OPTICAL STUDIES OF CURRENT-INDUCED SPIN-ORBIT EFFECTS IN MAGNETIC SYSTEMS

BY

WENRUI WANG

DISSERTATION

Submitted in partial fulfillment of the requirements
for the degree of Doctor of Philosophy in Physics
in the Graduate College of the
University of Illinois at Urbana-Champaign, 2019

Urbana, Illinois

Doctoral Committee:

Professor David G. Cahill, Chair
Associate Professor Virginia O. Lorenz, Director of Research
Professor Lance Cooper
Assistant Professor André Schleife

Abstract

Efficient electrical control of magnetic moments is essential for future spintronics applications, in which the intrinsic spin of the electron is utilized in addition to the electron charge for data processing and storage. Spin-orbit-interaction-induced phenomena, including the spin Hall effect, Rashba-Edelstein effect and the resultant spin-orbit torques (SOTs), have fueled the development of spintronics for more than a decade thanks to their promising magnetization-switching efficiencies. This dissertation presents experimental studies of current-induced novel phenomena arising from the spin-orbit interaction in magnetic materials. We first develop a highly-sensitive SOT magnetometer system based on the magneto-optic Kerr effect (MOKE). With the help of this sensitive system, we find an anomalous spin-orbit torque (ASOT) at the surfaces of single-layer magnetic thin films. Following the insight provided by the single-layer findings, we further demonstrate self-spin-orbit torque (SSOT) in multilayer systems lacking traditional nonmagnetic spin-source materials.

A simple and accurate SOT characterization approach is important not only for scientific research, but also for industrial product development. We develop a SOT magnetometer system employing MOKE and lock-in detection for high-sensitivity spin-orbit torque measurements. By controlling the incident light polarization in the normal-incidence configuration, polar- and quadratic-MOKE are used to measure out-of-plane and in-plane SOT-induced magnetization reorientation, respectively. Thanks to its simplicity and high sensitivity (< 70 nrad/$\sqrt{\text{Hz}}$ polarization rotation resolution), our SOT magnetometer system enables us to perform a variety of experiments for discovery of new phenomena.

A well-known spin-orbit-interaction-induced phenomenon in magnetic materials is the

anomalous Hall effect (AHE). In this dissertation, we report the observation of a counterpart of the AHE that we term the ASOT, wherein an electric current parallel to the magnetization generates opposite spin-orbit torques on the surfaces of the magnetic film. After a series of thickness-dependent and interface-varying experiments on different magnetic materials, we interpret the observed ASOT as due to a spin-Hall-like current generated with a high efficiency. This work leads to the conclusion that a single-layer ferromagnet can generate SOTs on its own surfaces, which introduces a new route for electrically manipulating magnetization in magnetic nanodevices.

Current-induced SOTs in multilayer structures consisting of a ferromagnetic metal (FM) and a nonmagnetic spin-source material (SSM) can efficiently manipulate the magnetization and magnetic textures of the FM. The origin of the SOT is often attributed to the spin current generated by the nonmagnetic SSM, which generates a spin transfer torque on the FM. In light of our study of ASOT in single-layer magnetic films, we examine the effects of an FM-originated spin current in multilayer structures. It turns out that such spin current leads to large SOTs on the FM itself. We refer to this long-overlooked SOT as the self-spin-orbit torque (SSOT). The discovery of SSOT provides a new method for manipulating magnetization by using magnetic materials that work with nonmagnetic SSMs constructively.

To my parents, Xingmeng Wang and Yong Liu,

and my wife, Evelyn Johnson,

for their infinite love and support.

Acknowledgments

It was a wonderful journey to study and do research in the Department of Physics at University of Illinois at Urbana-Champaign. There are so many people I would like to thank for their selfless help along the way. It would be impossible for me to be who I am today without their help.

First of all, I am deeply grateful to my Ph.D. advisor, Prof. Virginia Lorenz, for her constant support, encouragement, and inspiration throughout my Ph.D. study. I first met Gina at University of Delaware back in 2013. Thanks to her open mind and explorer's spirit, I was able to study the new research area of spintronics in our atomic/quantum physics group. During my Ph.D. study, besides the generous financial support, Gina also devoted herself in helping me be successful in many other aspects, such as, coursework and professional development. I deeply appreciate her guidance and kindness.

I would also like to thank my other academic adviser at UIUC, Prof. David Cahill, for his generous support, helpful suggestions and inspiring discussions. I was truly impressed by his physical intuition and attentive attitude for experiments. I learned a lot about how to interpret scientific problems from our discussions. I believe his wisdom will continue to benefit me in the future.

Special thanks to Prof. Xin Fan at University of Denver for his guidance and patience. You are one of the smartest and nicest people that I ever worked with. Many achievements would have been impossible without your contribution. I also appreciate all of my collaborators: Prof. John Xiao, Dr. Tao Wang, Yang Wang at University of Delaware for their hard work and help.

I also want to thank the members of Lorenz and Cahill groups: Dr. Bin Fang, Dr. Seth Meiselman, Dr. Halise Celik, Kai Shinbrough, Anil Radhakrishnan, Yujie Zhang, Kathleen Oolman, Fatemeh Amerikheirabadi, Oliver Wang, Dr. Zhu Diao, Kexin Yang, Hyejin Jang, Ella Pek. Many thanks for their help in experiments and discussions. In addition, special thanks to the staff members at MRL: Tao Shang, Fubo Rao, Xiaoli Wang and Jeff Grau, for their help in preparation of my samples.

I am deeply grateful to Prof. Lance Cooper and Prof. André Schleife for their willingness to serve as my dissertation committee members.

Last but not least, thank you to my parents, Xingmeng Wang and Yong Liu, and my wife, Evelyn Johnson, for their love and support.

Table of Contents

List of Abbreviations . . . . . **ix**

Chapter 1 Introduction **1**
1.1 Spintronics and Magnetoresistive Random Access Memory 1
1.2 Spin-Orbitronics 6
1.3 Magneto-Optic Kerr Effect 12
1.4 Dissertation Layout 15

Chapter 2 Device Fabrication and Characterization Techniques **17**
2.1 Device Fabrication Techniques 17
2.2 Device Characterization Techniques 25

Chapter 3 Magneto-Optic Kerr Effect Based Spin-Orbit Torque Magnetometer **30**
3.1 SOT-Induced Magnetization Reorientation 31
3.2 Polar and Quadratic MOKE in the Normal-Incidence Configuration 33
3.3 Experimental Setup 35
3.4 Calibration Method 37
3.5 Results 42
3.6 Comparison with the Spin-Torque Ferromagnetic Resonance (ST-FMR) Results 45
3.7 Conclusion 47

Chapter 4 Enhanced Signal-to-Noise Ratio in an Unbalanced MOKE System **48**
4.1 System Noise Calibration 48
4.2 Unbalanced Optical Bridge Method 52
4.3 Experimental Demonstration 55
4.4 Using the Unbalanced Method to Measure a Pattern-Free Sample 58
4.5 Conclusion 59

Chapter 5 Anomalous Spin-Orbit Torques in Magnetic Single-Layer Films **61**
5.1 Introduction 61
5.2 Symmetry Argument 63
5.3 Simulation and Observation of ASOT-Induced Magnetization Distribution . 65
5.4 Thickness-Dependent Study: Model and Results 74

5.5 Interface Contribution 82
5.6 First-Principles Calculation 83
5.7 Conclusion 86

Chapter 6 Self-Generated Spin-Orbit Torques in Magnetic Multilayers . 87
6.1 Introduction 87
6.2 Observation of the SSOT 89
6.3 Discussion of Spin-Orbit Torques in a Spin-Valve Structure 92
6.4 Separating MOKE Signals from Two FM Layers 94
6.5 Quantitative Analysis of the SSOT 98
6.6 Conclusion 101

Chapter 7 Conclusions 102

Chapter 8 References 104

Appendix A Jones Calculus Derivations 115
A.1 Overview of Jones Calculus 115
A.2 Derivation of MOKE Signal for Circular Polarization 118
A.3 Derivation of MOKE Signal for Linear Polarization 119
A.4 Derivation of MOKE Signal for the Magnetometer Setup 120

Appendix B MATLAB Code for Simulations 123
B.1 Signal-to-Noise Enhancement for Imperfect Linear Polarization 123
B.2 ASOT- and Calibration-Field-Induced Magnetization Distribution and MOKE Response 125

List of Abbreviations

GMR	Giant magnetoresistance.
FM	Ferromagnetic metal.
NM	Non-magnetic metal.
TMR	Tunneling magnetoresistance.
MTJ	Magnetic tunnel junction.
MRAM	Magnetoresistive random access memory.
STT	Spin transfer torque.
SOI	Spin-orbit interaction.
SOE	Spin-orbit effect.
SHE	Spin Hall effect.
SOT	Spin-orbit torque.
DL	Damping-like.
FL	Field-like.
MOKE	Magneto-optic Kerr effect.
PR	Photoresist.
XRD	X-ray diffraction.
HWP	Half wave plate.
QWP	Quarter wave plate.
S/N	Signal-to-noise.
AHE	Anomalous Hall effect.

ASOT	Anomalous-spin-orbit torque.
SSOT	Self-spin-orbit torque.
SSM	Spin-source material.

Chapter 1

Introduction

1.1 Spintronics and Magnetoresistive Random Access Memory

1.1.1 Giant Magnetoresistance

Spin electronics, or Spintronics, is a research field with the focus of understanding and utilizing the spin degree of freedom of electrons for next-generation data computing and storage. In addition to the electron charge, which fuels the development and success of modern electronics, electron spin is useful in efficient information storage and transport. One of the most important milestones in the development of spintronics is the discovery of giant magnetoresistance (GMR) by Albert Fert and Peter Grunberg in 1988 [1, 2]. They were later awarded the Nobel Prize in Physics in 2007 for their research and its practical significance. Phenomenologically, GMR can be described as an electrical resistance change of magnetic multilayer structures depending on the relative magnetization orientation of adjacent magnetic layers. For instance, as shown in Fig. 1.1, GMR is often studied or used in a sandwich structure of a ferromagnetic metal (FM)/ non-magnetic metal (NM)/ ferromagnetic metal (FM) stack, which is referred to as a spin-valve [3]. Due to spin-dependent electron scattering [4, 5], the "spin-up" and "spin-down" electrons experience different scattering rates in the FM layer. Namely, electrons with spin polarization parallel (anti-parallel) with the magnetization yield low (high) scattering rates. Therefore, when the two FM layers are magnetized in parallel, the resistance of the spin valve is lower than in

the anti-parallel case.

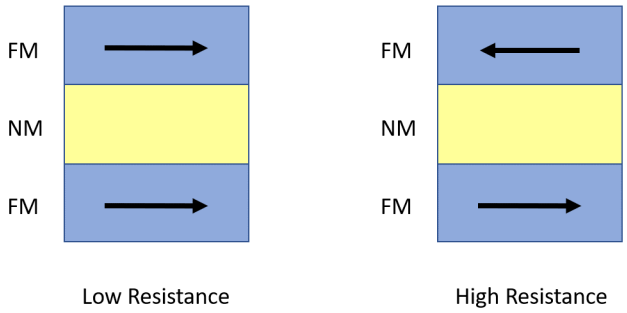

Figure 1.1: Illustration of the spin valve structure and GMR effect. The resistance of the spin valve is relatively low (high) when the two magnetizations are parallel (anti-parallel). The black arrows represent the magnetization directions in the ferromagnetic material (FM). NM: non-magnetic material.

Mathematically, the GMR can be expressed as GMR $= \frac{R_{\uparrow\downarrow}-R_{\uparrow\uparrow}}{R_{\uparrow\uparrow}}$, in which the normalized value of the resistance difference between the parallel ($R_{\uparrow\uparrow}$) and anti-parallel ($R_{\uparrow\downarrow}$) states is used to quantitatively characterize the strength of GMR. By proper choice of the materials and design of the spin valve structure, GMR of a few percent can be easily achieved [6]. Various applications based on the GMR principle, including magnetic field sensors and hard-disk drives (HDDs), have significantly benefited our daily lives [6, 7].

Similar to GMR, tunneling magnetoresistance (TMR) describes the same resistance change phenomenon in magnetic tunnel junctions (MTJs), where a thin insulator film (normally Al_2O_3 or MgO) is used to replace the conductive non-magnetic layer in spin valves [8–11]. Despite the similarity, the fundamental mechanism of TMR is quite different from that of GMR. Since a tunneling current through the insulator is forbidden by classical physics, this phenomenon can only be explained with quantum mechanics [12]. Compared to the GMR in spin valves, TMR in MTJs can reach a much higher value, up to 604% [13]. This advantage makes MTJs with high TMR a promising candidate for reliable memory applications such as magnetoresistive random access memory.

1.1.2 Magnetoresistive Random Access Memory

Magnetoresistive random access memory (MRAM) is a non-volatile memory with low power consumption and fast writing speed [14]. Because of its compatibility with the current CMOS technology and potential of realizing ultrahigh density, some researchers consider MRAM a strong candidate to replace static random access memory (SRAM) and dynamic random access memory (DRAM) as technology progresses. As a memory device, MRAM must possess three key components: (1) a unit/bit to store information, (2) a method to read/retrieve the information and (3) a method to write new information. The first two key components have actually already been discussed in the previous section. As shown in Fig. 1.2, the core units in MRAM for information storage are MTJs. The stable low (parallel) and high (anti-parallel) resistance states of an MTJ device represent "0" and "1" in a binary information system, respectively. The read mechanism is based on the magnetoresistance, for which a small current is applied from the source line to bit line to retrieve the stored information.

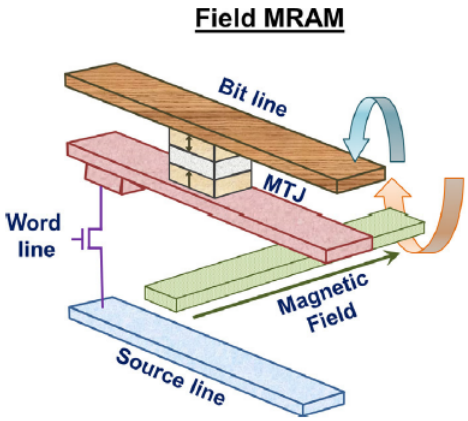

Figure 1.2: Illustration of the architecture of a field-switching MRAM. Information is stored in the MTJ structure by different resistance states. Reading is achieved by applying current through the source line and bit line to read the device resistance. Writing is realized by a pair of magnetic fields caused by currents through the bit line and word line. This figure is reproduced from Ref. [14].

As for the writing mechanism, multiple techniques have been implemented or proposed

so far. As illustrated in Fig. 1.2, the conventional way is to use a pair of current-induced orthogonal magnetic fields to switch the magnetization in the free layer of the MTJ, so that new information is written into the bit. This conventional design has been extensively studied and realized. However, this design requires the magnetization to lie in the plane of the magnetic thin films. This limits further scaling of the memory bits due to shape anisotropy. Moreover, the current needed to switch the magnetization via fields is also very high [15]. Therefore, a new write mechanism based on spin-transfer torque was put forward about two decades ago.

1.1.3 Spin Current and Spin Transfer Torque

In analogy with electric current, which is a flow of electron charge, spin current is a flow of electron spin. In non-magnetic metals, such as gold and copper, electrons with opposite spin polarization are equally populated and evenly distributed. Therefore, when an electric current flows through non-magnetic materials, "spin-up" and "spin-down" electrons have equal probability of transmission, resulting in no net spin current. However, if an unpolarized electric current is applied through a magnetic material, electrons with different spin polarization are subject to different scattering rates [16]. As a result, the output current yields a net spin polarization. This is called the spin filtering effect. In other words, magnetic materials can transform a pure charge current into a spin current.

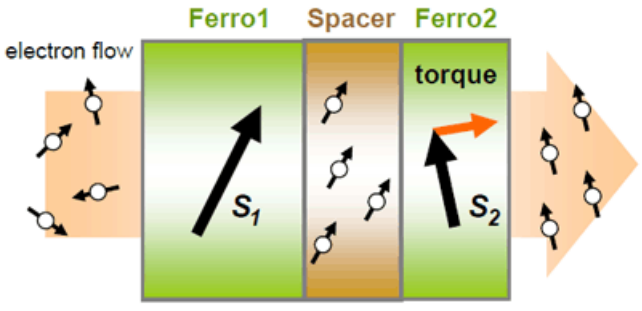

Figure 1.3: Illustration of the spin transfer torque. This figure is from Ref. [17].

When a spin current reaches another magnetic layer, if the spin polarization of the spin

current is not perfectly parallel with the local magnetization, the spin current can transfer its angular momentum and exert a torque on the local magnetization. This torque is the so-called spin transfer torque (STT). It was first predicted by Slonczewski [18] and Berger [19] in 1996. When the geometry is properly chosen, STT can overcome the damping of the magnetic material, which in turn leads to the switching of the magnetization. A simplified illustration of STT-induced magnetization switching is shown in Fig. 1.3. A spin current is first prepared by a reference magnetic layer via the spin filtering effect. Then, at the second magnetic layer, angular momentum is transferred from the spin current to the local magnetization by the STT, which can switch the magnetization if the spin current is strong enough [20–23].

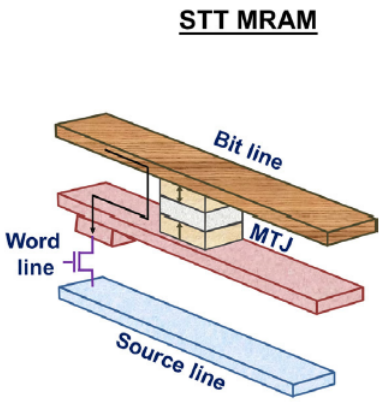

Figure 1.4: Illustration of the architecture of an STT-MRAM. The structure is less complex than the field MRAM. This figure is reproduced from Ref. [14].

Thanks to the discovery of STT, electrical manipulation of magnetic moments becomes possible. As a direct application, STT was proposed as another writing mechanism shortly after its discovery. As shown in Fig. 1.4, STT-MRAM does not require any external magnetic field. Instead, an electric current is sent through the MTJ to switch the bit. This advantage significantly simplifies the fabrication process. Furthermore, switching by current is also more scalable. In fact, shrinking bits to smaller sizes helps reduce the critical current amplitude for switching. Therefore, STT-MRAM is much more energy-efficient than field-

switching MRAM. In light of these advantages, companies like Everspin, Samsung and IBM are all working on bringing out the newest STT-MRAM product. As of today, the largest volume STT-MRAM chip is 256 MB from Everspin Technologies [24].

Regardless of the previously mentioned advantages, STT-MRAM does have a few drawbacks as well. First of all, even though the writing current of STT-MRAM is lower than in many other memory technologies, it is still quite high, which means high energy consumption and potential heating problems [25]. In addition, the mechanism of STT-MRAM requires the writing and reading circuits to share the same path [25]. This limitation significantly increases the error rate and breakdown probability. A trade-off between thermal stability and barrier oxide breakdown current needs to be carefully made. On the one hand, if the thermal stability factor is too low, a small read current may accidentally switch the bit, leading to an error. On the other hand, if the thermal stability factor is too high, high current is necessary to write information, which may cause barrier oxide breakdown. Therefore, due to these shortcomings, alternative mechanisms are extensively being explored to replace the STT.

1.2 Spin-Orbitronics

In the last decade or so, a sub-field of spintronics called spin-orbitronics developed rapidly because of its promising potential to replace STT-based technologies. Spin-orbitronics is based on the spin orbit interaction (SOI) in materials. The related effects are referred to as the spin-orbit effects (SOEs).

1.2.1 Spin Hall Effect

One of the best well-known SOEs is the spin Hall effect (SHE). The SHE is a phenomenon in materials exhibiting strong SOI wherein an electric current produces a spin current transverse to the electric current direction. The spin current, in turn, results in a spin accumulation

at the surfaces of the material. The SHE arises from the SOI, which leads to deflection of electrons with opposite spin polarization in opposite directions. An illustration of the SHE is shown in Fig. 1.5. This phenomenon was first discussed by Dyakonov in 1971 [26], and revived by Hirsch in 1999 [27].

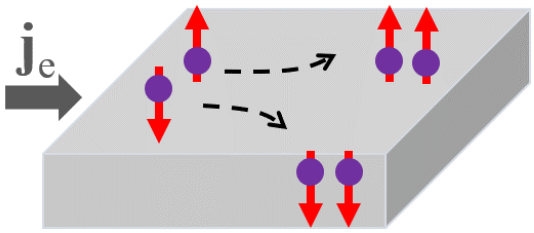

Figure 1.5: Illustration of the spin Hall effect. Purple dots represents electrons. Red arrows are spin polarizations. Black dashed arrows simulate the electron deflection trajectories.

Mathematically, the SHE can be described by

$$\boldsymbol{Q}_\sigma = \frac{\hbar}{2e}\theta_{\mathrm{SH}}\boldsymbol{j}_c \times \boldsymbol{\sigma}, \tag{1.1}$$

where $\boldsymbol{Q}_\sigma$ is the spin current density, $\hbar$ is the reduced Planck's constant, e is the electron charge, $\boldsymbol{j}_c$ is the electric current density, $\boldsymbol{\sigma}$ is the spin polarization unit vector, and θ_{SH} is a dimensionless value representing the charge-to-spin-current conversion efficiency, which is often referred to as the spin Hall angle or spin Hall efficiency. Based on Eq. 1.1, the charge current direction, spin current direction and spin polarization should be orthogonal to each other. There are two mechanisms associated with the SHE: one is the intrinsic SHE, which is related to the band structure of the crystaline solid [28]; the other is the extrinsic SHE, which is due to impurity-induced scattering, including skew-scattering and side-jump effect[27].

The SHE provides a new way of generating pure spin current without a magnetic layer. And, if a magnetic layer is deposited on top of a strong spin Hall material, the SHE-generated spin current can exert an STT-like torque on the local magnetic moment. Thanks to the

large spin Hall angle of some materials, such as Pt [29], β-Ta [30] and β-W [31], SHE-induced torque is a promising candidate for more energy-efficient control of magnetism.

1.2.2 Rashba-Edelstein Effect

Another example of SOEs is the Rashba-Edelstein effect, or simply Rashba effect [32]. It also originates from spin-orbit coupling, but, compared to the SHE, which is a bulk effect, the Rashba effect only appears at the interface. In principle, the broken inversion symmetry at the interface creates an effective electric field normal to the interface. This additional field leads to one extra SOI term. The Rashba-induced SOI term causes a wavevector-dependent spin splitting in the electron band structure. At equilibrium, when no electric current is applied, the "spin-up" and "spin-down" states are equally populated. However, when an electric current is applied in the plane of the interface, the electrons experience an effective magnetic field that is in-plane and perpendicular to the charge current. As a result, net spin accumulation occurs at the interface [33, 34].

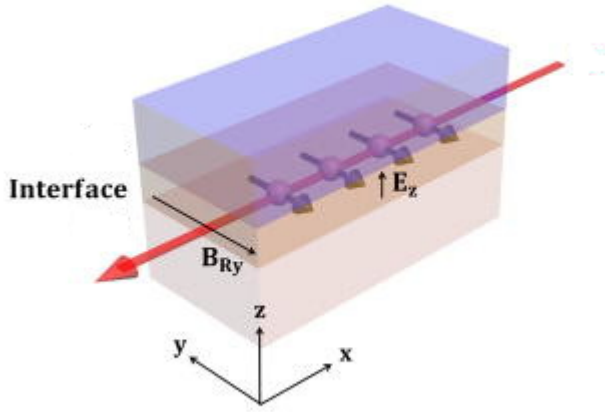

Figure 1.6: Illustration of Rashba-induced spin accumulation at the interface. E_z is the effective electric field due to inversion symmetry breaking. B_{Ry} is the effective Rashba magnetic field. Red arrow represents the electric current direction. Dots and arrows in the interface layer represent the spin accumulation. This figure is reproduced from Ref. [34].

If one of the materials comprising the Rashba interface is magnetic, due to exchange coupling, the interfacial spin accumulation can exert torques that are very similar to those from the SHE on the adjacent magnetic layer.

1.2.3 Spin-Orbit Torques

As discussed in the previous two subsections, both the SHE and the Rashba effect can generate non-equilibrium spin angular momentum and exert torques on adjacent magnetic layers. Despite their quite different mechanisms, the resultant torques have very similar forms. Given their common origin of spin-orbit coupling, the SHE- or Rashba-induced torques are all referred to as spin-orbit torques (SOTs). Generally speaking, there are two forms of SOT: damping-like torque (DL-SOT) and field-like torque (FL-SOT). The effect of the two torques on magnetic moment dynamics can be expressed by the Landau-Lifshitz-Gilbert-Slonczewski (LLGS) equation [35]:

$$\frac{\mathrm{d}\boldsymbol{m}}{\mathrm{dt}} = -\mu_0\gamma\boldsymbol{m}\times\mathbf{H}_{\text{eff}} + \alpha\boldsymbol{m}\times\frac{\mathrm{d}\boldsymbol{m}}{\mathrm{dt}} + \tau_{\mathrm{DL}}\boldsymbol{m}\times(\boldsymbol{\sigma}\times\boldsymbol{m}) + \tau_{\mathrm{FL}}(\boldsymbol{\sigma}\times\boldsymbol{m}), \tag{1.2}$$

where $\boldsymbol{m}$ is the magnetic moment unit vector, μ_0 is the vacuum permeability, γ is the gyromagentic ratio, $\mathbf{H}_{\text{eff}}$ represents the effective magnetic field, α is the damping coefficient, and τ_{DL} and τ_{FL} are the DL-SOT and FL-SOT parameters, respectively. The LLGS equation describes SOT-related magnetic moment dynamics. Similar to the STT, DL-SOT arises from the angular momentum transfer between spin current and the local magnetic moment. It yields a form similar to the damping term in the LLGS equation. Therefore, by properly arrange the system geometry, DL-SOT can be used to cancel out the intrinsic damping in the magnetic material, leading to magnetic moment switching. The origin of the FL-SOT has been attributed to the Rashba-induced spin accumulation at the interface and exchange coupling with the magnetic moment. However, several researchers have reported results indicating FL-SOT can also arise from the SHE spin current [36, 37]. Regardless of the

mechanism, FL-SOT indeed affects the magnetic moment dynamics. A phenomenological diagram of the SOT-induced magnetic moment dynamic processes is displayed in Fig. 1.7.

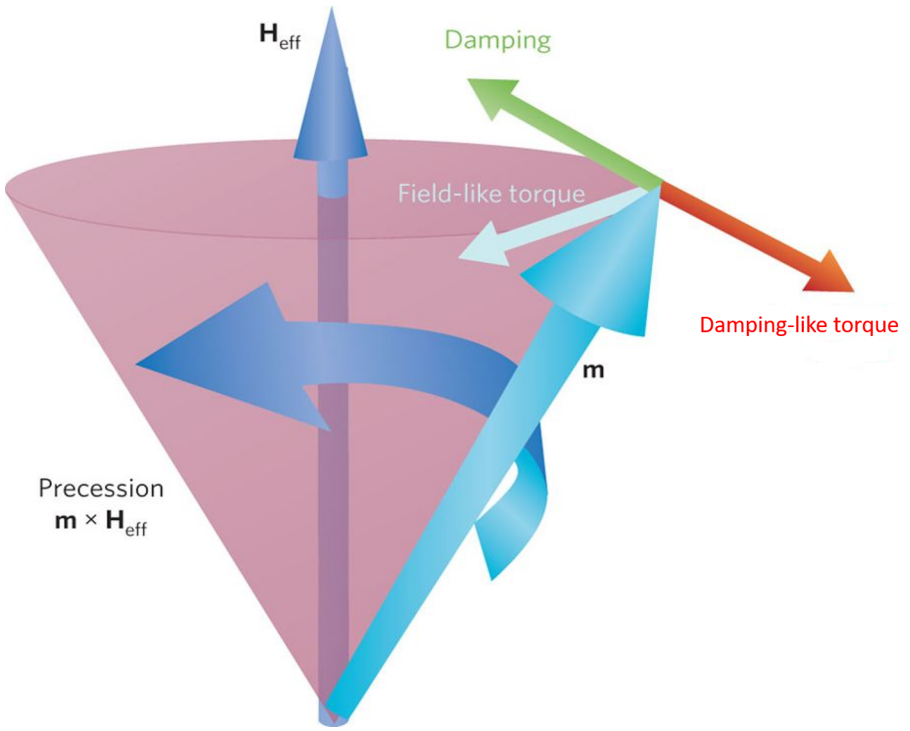

Figure 1.7: Illustration of the SOT-induced magnetic moment dynamics. The green arrow illustrates the magnetic damping that tends to move the magnetization toward the effective field direction. The red arrow is the DL-torque and the light-blue arrow is the FL-torque with an electron spin polarization collinear with the effective field. This figure is modified from Ref. [38].

On the other hand, in a quasi-static situation, SOTs also lead to magnetization reorientation. If we ignore the time-dependent terms in the LLGS equation, the two SOTs can be approximately considered as two effective fields, namely, a DL-field, $h_{\mathrm{DL}} \propto \boldsymbol{m} \times \boldsymbol{\sigma}$, and an FL-field, $h_{\mathrm{FL}} \propto \boldsymbol{\sigma}$ [38]. A detailed discussion of SOT-induced magnetization reorientation is presented in Chap. 3. By measuring the amplitude and direction of the SOT-induced magnetization reorientation, some key characteristics of the SOTs can be quantitatively determined. This is important for a better understanding of the SOTs.

Because of the low critical current in SOT-switching, SOT-based MRAM has been extensively studied and proposed as a promising candidate to replace STT-MRAM. The first

experimental attempt at using SOT in MRAM was done by Liu *et al.* in 2012 with β-Ta [30]. In their experiments, SOT-induced magnetization switching was demonstrated in both in-plane and perpendicular anisotropy MTJs. Later simulation and experiments also suggest that SOT-MRAM have better critical current density, write delay and retention failure rate than STT-MRAM [14, 39]. As shown in Fig. 1.8, SOT-MRAM has separate write and read paths. The information is read by sending a small current from bit line to source line, while the write process relies on a larger current from the word line to the source line. SOT makes lower power consumption and faster writing speed possible. And, the separate read and write paths eliminate the trade-off between thermal stability and barrier oxide breakdown current as in STT-MRAM. However, as mentioned earlier, some fundamental questions about SOTs such as the bulk/interface origin and contribution of the magnetic materials are still unsolved and commercial applications require more research to find novel spin-orbit mechanisms for optimal write currents. Therefore, I devote my dissertation research to the field of spin-orbitronics.

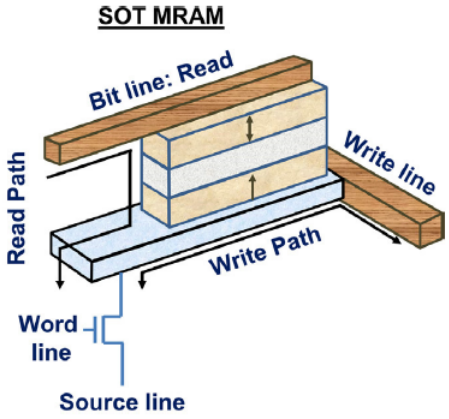

Figure 1.8: Illustration of the architecture of an SOT-MRAM. The three-terminal design significantly improves the error rate. This figure is reproduced from Ref. [14].

1.3 Magneto-Optic Kerr Effect

To study SOI-induced effects on magnetization, we develop an SOT magnetometer based on the magneto-optic Kerr effect (MOKE). Compare to the common electric techniques used to measure magnetic transport signals, MOKE-based SOT magnetometers have the following advantages: (1) compatibility with magnetic materials exhibiting both in-plane and out-of-plane anisotropies, (2) independence on the applied current frequency, (3) ability to measure very thin magnetic films, and (4) simplicity in implementation. A more detailed description of our SOT magnetometer is provided in Chap. 3.

MOKE describes the change of light polarization upon reflection from a magnetized surface. This phenomenon was first discovered by John Kerr in 1877 [40], shortly after the discovery of another magneto-optic effect, the Faraday effect, in 1845 [41]. The Kerr effect is just the reflection-configuration counterpart of the Faraday effect, which applies in the transmission configuration. The change of light polarization due to MOKE is demonstrated in Fig. 1.9. For light initially with linear polarization, after reflecting from a magnetic surface, its polarization becomes elliptical. Quantitatively, this change can be characterized by a rotation of polarization direction, called the Kerr rotation θ_K, and a term describing the ellipticity of the reflected light, the Kerr ellipticity ϵ_K. Consequently, the polarization change $\Psi(\boldsymbol{m})$ can be written as

$$\Psi(\boldsymbol{m}) = \theta_K + \mathrm{i}\epsilon_K. \tag{1.3}$$

In principle, MOKE arises from the non-zero off-diagonal components in the permittivity tensor, $\boldsymbol{\epsilon}$. Since the permittivity tensor can be expressed as a Taylor series in different components of the magnetization unit vector, the corresponding MOKE response should also have multiple orders of magnetization-dependence: $\epsilon_{ij}(\mathbf{m}) = \epsilon_{ij}^{(0)} + \sum_k \epsilon_{ijk}^{(1)} m_k + \sum_{k,l} \epsilon_{ijkl}^{(2)} m_k m_l + ...$, where $i, j, k, l = x, y, z$ [42]. In most cases, the first-order (linear) MOKE dominates the polarization response. Under the first-order approximation, the magnetization-dependent

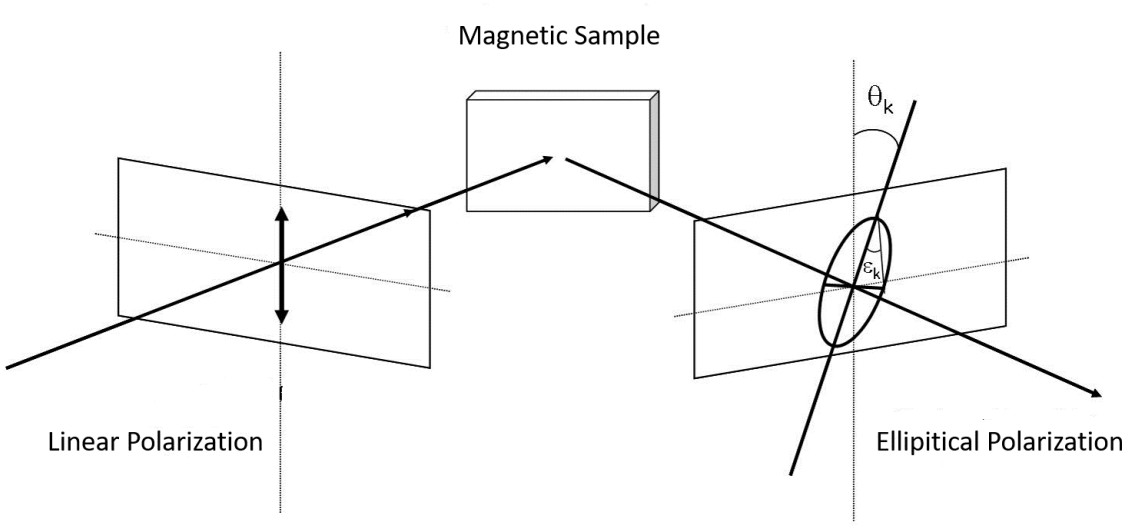

Figure 1.9: Illustration of the magneto-optic Kerr effect.

off-diagonal components create an anisotropic permittivity:

$$\boldsymbol{\epsilon} = \epsilon_0 \begin{bmatrix} 1 & -iQm_z & iQm_y \\ iQm_z & 1 & -iQm_x \\ -iQm_y & iQm_x & 1 \end{bmatrix},$$

where Q is the magneto-optic coefficient [43]. Since the absorption and speed of light in materials are determined by the permittivity, the different polarization components of the incident light experience different absorption and index of refraction as they propagate through the material, resulting in an overall polarization change.

Higher-order MOKEs are also useful in certain applications. The second-order (quadratic) MOKE becomes significant in materials yeilding weak linear MOKE response. For example, large quadratic MOKE has also been observed in antiferromagnets [44] and Heusler alloys [45, 46]. Quadratic MOKE is also important in certain detection geometries, where the capability of linear MOKE is limited. In my dissertation study, both linear and quadratic MOKE are studied and implemented experimentally. More details are discussed in Chap. 3.

1.3.1 Geometries of First-Order MOKE

For first-order MOKE, depending on the relation between the magnetization direction and the plane of light incidence, there are three typical geometries: polar MOKE, longitudinal MOKE and transverse MOKE. As shown in Fig. 1.10(a), polar MOKE describes the change of light polarization due to the magnetization component that is normal to the sample surface and parallel to the plane of incidence. When the light is normally-incident, the first-order MOKE signal is only sensitive to the polar MOKE response. On the other hand, as shown in Fig. 1.10(b), longitudinal MOKE accounts for the polarization change resulting from the magnetization component that is in both the sample plane and plane of incidence. Transverse MOKE, which describes a reflectivity change, rather than a polarization change, of the light due to the magnetization component that is in the sample plane and perpendicular to the plane of incidence, is illustrated in Fig. 1.10(c). In all three geometries, the MOKE response is linearly proportional to the magnetization strength. Polar MOKE is most widely used thanks to its simplicity in implementation and analysis.

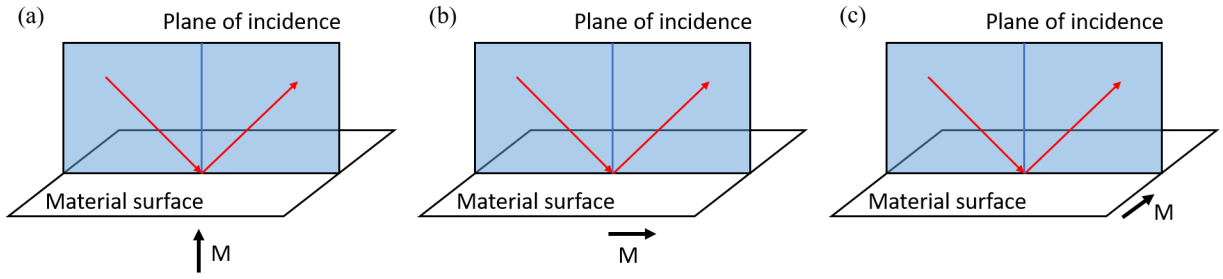

Figure 1.10: Illustration of the geometries of (a) polar MOKE, (b) longitudinal MOKE and (c) transverse MOKE. Red arrows represent the incident and reflected light; blue line is the material surface normal; black arrows are directions of the magnetization, **M**.

On the application side, MOKE has served as a powerful tool in magnetism research for a long time. For example, MOKE microscopy is very convenient and accurate for magnetic domain structure characterization. With the development of ultrafast laser technology, MOKE also plays an critical role in time-domain studies of dynamic processes. In this work,

a polar MOKE configuration with normally-incident light is developed and used for SOT studies.

1.3.2 Jones Calculus

In MOKE-related experiments, it is essential to have a method of simulation for better understanding of the observed signal. Since MOKE mostly results in a change of light polarization, Jones calculus is often used to calculate the resultant polarization state. Jones calculus was first demonstrated by R. C. Jones in 1941 [47]. It provides a vector/matrix formulation of polarized light and linear optics, in which polarized light is represented by 2×1 Jones vector and linear optical elements are represented by 2×2 Jones matrices. In this dissertation study, Jones calculus is applied on multiple occasions including MOKE signal analysis and signal-to-noise ratio characterization. An overview of Jones calculus is provided in Appendix.A. A more detailed implementation of Jones calculus for our MOKE-based SOT magnetometer system is discussed in Chap. 3.

1.4 Dissertation Layout

In this dissertation, I experimentally investigate current-induced SOEs and the resultant SOTs in magnetic systems, with a focus on the SOEs originating from metallic magnetic materials. By measuring SOT-induced magnetization reorientation using an optical magnetometer based on MOKE, I not only reveal novel phenomena that may impact the current understanding of physics in such systems, but also provide a tool for efficient device characterization.

This dissertation is organized as follows:

In Chapter 2, I summarize the sample fabrication and characterization methods that I utilize for my dissertation research. The basic principles of magnetron sputtering, argon ion milling, photolithography, ellipsometry and X-ray diffraction are reviewed. Key experimental

parameters are also listed for future reference.

In Chapter 3, I introduce a highly sensitive optical SOT magnetometer system based on MOKE that I built for this dissertation study. First, I discuss the SOT-induced magnetization reorientation and its connection to polar and quadratic MOKE. Second, I describe the experimental system and calibration methods for accurate SOT measurement. Lastly, the accuracy and precision of the system is demonstrated via a series of experiments and comparison with the results of other methods.

In Chapter 4, I describe a modified SOT magnetometer setup that achieves more than 3 times signal-to-noise ratio improvement. A system noise analysis is first presented to support our assumptions for the method. Theoretical and experimental results are then used to demonstrate the capability and reliability of the new method.

In Chapter 5, I explain our discovery of a novel SOT in single-layer magnetic materials. I present our experimental observation of the SOT and numerically simulate the resulting MOKE signal. Based on measurements of multiple magnetic materials and first-principles calculations, we conclude this novel SOT arises from the intrinsic properties of the magnetic materials.

In Chapter 6, I describe a self-induced SOT in magnetic materials caused by the exit of spin current generated from the same magnetic material. Experimental results in a spin-valve structure are discussed to demonstrate the self-SOT. A new technique is also introduced for separation of MOKE responses from different magnetic layers.

In Chapter 7, I summarize the key findings of this dissertation and possible future research directions.

Chapter 2

Device Fabrication and Characterization Techniques

2.1 Device Fabrication Techniques

In the study of current-induced spin-orbit effects, researchers typically need the current density to be 1×10^6 A/m^2 or higher. To realize such a high current density while keeping the sample heating low, small feature size is necessary. Therefore, micro/nano-fabrication techniques are often used in the sample preparation process. In my dissertation work, I used magnetron sputtering for thin film depositions. Photolithography and ion mill etching were used to further pattern the sample/device into the desired shape and size.

2.1.1 Thin Film Deposition: Magnetron Sputtering

Magnetron sputtering is one of the most widely used thin-film deposition methods [48]. By the nature of its mechanism, magnetron sputtering is categorized as a physical vapor deposition (PVD) technique, which is in contrast to the chemical vapor deposition (CVD) techniques, such as atomic layer deposition. This technique has the advantages of system simplicity, fast deposition rate as well as versatility in material choices.

A typical sputtering process needs to be in a high-vacuum environment with a base pressure $< 1 \times 10^{-7}$ Torr. The goal is to minimize the background gases and potential contaminants. After the base pressure is reached, Ar-gas is flowed into the chamber and the chamber pressure is maintained at a stable level (normally, a few mTorr). A plasma is then generated by applying a high electric potential difference between the material target

(cathode) and the substrate (anode). Under this high voltage, the neutral Ar atoms are ionized into positive Ar ions and free electrons. The generated free electrons further interact with other neutral atoms to continue the ionization process, while the positive Ar ions are accelerated towards the cathode and bombard the surface of the target material. Upon these collisions, the kinetic energy of the Ar ions is transferred to the target material and the target atoms are ejected into the vacuum environment with enough energy to reach the substrate, e.g. a Si wafer (See Fig. 2.1(a)).

Magnetron sputtering improves the performance of the above mentioned process by using a magnetic field to confine the free electrons near the target. As illustrated in Fig. 2.1(b), with the additional magnetic fields, free electrons are "trapped" in the space where the magnetic field is strong due to the Lorentz force. A higher free electron density results in a higher plasma density. Therefore, the deposition rate is significantly enhanced. In addition, better confinement of the free electrons reduces the damage to the substrate and deposited thin film.

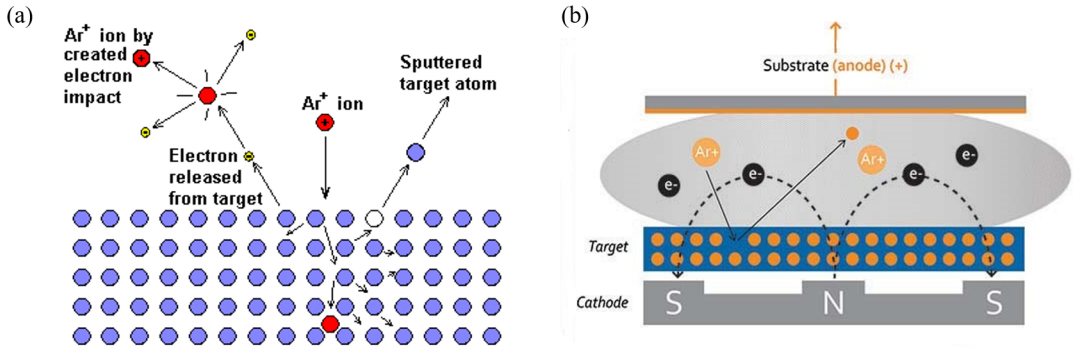

Figure 2.1: Illustration of (a) the general sputtering process, where target atoms are "sputtered" off the target surface by the accelerated argon ions in a plasma; (b) the magnetron sputtering process, where free electrons are well-confined by the magnetic field. A much higher density of plasma can be reached near the target surface, which in turn leads to a faster deposition rate. This figure is reproduced from Ref. [49].

As mentioned in the beginning paragraph, magnetron sputtering is suitable for various materials. There are different power source selections for different target materials. For con-

ductive targets, such as metals, DC magnetron sputtering is sufficient, because the positive charges from the Ar ions can be conducted away. Therefore, the electric potential between the target and substrate can be sustained. However, if the target material is insulating, such as oxides, positive charges will accumulate on the target and eventually generate a positive electric field, preventing the Ar ions from reaching the target. To overcome this issue, we can use radio frequency (RF) magnetron sputtering, in which an alternating electric field makes the positive ions and free electrons alternately bombard the target to neutralize the accumulated charges [50, 51].

For the thin films included in this dissertation, namely, Pt, Cu, $Ni_{80}Fe_{20}$, Al, Ti, Au and IrMn, we deposit via DC magnetron sputtering. Oxide layers, such as SiO_2, are deposited via RF magnetron sputtering. Samples studied in this Chap. 5 and Chap. 6 are fabricated by our collaborators in University of Delaware.

2.1.2 Photolithography

Photolithography is a technique widely used in microelectronic device fabrication processes [52]. It utilizes a combination of UV-light-sensitive chemical "photoresist" (PR) and photomasks that have user-defined geometric patterns. By shining UV-light through a photomask onto different types of PR, users can transfer a pattern from the photomask to the PR on top of the substrate, which enables them to either deposit new materials in a certain pattern or remove old materials from certain parts. Photolithography is the standard method of printed circuit board (PCB) and microprocessor fabrication.

A typical photolithography process involves various steps depending on the process purpose. But, these steps normally happen in a certain sequence, which can be categorized as: cleaning and preparation, PR application (spin coating), exposure and development, deposition/etching and PR removal [53].

Cleaning and preparation: The goal of this step is to remove all the organic and inorganic contamination on the substrate surface so that the substrate is ready for the PR

applications. In the process that I used for my samples, I apply acetone, isopropyl alcohol (IPA) and distilled water in sequence to clean the substrate. An ultrasonic bath is suggested if the substrate is really dirty. Then, I bake the substrate on a hotplate at 110°C for 2 minutes to get rid of the moisture on the wafer surface.

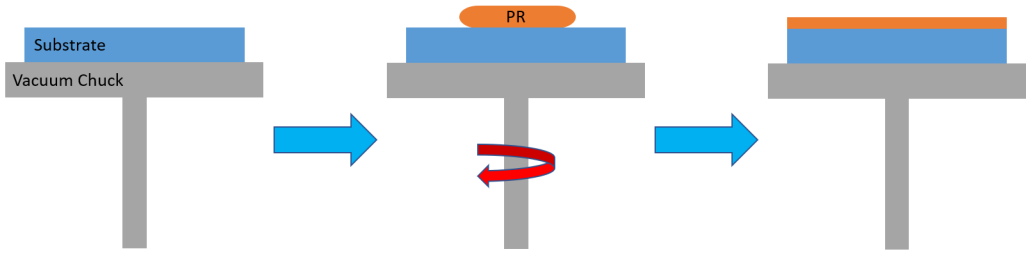

Figure 2.2: Illustration of the spin coating process. High speed rotation produces a PR layer with a uniform thickness.

PR application (spin coating): Spin coating is a technique used to provide uniformly distributed PR on the substrate surface. As illustrated in Fig. 2.2, the viscous, liquid PR is dispensed and spun on top of the substrate surface. Due to the spinning nature of this method, circular substrates are always recommended for spin coating. In the case of my work, I use a speed of 4000 rpm for 45 seconds to realize a PR thickness of 1.4 microns [54]. After the PR application, a prebake at 110°C for 75 seconds is normally performed to drive off excess PR solvent on the substrate.

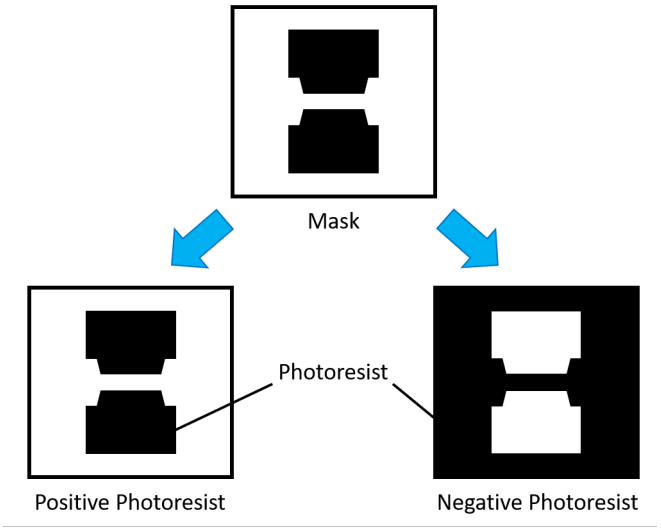

Figure 2.3: Illustration of the PR types. The mask is used to transfer the pattern to the PR. It's normally made of glass and patterned with chrome. The black part is opaque and the white area is transparent. After the exposure and development, positive PR keeps the exact same pattern as the mask. (Exposed PR is removed) On the other hand, negative PR shows opposite phenomenon, where the unexposed PR is removed.

Exposure and development: After the prebaking, the PR is exposed to a pattern of UV light on a mask-aligner. There are two kinds of PR: positive PR and negative PR. For positive PR, the exposed part can react with the developer and be dissolved, with the unexposed part staying on the substrate. In contrast, negative PR does not react with the developer if it is exposed, so the exposed pattern persists on the substrate (Fig. 2.3). Each PR has its applications. For example, in my work, positive PR is used to pattern the deposited thin films followed by ion mill etching to remove the exposed materials. Negative PR is useful in the electrode deposition process. In a process called "lift-off", the negative PR is first coated and patterned before the deposition of electrode materials. Then, upon removal of the PR, the materials on top of the PR are washed away together with the PR (Fig. 2.4). This is a more efficient technique for thick pattern depositions. In my work, I used AZ-5214E PR [54], which can be used as both positive and negative PR. The AZ-917 MIF developer is a good match to AZ-5214E. The normal development time is between 30 and 40 seconds.

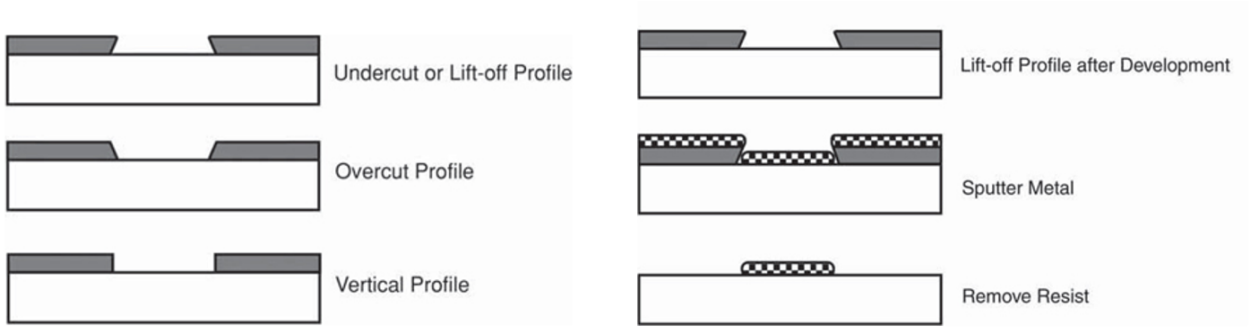

Figure 2.4: Illustration of the "lift-off" process. The undercut PR profile is critical for a successful "lift-off" process. So, precise control of exposure dose is important. This figure is reproduced from Ref. [55].

Deposition and etching: This step is performed after the PR profile is defined. Based on the PR types used in the previous process, ion mill etching (for positive PR), explained in the next section, or magnetron sputtering deposition (for negative PR) can be used.

PR removal: After the deposition/etching step, PR needs to be removed so that the sample can be ready for measurements or further processes. There is a wide choice of PR removers suitable for different PRs. For AZ-5214E, acetone is a good solvent to remove it. Typically, the sample need to be soaked in acetone for over half an hour. Heating and an ultrasonic bath are also often used to speed up the process. A simplified process flow chart is shown in Fig. 2.5.

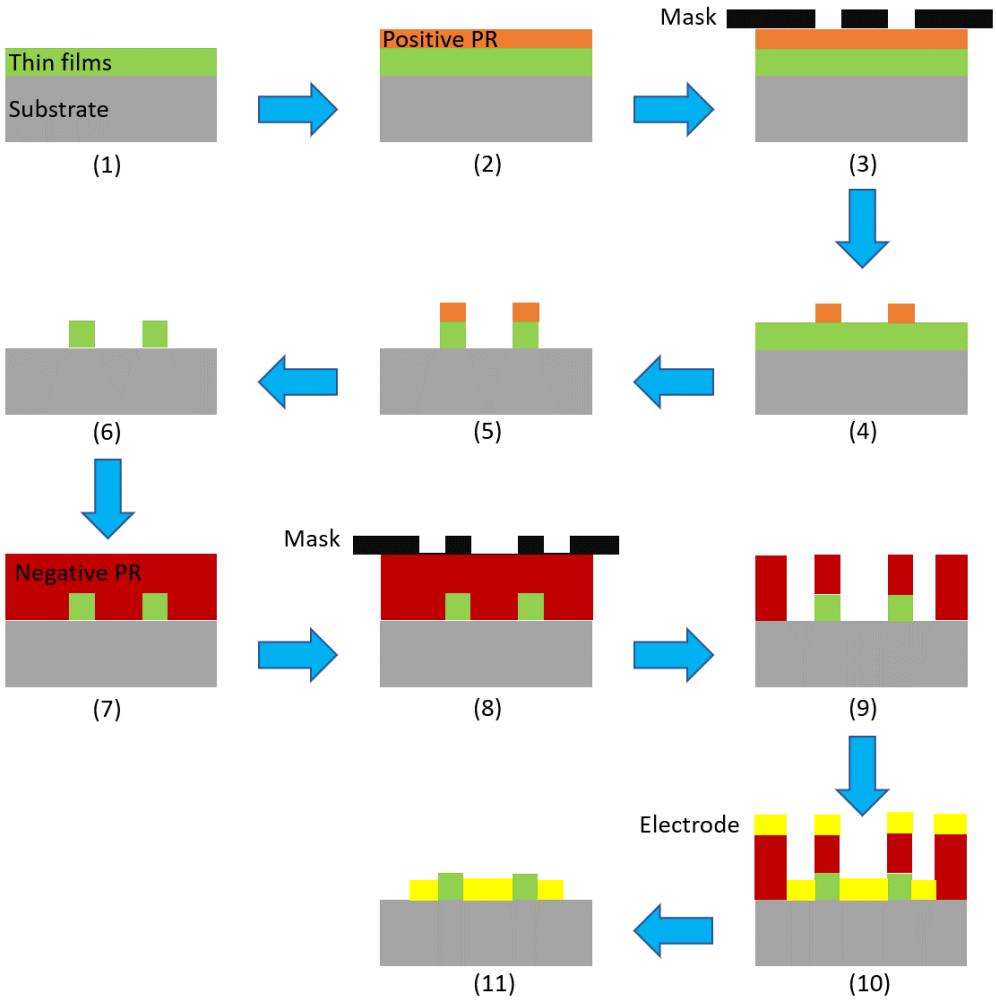

Figure 2.5: Fabrication process flow chart for a typical current-induced spin-orbit torque device. The steps are: (1) Deposit the magnetic multilayer thin film for current-induced spin-orbit effect studies, (2) apply the positive PR for the etching pattern, (3) expose the sample on a mask-aligner, (4) develop the PR and define the PR profile, (5) pattern the magnetic heterostructure with ion mill etching, (6) remove the positive PR residue, (7) coat the substrate with negative PR for the electrode, (8) exposure, (9) develop the negative PR to produce the undercut profile for "Lift-off" [55], (10) deposit the electrode materials via magnetron sputtering, (11) PR removal and postbake at 110°C for 3 minutes.

2.1.3 Ion Mill Etching

As mentioned in the previous section, ion mill etching is often used following photolithography to remove excess material so that a specific pattern can be achieved. Ion mill etching is a pure physical process, in which high energy heavy ions (e.g. Ar^+) bombard the surface of a PR-patterned substrate in a vacuum chamber. While the whole substrate is etched by the ion beam, the PR protects the underlying materials during the process. In addition, the PR's etching rate is much lower than that of the material to be removed. Therefore, when the etching process is completed, the remaining material defines the desired small feature size.

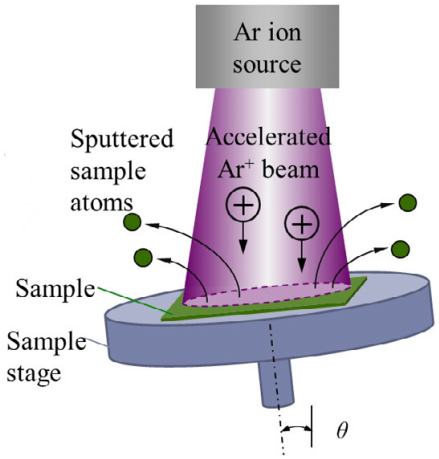

Figure 2.6: Schematic diagram of a typical Ar ion mill. This figure is reproduced from Ref. [56].

Fig. 2.6 shows a simplified diagram of an ion mill etching machine. Argon ions are generated by discharge ionization in the discard chamber. While the plasma is completely contained in the discard chamber, the argon ions are accelerated by a pair of optically aligned grids and ejected into the vacuum work chamber. The work chamber pressure should be at moderate vacuum ($< 1 \times 10^{-4}$ Torr) so that the mean free path is longer than the distance between ion source and substrate. The neutralizer beam prevents positive charge accumulation on the substrate, which may significantly affect the etching rate. To achieve the optimal etching uniformity and rate, the substrate is often attached to a water/liquid

nitrogen-cooled tilted rotation plate. Since argon ions carry a great amount of energy, it is important to make sure the substrate is not overheated. An overheated substrate not only becomes more fragile, but also changes the properties of the PR on top, which makes the PR difficult to remove. The tilted plate is to avoid the scattered particles interacting with the incoming ions. A constant speed rotation helps with the uniformity of the etching.

For the etching performed for this dissertation, base pressure is normally below 2×10^{-6} Torr and Ar pressure is controlled between 2×10^{-4} Torr and 5×10^{-4} Torr. Other specifications include: Ar flow rate = 3 sccm; beam voltage = 250 V; beam current = 50 mA; accelerate voltage = 30 V; neutralizer current = 60 mA. To avoid overheating, liquid nitrogen cooling is used.

2.2 Device Characterization Techniques

In the study of the current-induced spin-orbit effects, to quantitatively determine the strength of the spin-orbit torques, we characterize key parameters of the deposited thin films and fabricated devices. For instance, we measure resistivity of the investigated spin-orbit devices with the four-point probe method and the refractive indices of materials with ellipsometry analysis. Furthermore, X-ray diffraction (XRD) techniques are used to determine material properties like crystalline structure and thickness of the thin films.

2.2.1 Four-Point Resistivity Measurement

The four-point probe method is a widely used technique in measuring small resistance with high accuracy. Compared to the two-point probe method, whose accuracy is significantly affected by the contact and spreading resistances associated with the probes, the four-point method mostly eliminates the contributions from contact and spreading resistances by separating the detecting probes from the voltage source probes. Thus, one can obtain a fairly accurate reading of the resistivity [57].

The basic principle of the four-point probe technique is shown in Fig. 2.7. As a constant current I runs through the Hall bar, the electric potential between two points along the longitudinal wire is nonzero. By measuring the voltage difference, the sheet resistance R_s of the material can be calculated with

$$R_s = \frac{\Delta V}{I}\frac{L}{W}, \tag{2.1}$$

where R_s is the sheet resistance with units of $\Omega/\square$, which can be interpreted as the resistivity of a uniform film with unit thickness; I is the current through the longitudinal wire; L is the distance between the two voltage terminals; and W is the width of the longitudinal wire. Once the sheet resistance is extracted, the material resistivity can be computed as: $\rho = R_s t$, where t is the thickness of the film.

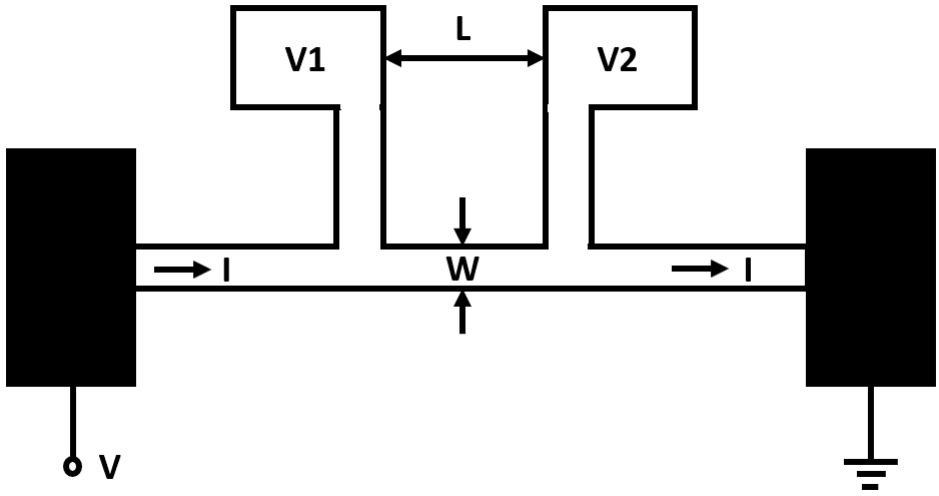

Figure 2.7: Illustration of the principle of the four-point probe method. A Hall bar structure is usually used for such measurements. A bias voltage V is applied between the two "edge" pads, which generates a current I in the wire. The potential difference between the two middle voltage terminals, $\Delta V = V_2 - V_1$, is measured to calculate the sheet resistance.

2.2.2 Ellipsometry

Ellipsometry is an optical technique for investigating dielectric properties such as the complex refractive index of thin films [58]. It measures the polarization change upon reflection from a material and extracts the property information by comparing the result to a model. Within the framework of this dissertation work, a spectroscopic ellipsometer is used to measure the complex refractive indices of materials for the propagation matrix numerical simulation in Chap. 5. However, ellipsometry can also be applied in the characterization of film composition, surface roughness, thickness, crystalline nature and many other material properties [59].

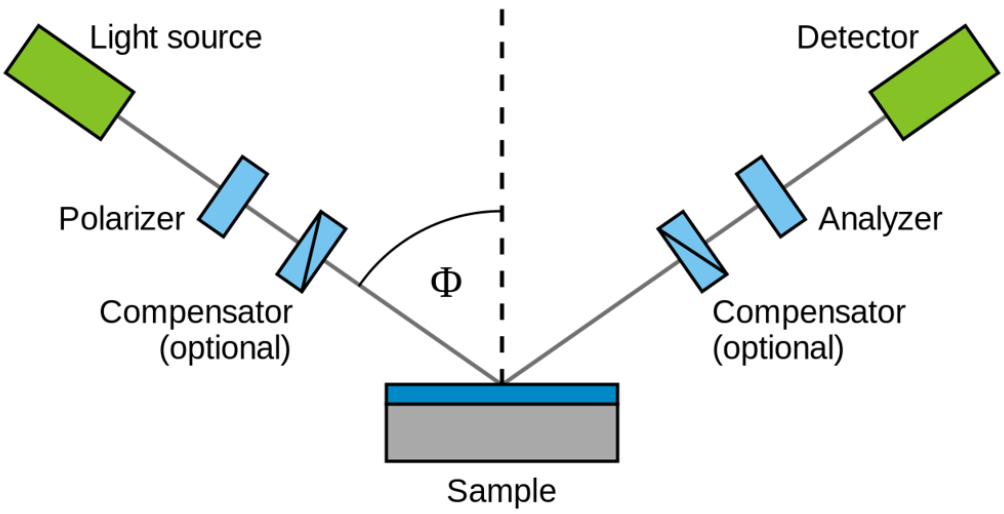

Figure 2.8: Illustration of an ellipsometry system [60].

The basic principle of ellipsometry is to measure the complex polarization change as determined by the properties of the material of interest. As illustrated in Fig. 2.8, the experimental setup consists of a light source, a detector, a polarizer and an analyzer. The incident beam and reflected beam construct the plane of incidence. Any arbitrary polarization can be decomposed into two components: the s-component (perpendicular to the plane of incidence) and p-component (parallel to the plane of incidence). Ellipsometry measures

the complex reflectance ratio ρ, which is defined as

$$\rho = \frac{r_p}{r_s} = \tan(\Psi)e^{i\Delta}, \tag{2.2}$$

where r_s and r_p are the normalized reflected s-component and p-component amplitudes, respectively; $\tan(\Psi)$ is the amplitude ratio upon reflection; and Δ represents the phase difference. Ellipsometry results are normally presented as Ψ and Δ. In most cases, Ψ and Δ cannot be directly converted to optical properties. Model analysis must be performed to fit the experimental data so that the property parameters can be extracted. However, for the characterization of refractive index of isotropic and homogeneous materials, direct conversion of Ψ and Δ is usually possible with thick "opaque" single-material films. All the refractive indices in this work are measured directly with thick single-material films prepared via magnetron sputtering on oxidized Si wafer.

2.2.3 X-ray Diffraction

X-ray diffraction (XRD) is a widely-used non-destructive technique for crystalline structure characterization. The principle of XRD is to enable the elastic scattering of x-rays from the periodic lattice of a crystalline material, and measure the resultant constructive interference of the reflected wave [61]. X-rays with wavelengths close to 0.1 nm are often used in XRD applications. The similarity between the x-ray wavelength and atomic spacing in the crystal makes scattering and interference significant, which helps reveal structural information.

As illustrated in Fig. 2.9, an intuitive model of XRD is the well-known Bragg's law [62], which states that constructive interference of reflected x-rays occurs under the condition

$$2d\sin\theta = n\lambda, \tag{2.3}$$

where d is the distance between adjacent lattice planes, θ is the incident angle of the x-ray, λ is the x-ray wavelength, and n is an integer number. Constructive interference only happens

when the distance traveled by two adjacent reflected rays differ by an integer number of the x-ray wavelength. By varying the incident angle θ, the interference condition gets satisfied for different lattice spacings. Therefore, the interference peak positions reveal structural information such as the lattice constant, crystal structure, and chemical composition. When the x-rays are incident at a small angle ($< 10°$), the diffraction pattern can be used to determine thin flim thicknesses. This technique is called x-ray reflectivity (XRR). In this dissertation, XRD is used to characterize the crystal structure of the magnetic materials, e.g. Fe, Co, and Ni studied in Chap. 5; and XRR is used to calibrate the sputtering deposition rate in the thin film preparation process.

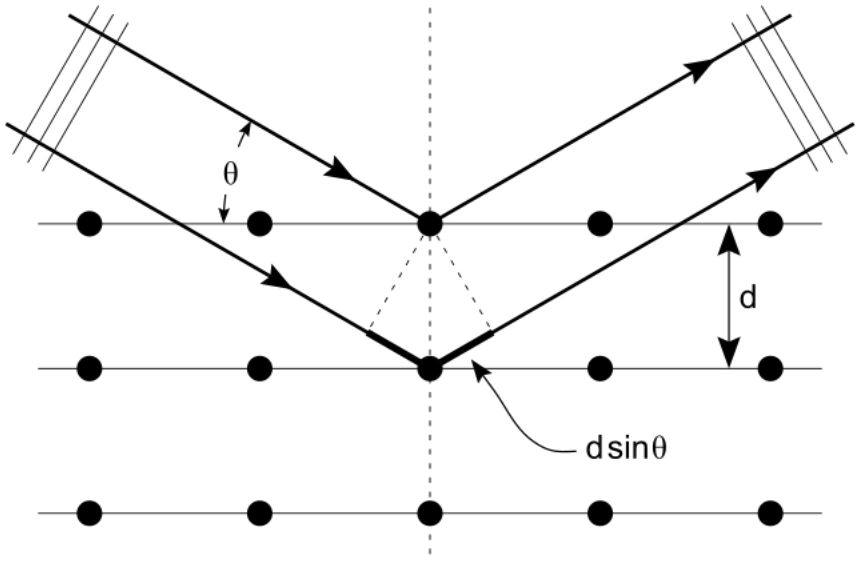

Figure 2.9: Illustration of Bragg diffraction. This figure is reproduced from Ref. [63].

Chapter 3

Magneto-Optic Kerr Effect Based Spin-Orbit Torque Magnetometer

Part of this chapter was published in "All-optical vector measurement of spin-orbit-induced torques using both polar and quadratic magneto-optic Kerr effects," by Xin Fan, Alex R. Mellnik, Wenrui Wang, Neal Reynolds, Tao Wang, Halise Celik, Virginia O. Lorenz, Daniel C. Ralph, and John Q. Xiao, Appl. Phys. Lett. **109**, 122406 (2016). In this work, Dr. Xin Fan conceived the idea and oversaw the whole project. Alex Mellnik performed the spin-torque ferromagnetic resonance (ST-FMR) measurement. Wenrui Wang conducted all the MOKE measurements and majority of the data analysis.

As discussed in the introducton, spin-orbit torques (SOTs) are promising candidates for realizing efficient electrical manipulation of magnetism [20, 30, 64–69], which may lead to new technologies for magnetic memory and logic devices [6, 70]. Recently, SOT-induced magnetic-moment manipulation was observed in both heavy metal/ferromagnet bilayers [30, 68, 71, 72] and topological insulator/ferromagnet bilayers [73, 74]. Exploration in this field, both for fundamental understanding and practical applications, requires a convenient method to quantitatively measure the amplitude and direction of the SOTs. To date, the workhorse methods for measuring such torques are based on using magneto-transport signals for detecting magnetic reorientations in response to an applied current. For example, second-harmonic Hall effect measurements work well for measuring torques acting on a metallic magnetic layer with perpendicular magnetic anisotropy, but for magnets with in-plane anisotropy, the need to separate out thermally-induced signals makes this technique more difficult to apply [71, 75, 76]. Spin-torque ferromagnetic resonance (ST-FMR) [30] can be

used for metallic magnets with either perpendicular or in-plane anisotropy, but for very thin magnetic layers an artifact caused by spin pumping and the inverse spin Hall effect could in principle interfere with this method [77]. Here, I introduce a simple all-optical technique based on the polar and quadratic magneto-optic Kerr effect (MOKE) for current-induced SOT characterization. The method has a sensitivity comparable to the techniques based on magneto-transport detection, but with fewer artifacts and applicability to a very wide range of magnetic materials.

In this chapter, I first explain the connection between the MOKE response and magnetization components in the normal incidence configuration. Then, I describe the experimental system and how we quantitatively calibrate the strength of the SOTs. Lastly, comparison between MOKE and ST-FMR results is presented to demonstrate the accuracy of the technique.

3.1 SOT-Induced Magnetization Reorientation

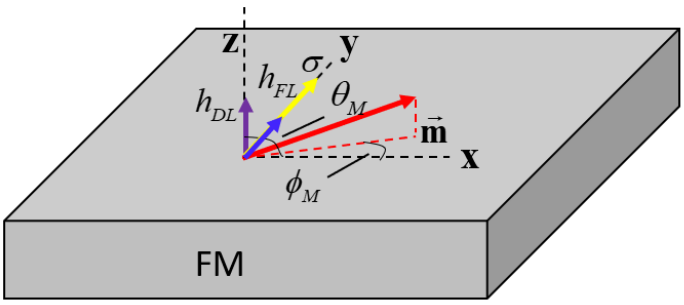

Figure 3.1: Illustration of the SOT-induced magnetization reorientation. For a magnetization initially aligned in the x-direction, an in-plane spin polarization σ in the y-direction leads to a DL-SOT effective field h_{DL} in the z-direction and a FL-SOT effective field h_{FL} in the y-direction. h_{DL} and h_{DL} cause out-of-plane and in-plane magnetization tilt, respectively.

As discussed in Chap. 1, when a spin current is absorbed by a magnetic material, it

exerts two kinds of SOT: (anti-)damping-like SOT (DL-SOT) and field-like SOT (FL-SOT). DL-SOT has the form of $\vec{m} \times (\vec{m} \times \vec{\sigma})$, while FL-SOT has the form of $\vec{m} \times \vec{\sigma}$. The effect of such torques on the magnetization can be equivalently expressed as effective magnetic fields: $h_{\mathrm{DL}} \propto \vec{m} \times \vec{\sigma}$ and $h_{\mathrm{FL}} \propto \vec{\sigma}$, respectively. As illustrated in Fig. 3.1, a spin current with spin polarization σ in the y-direction results in magnetization reorientation in both the xz- and yz-plane. Namely, DL-SOT causes the magnetization to tilt out of plane, while FL-SOT rotates the magnetization in plane.

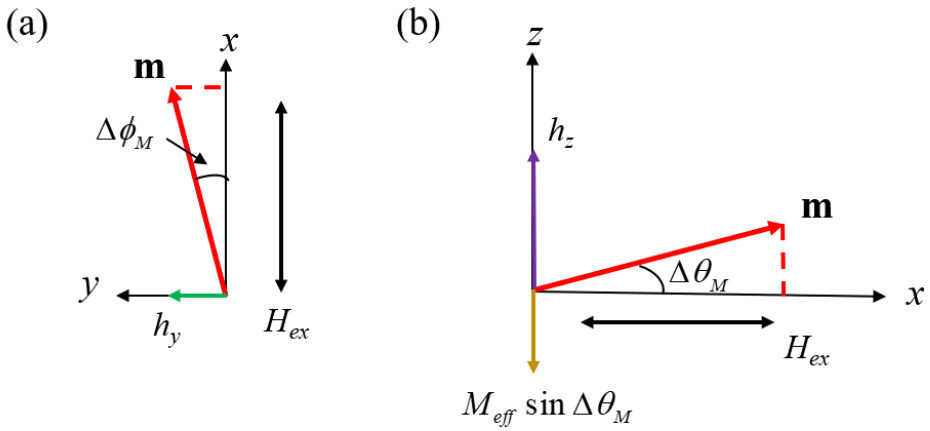

Figure 3.2: Illustration of the major fields that influence the magnetization reorientation in the (a) xy-plane and (b) xz-plane.

For an in-plane magnetized thin film, under the first-order approximation, the magnetization change under the effective SOT magnetic fields can be calculated. As shown in Fig. 3.2(a), assuming an external field in the x-direction and an effective field h_y in the y-direction, the in-plane magnetization rotation $\Delta\phi_M$ can be expressed as

$$\Delta\phi_M = \frac{h_y}{H_{\mathrm{ex}}}, \tag{3.1}$$

where $h_y = h_{\mathrm{FL}} + h_{\mathrm{OerstedIn}}$ is the superposition of the effective field of the FL-SOT and the in-plane current-induced Oersted field $h_{\mathrm{OerstedIn}}$, and H_{ex} is the external magnetic field.

On the other hand, as shown in the diagram of Fig. 3.2(b), the effect of an out-of-plane

effective field h_z is significantly suppressed by the demagnetizing effect, which results in an out-of-plane magnetization tilt $\Delta\theta_M$ that is not as sensitive to the external field H_{ex}:

$$\Delta\theta_M = \frac{h_z}{|H_{\text{ex}}| + M_{\text{eff}}}, \tag{3.2}$$

where $h_z = h_{\text{DL}} + h_{\text{OerstedOut}}$ represents the combination of h_{DL} and the out-of plane current-induced Oersted field $h_{\text{OerstedOut}}$; $M_{\text{eff}} = M_s - H_{\text{anis}\perp}$ is a term arising from demagnetization and surface anisotropy, which is normally much larger than H_{ex}, where M_s is the saturation magnetization and $H_{\text{anis}\perp}$ is the out-of-plane anisotropy field.

3.2 Polar and Quadratic MOKE in the Normal-Incidence Configuration

As introduced in Chap. 1, MOKE describes the change of light polarization upon reflection from a magnetized surface. In principle, MOKE can be described as arising from a magnetization-dependent permittivity tensor, which can be expressed as a Taylor series in the components of the magnetization unit vector $\mathbf{m}$ [42]:

$$\epsilon_{ij}(\mathbf{m}) = \epsilon_{ij}^{(0)} + \sum_k \epsilon_{ijk}^{(1)} m_k + \sum_{k,l} \epsilon_{ijkl}^{(2)} m_k m_l + ..., \tag{3.3}$$

where $i, j, k, l = x, y, z$. When light interacts with a magnetic material, the light polarization changes depending on the magnetization orientation. The second term on the right side of Eq. 3.3 generates the first-order MOKE, which includes the well-known polar, longitudinal, and transverse MOKE [78]. The third term on the right in Eq. 3.3 leads to the second-order MOKE, which is often referred as quadratic MOKE [79]. This term is in general not negligible.

For the case of normally-incident light with linear polarization, the change of the polarization angle due to the magnetization can be written as [80]

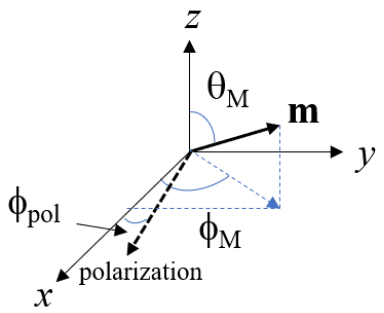

Figure 3.3: Illustration of the θ_M, ϕ_M and ϕ_{pol} in Eq. 3.5.

$$\Phi(\mathbf{m}) = \alpha_{\text{Polar}} m_z + \beta_{\text{Quadratic}} m_x m_y ..., \tag{3.4}$$

where the z-direction is perpendicular to the magnetic film plane, the x-direction is parallel to the plane of the incident polarization, and α_{Polar} and $\beta_{\text{Quadratic}}$ are the coefficients for the polar MOKE and quadratic MOKE responses, respectively. One way to distinguish the polar MOKE and quadratic MOKE responses is by tuning the polarization of the incident light. If we define θ_M and ϕ_M as the polar and azimuthal angles of the magnetization, and ϕ_{pol} as the angle of the polarization, as illustrated in Fig. 3.3, Eq. 3.4 can be rewritten (still assuming normally-incident light with linear polarization) as

$$\Phi_{\text{linear}}(\mathbf{m}) = \alpha_{\text{Polar}} \cos\theta_M + \frac{1}{2}\beta_{\text{Quadratic}} \sin^2\theta_M \sin[2(\phi_M - \phi_{\text{pol}})] + ... \tag{3.5}$$

As a result, the polar MOKE response does not depend on the polarization direction, while the quadratic MOKE depends on the polarization angle as $\propto \sin[2(\phi_M - \phi_{\text{pol}})]$.

Alternatively, if circularly-polarized incident light is used, the polar MOKE component yields no polarization change, while quadratic MOKE changes the polarization from circular to slightly elliptical. Using Jones matrices to calculate the change in polarization due to each optical element (a detailed derivation is given in Appendix.A2), the expected current-induced change in the polarization is

$$\Phi_{\text{circular}}(\mathbf{m}) = -\beta_{\text{Quadratic}}\Delta\phi_M. \tag{3.6}$$

Therefore, by controlling the polarization of the incident light, one can conveniently separate the two MOKE signals that are proportional to m_z and $m_x m_y$, and thus measure current-induced magnetization rotation that results in changes to any of the magnetization components.

3.3 Experimental Setup

Our MOKE system is an optical bridge apparatus using lock-in detection. The light source is a mode-locked Ti:Sapphire laser with a center wavelength of 780 nm. As shown in Fig. 3.4, a Glan-Thompson polarizer is used to prepare linear polarization at the beginning. The initial polarization is set along the x-direction. After a 50/50 beam splitter, a half (quarter) wave plate is used to further tune the laser polarization for polar (quadratic) MOKE measurement. The magnetization in the sample is altered by the applied current at a frequency of 20.15 kHz. After the laser is reflected from the sample, it is redirected by the 50/50 beam splitter towards the detector direction. Changes in the MOKE signal due to magnetization reorientation are analyzed by using a Wollaston prism to separate the s- and p-component of the light and then measuring the power difference with a balanced detector. SOT-induced changes in the MOKE signal, $\Delta\Phi(\mathbf{m})$, are recorded by a lock-in amplifier locked to the frequency of the applied current. (A Jones matrix calculation of the MOKE signal is included in Appendix.A4)

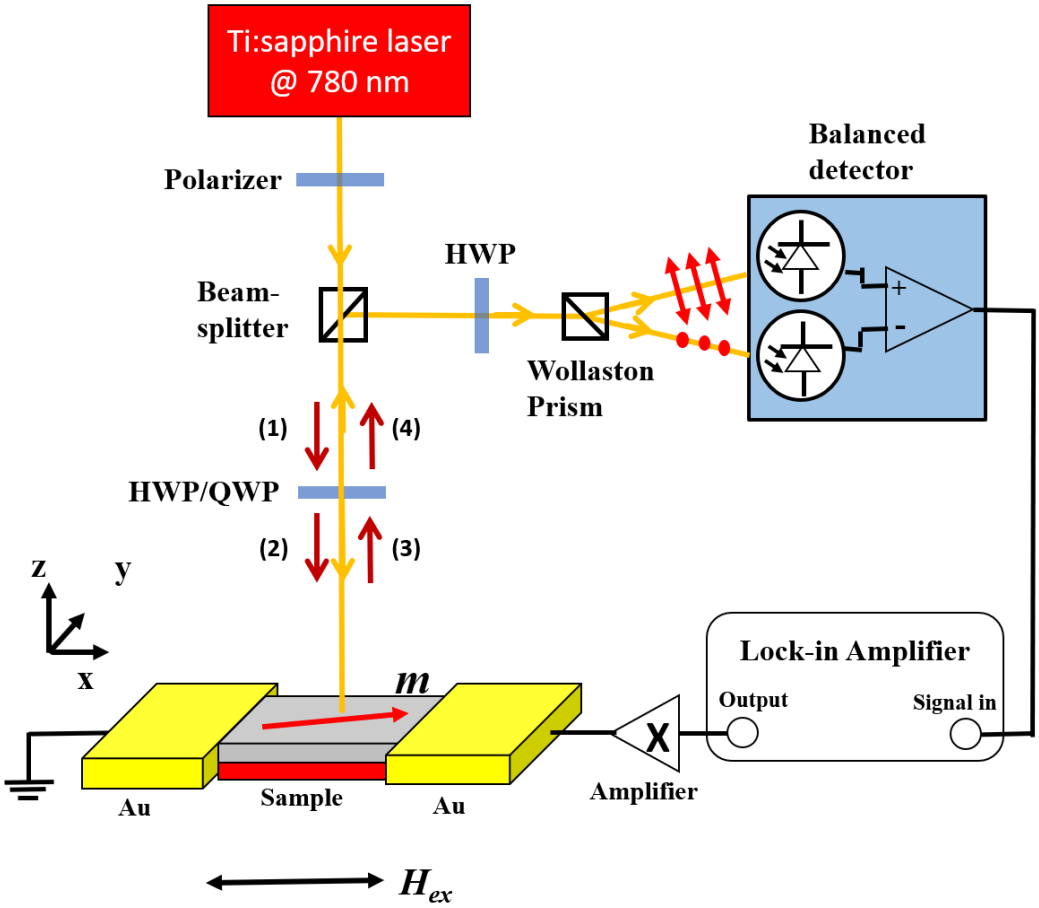

Figure 3.4: Experimental setup for the optical detection of SOTs. To detect the SOT-induced out-of-plane magnetization tilt, we use a half wave plate (HWP) before the sample. The half wave plate is replaced by a quarter wave plate (QWP) for measuring the in-plane magnetization rotation. The half wave plate before the Wollaston prism is initially set so that the s- and p-component of the polarization is balanced. Red arrows and dots in front of the balanced detector represent the light polarization direction.

Since we study small current-induced perturbations of the magnetization about an initial state at $\phi_M = 0$, $\theta_M = \frac{\pi}{2}$, by differentiation of Eq. 3.5, the expected change in the MOKE signal is (see Appendix.A3)

$$-\Delta\Phi(\mathbf{m}) = -\alpha_{\text{Polar}}\Delta\theta_M + \beta_{\text{Quadratic}}\cos 2\phi_{\text{pol}}\Delta\phi_M. \tag{3.7}$$

Combining Eq. 3.7 with Eqs. 3.1 and 3.2, we obtain an expression that relates the SOT-

induced magnetization reorientation to the detected MOKE signal. In the actual experiments, I extract the polar MOKE response by measuring the average of the signals at 45° and 135° incident polarization:

$$\Delta\Phi_{\text{Polar}} = \frac{\Delta\Phi(\phi_{\text{pol}} = 45°) + \Delta\Phi(\phi_{\text{pol}} = 135°)}{2} = \alpha_{\text{Polar}}\Delta\theta_M.$$

The purpose of measuring two polarization angles that are exactly 90 degrees apart is to minimize any residual quadratic MOKE signal due to small misalignment. Similarly, for the quadratic MOKE component, I measure the signal at 0° and 90° polarization angle and take half the difference as the result:

$$\Delta\Phi_{\text{Quadratic}} = \frac{\Delta\Phi(\phi_{\text{pol}} = 0°) - \Delta\Phi(\phi_{\text{pol}} = 90°)}{2} = \beta_{\text{Quadratic}}\Delta\phi_M.$$

Thanks to the low sensitivity of cosine function to angular misalignment at 0 and 90 degrees, this method is a good alternative to the quadratic MOKE method using circularly-polarized light, which contains no polar signal.

3.4 Calibration Method

We use calibration magnetic fields to quantitatively determine the strength of the SOTs from the measured MOKE signals. For the DL-SOT calculation, we use an out-of-plane calibration field, while an in-plane calibration field is utilized for extracting the FL-SOT.

The out-of plane calibration field is generated by a specially designed calibration wire, shown in Fig. 3.5(a). Given all the dimensions of the calibration wire, the generated calibration field h_{Cal} due to a certain calibration current can be calculated. Recalling the magnetization reorientation expression in Eq. 3.2, we can write down the MOKE signal due to the out-of-plane magnetization tilt caused by h_{Cal} as

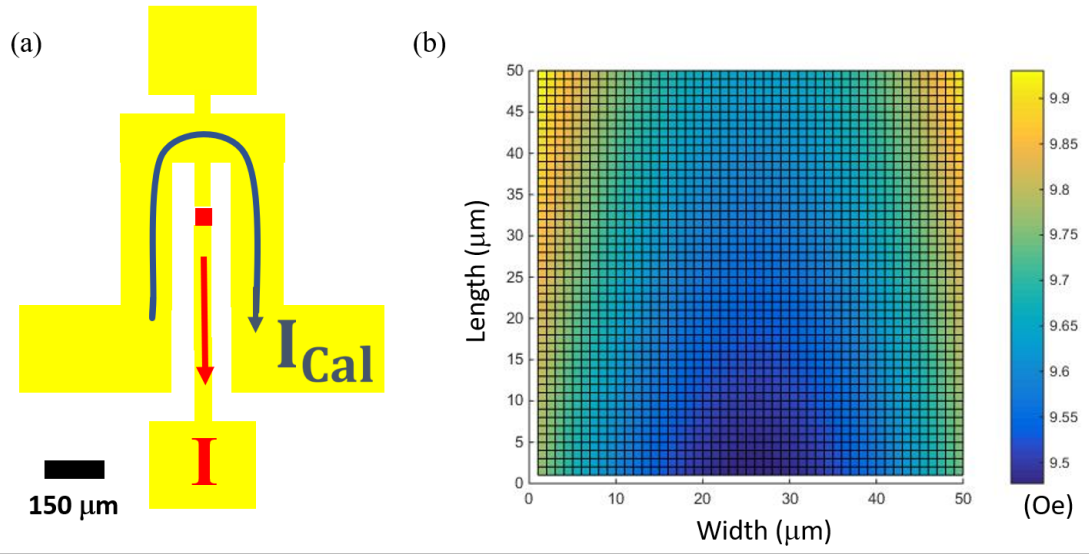

Figure 3.5: (a) Diagram of the designed calibration wire for out-of-plane calibration field. Calibration current is applied from the left to the right. (b) Generated out-of-plane Oersted field distribution for a calibration current of 400 mA. The 50 μm $\times$ 50 μm area is indicated by the red dot in (a). The values on the legend bar are in Oe.

$$\Delta V_{\mathrm{Cal}} = \alpha_{\mathrm{Polar}} \Delta\theta_M = \frac{h_{\mathrm{Cal}}}{|H_{\mathrm{ex}}| + M_{\mathrm{eff}}}. \tag{3.8}$$

Since the DL-SOT effective field, $h_{\mathrm{DL}} \propto \vec{m} \times \vec{\sigma}$, linearly depends on the magnetization, it changes sign when the external magnetic field H_{ex} reverses. Given $h_z = h_{\mathrm{DL}} + h_{\mathrm{OerstedOut}}$ and the Oersted field is independent of H_{ex}, the h_{DL}-caused magnetization tilt can be calculated as: $\Delta\theta_{h_{\mathrm{DL}}} = \frac{\Delta\theta_{h_z}(+H_{\mathrm{ex}}) - \Delta\theta_{h_z}(-H_{\mathrm{ex}})}{2}$. Therefore, the MOKE signal generated by the DL-SOT can be expressed as

$$\Delta V_{\mathrm{DL}} = \alpha_{\mathrm{Polar}} \Delta\theta_{h_{\mathrm{DL}}} = \frac{\Delta V(+H_{\mathrm{ex}}) - \Delta V(-H_{\mathrm{ex}})}{2} = \frac{h_{\mathrm{DL}}}{|H_{\mathrm{ex}}| + M_{\mathrm{eff}}}. \tag{3.9}$$

From Eqs. 3.8 and 3.9, we derive the final equation to calculate the effective magnetic field due to the DL-SOT as

$$h_{\mathrm{DL}} = \frac{\Delta V_{\mathrm{DL}}}{\Delta V_{\mathrm{Cal}}} h_{\mathrm{Cal}}. \tag{3.10}$$

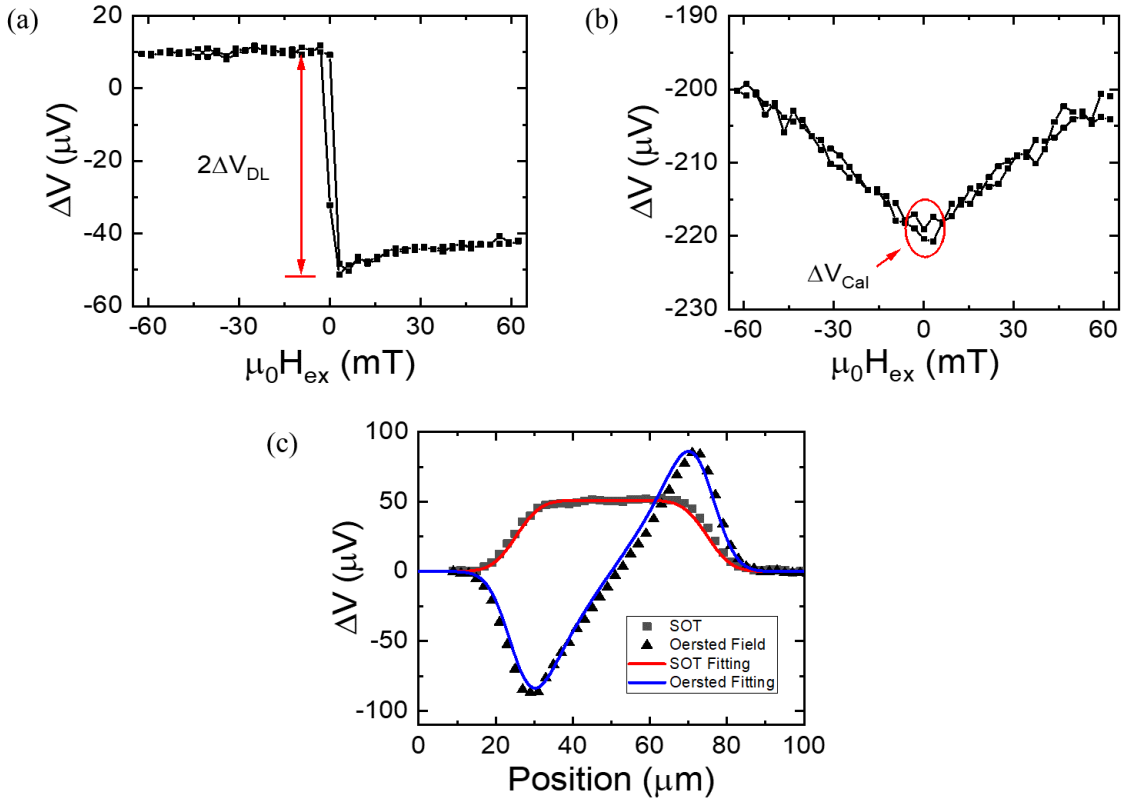

Figure 3.6: Illustration of the DL-SOT calibration process. (a) The h_{DL}-induced MOKE signal. The signal has a step-like shape because of the change of sign of h_{DL} on magnetization reversal, as described by Eq. 3.9. (b) the MOKE signal due to the calibration field. The symmetric tilted shape is described by Eq. 3.8. (c) The signals used to extract h_{DL} via a line-scan method, for comparison.

We verified the accuracy of this method by comparing its result with the result of a line-scan method [81]. The line-scan method utilizes the different symmetries of h_{DL} and $h_{\mathrm{OerstedOut}}$. By measuring the overall MOKE signal across the sample width under positive and negative external magnetic fields, signals due to h_{DL} and $h_{\mathrm{OerstedOut}}$ are extracted through simple addition and subtraction. Since the current-induced Oersted field can be readily calculated with Ampere's law, we can calibrate the amplitude of h_{DL} through fittings of the SOT and Oersted curves, shown in Fig. 3.6(c). Although the line-scan method is self-calibrated, which means no extra calibration field is needed, it is also more time-consuming. Therefore, we replace the line-scan method in our experiments. A sample with the structure,

substrate/Py(20)/Pt(3), was used in the comparison experiment, where the values in the parenthesis are in nanometers. Fig. 3.6(a) and (b) show the polar MOKE signal of the DL-SOT measurement and the calibration measurement, respectively. The MOKE signal due to the DL-SOT, $\Delta V_{\mathrm{DL}} \approx -30\ \mu$V, is extracted from Fig. 3.6(a) by taking half the difference between the positive field and the negative field signals. And, the calibration signal, $\Delta V_{\mathrm{Cal}} \approx -220\ \mu$V, is the zero-field reading in Fig. 3.6(b). Since the calibration current is 400 mA, which corresponds to a calibration field $h_{\mathrm{Cal}} = 9.6$ Oe, the DL-SOT-induced effective field can then be computed using Eq. 3.10 to be $h_{\mathrm{DL}} = 1.3 \pm 0.2$ Oe. This result is in good agreement with the self-calibrated line-scan result, $h_{\mathrm{DL}} = 1.1 \pm 0.2$ Oe, that is extracted from Fig. 3.6(c).

Applying the same methodology, we use an in-plane calibration field for the FL-SOT measurements. The in-plane field is generated by a 2 mm wide straight wire on a PCB board, that we attach underneath the sample with the wire parallel with the current direction (x-direction). The wide width of the wire ensures a relatively uniform in-plane (y-direction) Oersted field across the sample area. Since both the FL-SOT effective field h_{FL} and in-plane calibration field h_{CalIn} rotate the magnetization in the xy-plane, from Eqs. 3.1 and 3.7, we can write the quadratic MOKE signal due to h_{FL} and h_{CalIn} as

$$\Delta V_{\mathrm{FL}} = \beta_{\mathrm{Quadratic}} \Delta\phi_{h_{\mathrm{FL}}} = \frac{h_{\mathrm{FL}} + h_{\mathrm{OerstedIn}}}{H_{\mathrm{ex}}}, \tag{3.11}$$

$$\Delta V_{h_{\mathrm{CalIn}}} = \beta_{\mathrm{Quadratic}} \Delta\phi_{h_{\mathrm{CalIn}}} = \frac{h_{\mathrm{CalIn}}}{H_{\mathrm{ex}}}, \tag{3.12}$$

where $h_{\mathrm{OerstedIn}}$ is the Oersted field generated by the current that generates the SOTs.

As shown in Fig. 3.7(a) and (b), both the FL-SOT and calibration quadratic MOKE signals yield nice $1/H_{\mathrm{ex}}$ dependence as predicted by Eqs. 3.11 and 3.12. By replotting the FL-SOT result as a function of the calibration values and performing a linear regression fitting (Fig. 3.7(c)), we extract a slope value, which is equal to the ratio of $\frac{h_{\mathrm{FL}}+h_{\mathrm{OerstedIn}}}{h_{\mathrm{CalIn}}}$.

Since h_{CalIn} and $h_{\mathrm{OerstedIn}}$ can be calculated with Ampere's law, the strength of the FL-SOT effective field can be quantitatively determined as

$$h_{\mathrm{FL}} = \mathrm{slope} \times h_{\mathrm{CalIn}} - h_{\mathrm{OerstedIn}}. \tag{3.13}$$

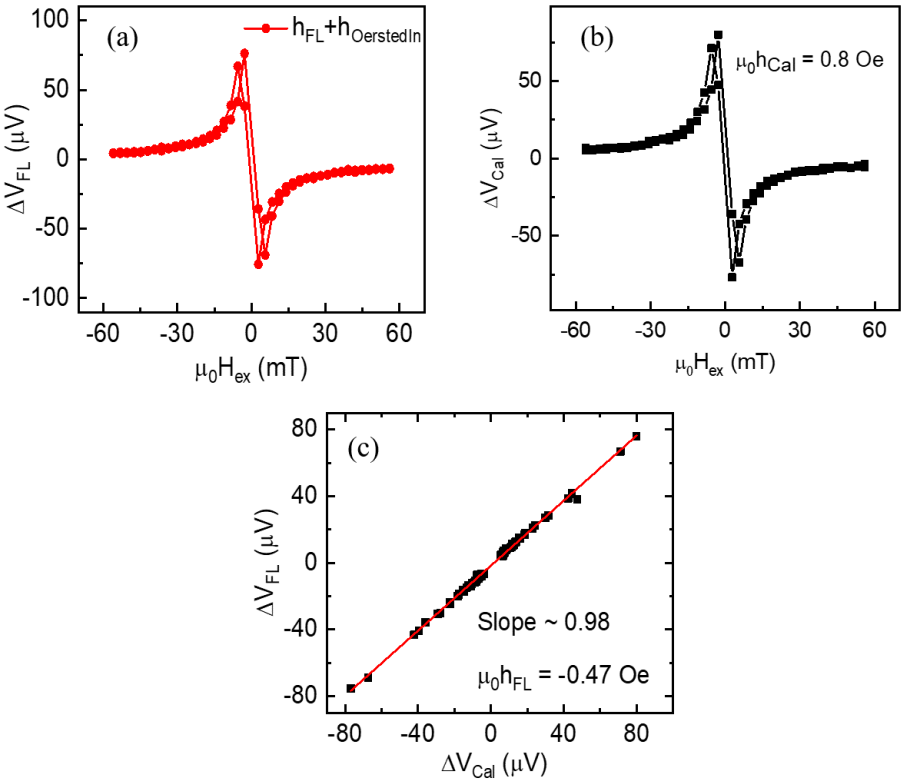

Figure 3.7: Illustration of the FL-SOT calibration process. (a) Quadratic MOKE signal of the FL-SOT. The signal includes contributions from the current-induced FL-SOT and the in-plane Oersted field generated by the same current. (b) The quadratic MOKE signal of the in-plane calibration field. Both (a) and (b) follow a clear $1/H_{\mathrm{ex}}$ dependence. (c) Plot of the FL-SOT MOKE signal as a function of the calibration-field-induced signal. The slope of the linear fit can be used to extract the amplitude of the effective field of FL-SOT. The negative sign before the field value indicates the direction of the h_{FL} is opposite to the calibration field direction.

3.5 Results

We demonstrate the current-induced SOT measurement using polar and quadratic MOKE with a Py/Pt bilayer sample. The sample has the structure: substrate/Pt(6)/Py(8)/AlO_x(3), where values in the parenthesis are in nanometers. We measure the MOKE response as a function of external magnetic field H_{ex} for different incident polarizations. As shown in Fig. 3.8(a), for $\phi_{pol} = 45°$, we observe a simple hysteresis-like change in the signal near zero field with the signal approximately independent of H_{ex} on either side of the step. This result agrees with the expectation from Eq. 3.7, in which the contribution from the quadratic MOKE is zero. This is also the behavior expected from the polar Kerr signal, with the step near $H_{ex} = 0$ due to reversal of the magnetization, and with the weak magnetic-field dependence away from the step consistent with Eq. 3.2 for $H_{ex} \ll M_s$. As the polarization angle is rotated so that ϕ_{pol} differs from 45°, the form of the magnetic-field dependence of the current-induced MOKE signal changes dramatically, evolving from a simple step to the superposition of a step with an additional component that is approximately inversely proportional to H_{ex}. This is the signature of a significant quadratic MOKE signal in addition to the polar MOKE response, with current-induced magnetization rotation within the sample plane providing the $1/H_{ex}$ dependence according to Eq. 3.1.

An out-of-plane effective field of $\mu_0 h_{DL} = 0.068 \pm 0.010$ mT at a 10 mA current bias is extracted from the calibration, based on which we extract the polar MOKE coefficient α_{Polar} to be $(5.8 \pm 0.8) \times 10^{-3}$. Using a simple parallel circuit model to account for the different resistivities of Pt and Py, we estimate that approximately 42% of the current flows through the Pt, yielding a current density in the Pt of $j_{Pt} = 1.4 \times 10^{10}$ A/m^2. If we assume all of the DL-SOT is due to the spin Hall effect in the Pt layer, we determine a spin Hall angle $\Theta_{Pt} = (2e/\hbar)\mu_0 h_{DL} M_s d_{Py}/j_{Pt} = 0.082 \pm 0.012$ [29]. This is consistent with the spin-Hall angle of Pt extracted using other torque-based measurement techniques [29, 77].

On the other hand, we show circularly polarized light is only sensitive to the quadratic

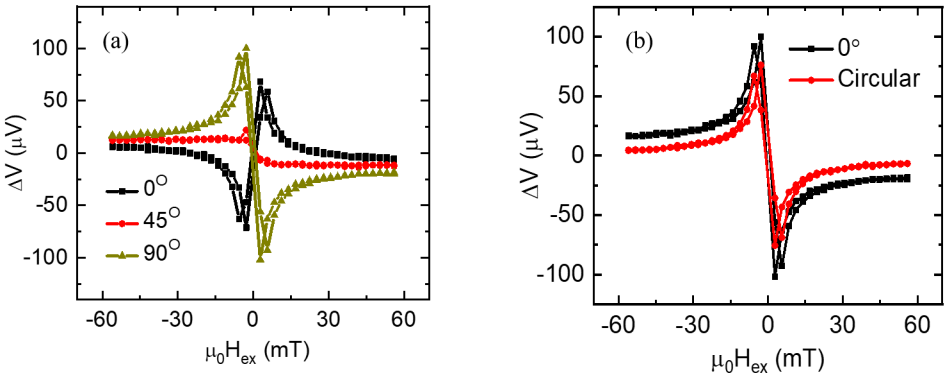

Figure 3.8: (a) Current-induced polar MOKE response with three different incident linear polarization angles. (b) Current-induced MOKE response with circularly polarized light and 0° linearly polarized light. The former only contains quadratic MOKE response ($1/H_{\mathrm{ex}}$-like) while the latter is a superposition of a quadratic MOKE response and a polar MOKE response (which has a step-like dependence on H_{ex}).

MOKE term in Fig. 3.8(b). Compared to the MOKE response for linear polarization at $\phi_{\mathrm{pol}} = 0°$, the MOKE signal for circular polarization yields no hysteresis-like polar MOKE contribution, while the $1/H_{\mathrm{ex}}$ quadratic MOKE component is retained. This result is consistent with our expectation based on Eq. 3.6. From the calibration method introduced in the previous section, for a 10 mA current bias, the effective field due to FL-SOT is found to be $\mu_0 h_{\mathrm{FL}} = 0.500 \pm 0.005$ mT, which gives a quadratic MOKE coefficient of $\beta_{\mathrm{Quadratic}} = (1.1 \pm 0.1) \times 10^{-4}$. The uncertainty arises mainly from the inaccuracy of calculating the calibration field amplitude.

We also determine how the Kerr coefficients in Eq. 3.7 depend on the polarization angle. Within the linear response regime, the current-induced MOKE signal in general should be described as

$$\Delta\Phi(\mathbf{m}) = a(\phi_{\mathrm{pol}})\Delta\theta_M + b(\phi_{\mathrm{pol}})\Delta\phi_M, \tag{3.14}$$

where $a(\phi_{\mathrm{pol}})$ and $b(\phi_{\mathrm{pol}})$ are the MOKE coefficients that may depend on the polarization angle while $\Delta\theta_M$ and $\Delta\phi_M$ are the current-induced polar and azimuthal magnetization

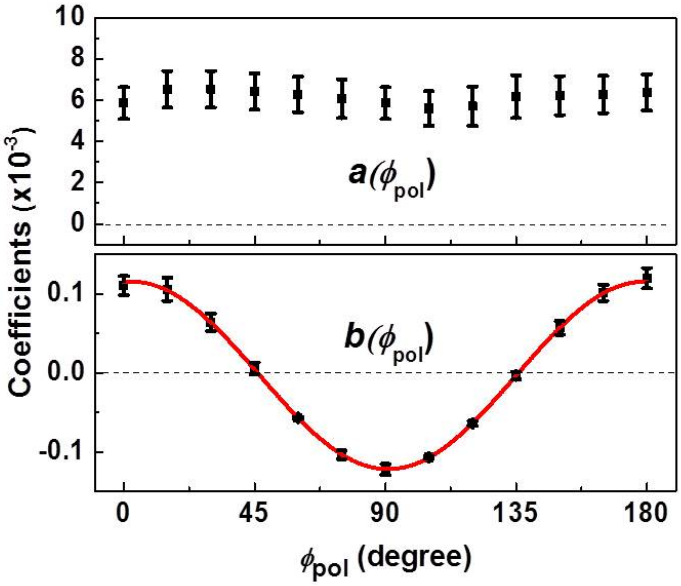

Figure 3.9: MOKE coefficients plotted as a function of laser polarization. The red curve in the bottom panel is a sinusoidal fit to $\cos(2\phi_{\mathrm{pol}})$.

change, which are independent of the polarization. Based on Eq. 3.7, $a(\phi_{\mathrm{pol}})$ is independent of polarization angle, while $b(\phi_{\mathrm{pol}})$ is proportional to $\cos(2\phi_{\mathrm{pol}})$. As shown in Fig. 3.9, the extracted MOKE coefficients confirm the prediction in Eq. 3.7.

It is worth mentioning that the magnitude of α_{Polar} is almost two orders of magnitude greater than $\beta_{\mathrm{Quadratic}}$, which is perhaps not surprising given that polar MOKE is a first-order process and quadratic MOKE is second-order. Nevertheless, because the out-of-plane magnetization reorientation $\Delta\theta_M$ is strongly suppressed by the demagnetization effect, the measured quadratic MOKE signal can still exceed the polar MOKE response in our thin-film bilayer samples.

3.6 Comparison with the Spin-Torque Ferromagnetic Resonance (ST-FMR) Results

To further verify the accuracy of our MOKE-based spin-orbit torque magnetometer, we measured samples with varying Py thickness: wafer/Pt(6)/Py(d_{Py})/AlO_x, with $d_{Py} = 2-10$ (values in parenthesis are in nanometers), and compared the results to ST-FMR performed on the same samples. We perform ST-FMR following the procedures described in Ref. [74]: we apply a microwave current to the sample through a coplanar waveguide structure and detect a magnetic resonance signal via a rectified dc voltage. The magnitude of the symmetric part of the resonance allows a determination of the damping-like torque, and the anti-symmetric part yields the in-plane effective-field component. The microwave current flowing through the sample is calibrated from a microwave reflection measurement; we do not assume as in Ref. [29] that the effective field component of the current-induced torque is due entirely to the Oersted field. We plot in Fig. 3.10(a) the measured current-induced equivalent fields h_{DL} (antidamping component) and h_{FL} (effective-field component) determined by both MOKE and ST-FMR as a function of d_{Py}. These measured fields are normalized by the total surface current density (I_{tot}/w), where w is the width of the sample. The two measurement techniques are in excellent quantitative agreement for both components. The strengths of both components of the equivalent field decrease as a function of increasing d_{Py} in part because this corresponds to a decrease in the current density flowing in the Pt layer. However, the dependences on d_{Py} are different for the two components. This is as expected due to the physical differences between the antidamping spin Hall torque that acts at the interface of the magnetic layer and the in-plane Oersted field that acts throughout the thickness of the magnetic layer.

In Fig. 3.10(b), we take the measurements of the antidamping component from Fig. 3.10(a) and replot them in the form of a surface torque normalized by the current density flowing just in the Pt layer, $\tau_{DL} = h_{DL}\mu_0 M_s d_{Py}$, where τ_{DL} is the surface damping-like torque, and

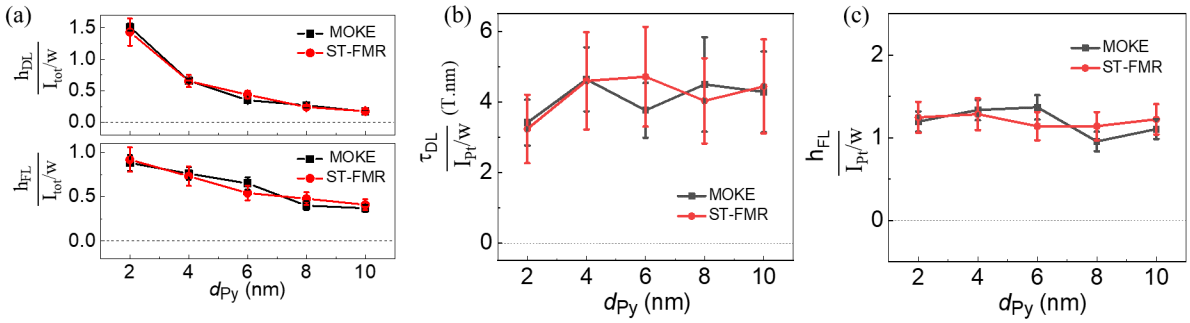

Figure 3.10: (a) The equivalent current-generated fields corresponding to the damping-like component h_{DL} and the in-plane effective-field-like component h_{FL} normalized by the total current I_{tot} per unit lateral width w in the bilayer, as a function of Py thickness d_{Py}. The uncertainties for the MOKE technique mostly arise from the fitting, while the uncertainties for the ST-FMR are mainly due to the determination of the microwave current. Excellent agreement is found between the MOKE and ST-FMR techniques. Lines are guides for eyes. (b) The damping-like torque τ_{DL} normalized by the estimated current per unit sample width w in the Pt layer. (c) The in-plane equivalent field h_{FL} normalized by the estimated current per unit sample width I_{Py}/w in the Pt layer.

$\mu_0 M_s = 1.0$ T is the saturation magnetization of Py. The current density in the Pt layer is estimated from the measured resistivities of Pt and Py films, assuming the Pt and Py films are two resistors in parallel. Over most of the range of Py thickness the torque is independent of d_{Py}, as expected for the surface torque due to the spin Hall effect arising from the Pt layer. The corresponding averarge spin Hall angle is 0.075 ± 0.010. There may be a small decrease in the strength of the torque for the 2 nm Pt layer, which is interesting in that it could hint at a decreased efficiency in the absorption of the incoming spin current for a very thin Py layer.

In Fig. 3.10(c), we replot the data for the in-plane effective field h_{FL} taken from Fig. 3.10(a), but normalized versus the estimated current per unit lateral sample width w flowing just in the Pt layer rather than the total current. For a pure Oersted field, the value should be 0.5 ($h_{\mathrm{OerstedIn}} = \frac{I}{2w}$ from Ampere's law), independent of Py thickness. We find that the measured equivalent field is indeed independent of d_{Py}, but the magnitude is somewhat larger than expected from a pure Oersted field. This discrepancy could be due to an inaccuracy

in our simple parallel circuit model for estimating the current in the Pt (we neglect surface scattering, for example) or to the existence of a spin-orbit-induced effective field with an unexpected dependence on d_{Py}.

3.7 Conclusion

In conclusion, we have demonstrated a convenient all-optical technique that can separately measure the antidamping-like and effective-field-like components of current-induced spin-orbit torque via polar MOKE and quadratic MOKE, respectively, with both measurements performed using normally-incident light. Excellent agreement between the results of this technique and that of ST-FMR measurements for a series of Pt/Py bilayers with different Py thicknesses verifies the validity of this method. We anticipate that MOKE magnetometry will be useful for rapid characterization of current-induced torques acting on a very wide range of materials. In particular, this method can be applied to magnetic bilayers with perpendicular magnetization. Being able to separately detect the out-of-plane and in-plane magnetization tilt, MOKE magnetometry may simplify the extraction of spin-orbit torques compared to second-order harmonics technique, which is complicated by the coexistence of the planar Hall, anomalous Hall, and thermal effects [82]. Due to these above mentioned advantages, I use this technique throughout my dissertation research.

Chapter 4

Enhanced Signal-to-Noise Ratio in an Unbalanced MOKE System

The previous chapter demonstrated that MOKE-based SOT magnetometry is a convenient and sensitive tool in current-induced spin-orbit effect studies. The relatively high (tens of nrad) sensitivity is sufficient for most of the SOT measurements involving ferromagnetic materials. However, in some fundamental experiments, such as detecting the current-induced spin accumulation in heavy metals [83–86] and topological insulators [87, 88], where the weak signal is comparable to the system noise floor, a better signal-to-noise (S/N) ratio is highly desired. In this chapter, I first carry out a systematic noise analysis for our SOT magnetometer. Based on the finding that the detector shot noise is the dominating noise source in our system, I propose an "unbalanced detection" method to enhanced the S/N ratio. Experimental demonstrations with a Pt/Py bilayer sample is presented to verify the validity of the technique. Lastly, I discuss how imperfect linear polarization can significantly attenuate the S/N enhancement.

4.1 System Noise Calibration

Thanks to the lock-in detection technique we use in our system, most of the environmental noise and thermal artifacts are filtered out. One possible noise source is the optical power variation due to the instability of the laser. However, at the power level (mW) and wavelength (780 nm) we normally use, the power variation is below 1%, which is at least one order of magnitude smaller than the detected noise level. Therefore, the main noise contributors are the output noise (thermal noise) of the balanced detector, the electron shot noise in the

detector and the lock-in amplifier noise:

$$\text{Total Noise} \simeq \text{Detector White Noise} + \text{Shot Noise} + \text{Lock-in Noise}.$$

Among these three sources, within the lock-in sensitivity range (below 50 μm) we normally use, the lock-in noise is dominated by the input noise (thermal noise), which is only 6 nV/$\sqrt{\text{Hz}}$ [89] at 20 kHz. For a equivalent noise bandwidth (ENBW) of 0.81 Hz, this noise is negligible in this analysis. The detector thermal noise should be a constant at different powers of the incident light. And, the electron shot noise should have a $\sqrt{\text{power}}$ dependence [90].

I conduct an optical power-dependent noise analysis to find the main source of the system noise. I take advantage of the "X Noise" function [89] in the SR-830 lock-in amplifier to measure the signal noise at 20 kHz as a function of incident light power at the balanced detector. As shown in the Fig. 4.1, the system noise has a very nice $\sqrt{\text{power}}$ dependence, which suggests that shot noise may be the dominant noise source. The y-intercept of the fitting line should be the detector white noise value.

To verify this hypothesis, I estimate the detector white noise and shot noise based on the device specifications. According to manual of the Nirvana model 2007 detector, the detector white noise is lower than 3 pW/$\sqrt{\text{Hz}}$ [91]. Given the detector DC conversion gain is 0.1×10^6 V/W, I calculate the upper bound of the detector white noise as

$$N_{\text{Detector}} \ < \ 3 \text{ pW}/\sqrt{\text{Hz}} \ \times \ 10^5 \text{ V/W} \ = \ 0.3 \ \mu\text{V}/\sqrt{\text{Hz}}, \tag{4.1}$$

where N_{Detector} is the detector white noise. This result is slightly larger than the measured value (0.22 μV/$\sqrt{\text{Hz}}$), which is reasonable because the calculated result is the upper bound.

One the other hand, the electron shot noise originates from the uneven statistical distribution of electrons in the current. It increases linearly with the square root of the current amplitude as

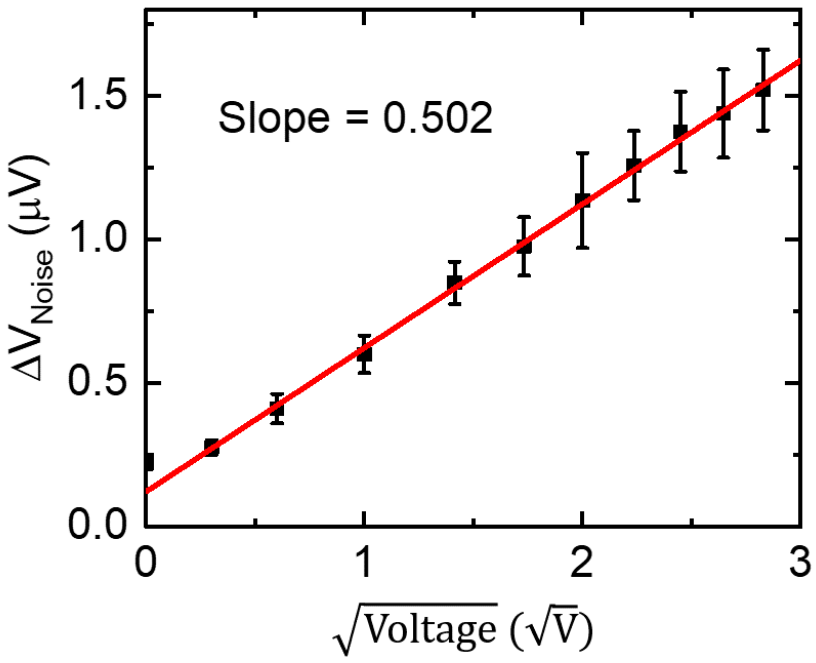

Figure 4.1: Illustration of the system noise as a function of the square root of the incident light power. Here, voltage is the corresponding DC voltage output of the balanced detector due to the incident light. The conversion relation is 1 mW = 10 V.

$$N_{\text{Shot}} = (2\text{qI} \times \text{ENBW})^{1/2}\ \text{A}/\sqrt{\text{Hz}}, \tag{4.2}$$

where q is the electron charge. Given the detector's transimpedance gain is 10^5 V/A, the light-induced electric current in the detector can be calculated as $I = \frac{x\text{V}}{1\times10^5\text{V/A}} = 10x\ \mu\text{A}$, where x is the DC voltage output from one photodiode caused by the light. Therefore, based on Eq. 4.2, the shot noise due to optical power that is equivalent to x volts DC voltage can be estimated as

$$N_{\text{Shot}} = (2\text{qI} \times \text{ENBW})^{1/2}\ \text{A}/\sqrt{\text{Hz}} = 0.509\sqrt{x}\mu\text{V}/\sqrt{\text{Hz}}. \tag{4.3}$$

The calculated slope matches the one extracted from experiment very well, which confirms the electron shot noise is the predominant noise source.

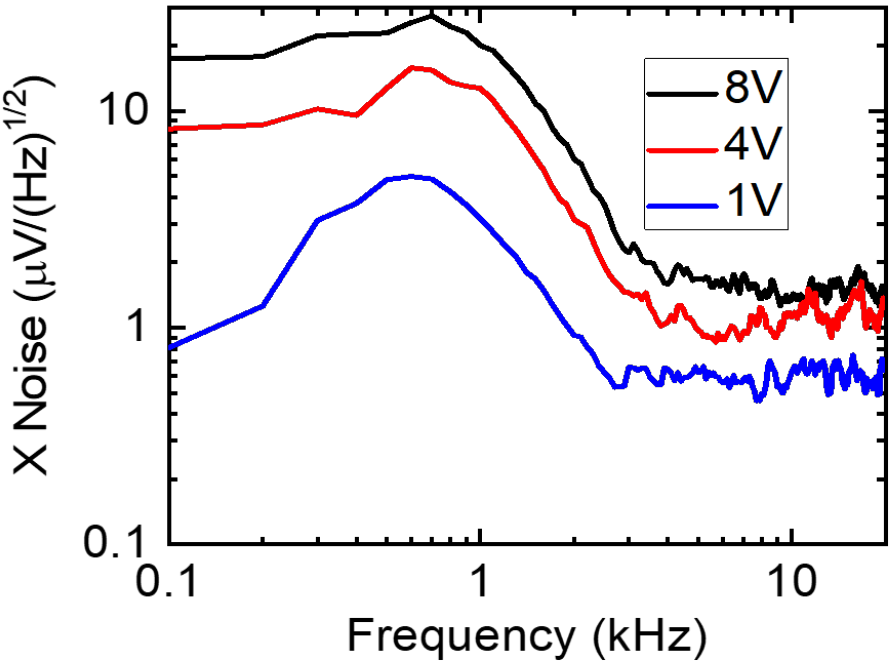

Figure 4.2: System noise as a function of lock-in modulation frequency.

In addition to the power-dependent study, I also measure the system noise as a function of the modulation frequency. As shown in Fig. 4.2, for all the three incident powers, the system noise doesn't change significantly with the modulation frequency after about 3 kHz. Therefore, my result at 20 kHz is reliable. However, special attention is needed with the huge spikes in the low frequency region. My suggestion is that only a modulation frequency higher than 5 kHz should be used.

Since MOKE is a linear effect, the MOKE signal should increase linearly with the optical power. On the other hand, as discussed above, the system noise is dominated by the electron shot noise, which follows a $\sqrt{\text{power}}$ dependence. Therefore, the S/N ratio of the system should be proportional to $\sqrt{\text{power}}$. Intuitively speaking, we can simply reach the optimal S/N ratio by increasing the optical power as much as possible. However, the balanced detector can only take a maximum power of 1 mW before it saturates. Thus, further enhancement of the S/N ratio is mainly limited by the highest optical power that the detector can handle.

Alternatively, we can also increase the detector gain to improve the shot-noise-related S/N ratio. The power to voltage conversion gain can be calculated as

$$\text{ConversionGain(V/W)} = \text{Responsivity(A/W)} \times \text{TransimpedanceGain(V/A)}.$$

If we increase the transimpedance gain by 16 times, we only need $\frac{1}{16}$ optical power to get the same signal. As for the noise, due to the same responsivity, the current in the circuit will be $\frac{1}{16}$, which leads to only a quarter of the initial noise. Therefore, we can improve the S/N ratio by a factor of 4. However, by increasing the gain of the detector, we will also amplify other noise such as the thermal noise from the input. Therefore, the optimal choice of the balanced detector depends on a trade-off between the shot noise and other current-independent noise sources.

4.2 Unbalanced Optical Bridge Method

To make more S/N ratio enhancement possible, we propose an "unbalanced" optical bridge technique to get around the power limitation of the detector. The basic idea of this method is to increase the incident power at the sample, while keeping the light reaching the balanced detector constant. As a result, the MOKE signal can be enhanced by the increased power on the sample, but the noise stays the same due to the constant power at the detector. The modified system is illustrated in Fig. 4.3. The setup should always be initially balanced so that the initial power at the sample and its corresponding voltage output from the detector can be recorded. Then, instead of fixing the half-wave-plate fast axis at 22.5° as in the balanced system shown in Fig. 3.4, we tune it to a new angle so that the voltage output (power) stays the same at one arm of the detector as we increase the optical power on the sample. The extra power distributed to the other arm is then attenuated by an variable neutral density (ND) filter before it goes to the detector. Therefore, the two arms can still

be balanced for measurement.

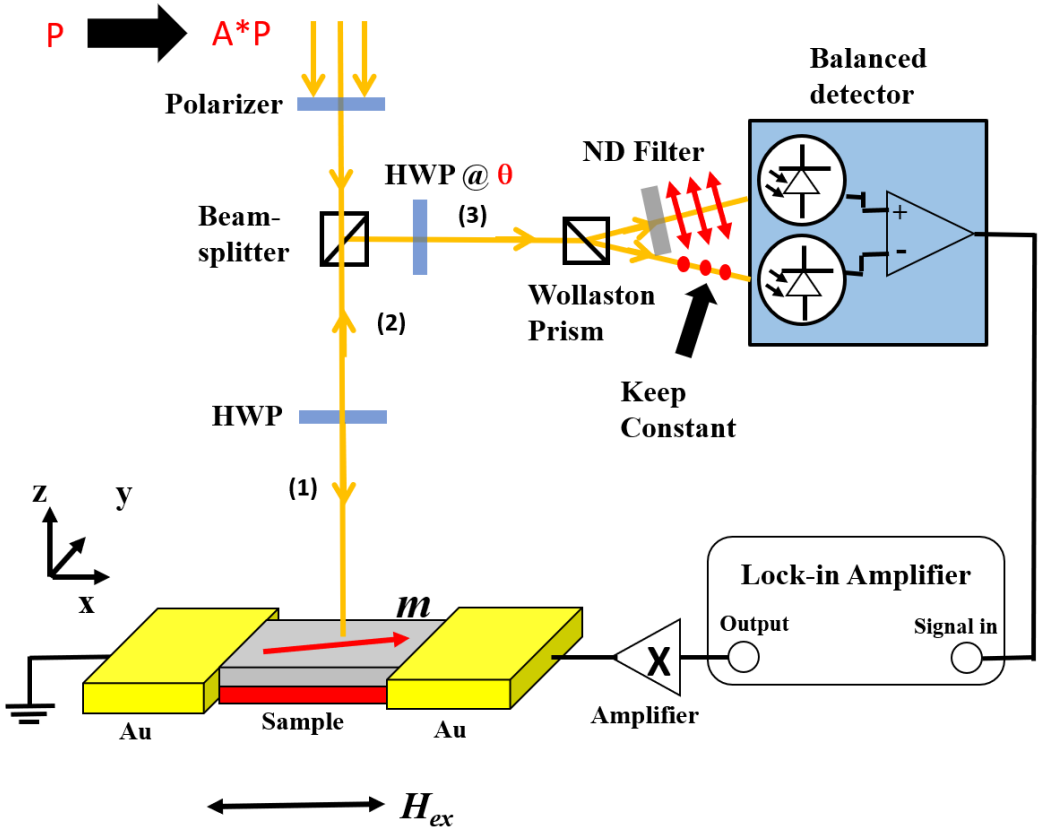

Figure 4.3: Illustration of the unbalanced optical bridge system. P is the initial optical power for the balanced system; A is the power amplification factor; θ represents the angle between the fast axis of half wave plate and vertical (s-polarization) direction. Red arrows and dots in front of the balanced detector represent the light polarization directions.

Here, I use Jones matrix calculus to derive the relation between the S/N improvement and the power amplification. Following a similar procedure as used in Appendix.A, the polarization states at each stage of the "unbalanced" system can be calculated as

$$(1) : P_1 = \begin{bmatrix} 1 \\ 0 \end{bmatrix},$$

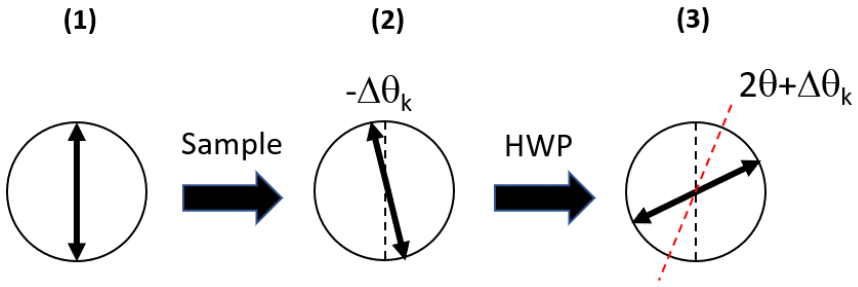

Figure 4.4: Illustration of the light polarization state at each stage through the unbalanced optical bridge system. Red dashed line indicates the fast axis direction of the wave-plates, which is at θ degrees.

$$(2) : P_2 = \begin{bmatrix} \cos\Delta\theta_K \\ \sin\Delta\theta_K \end{bmatrix},$$

$$(3) : P_3 = \begin{bmatrix} \cos(2\theta + \Delta\theta_K) \\ -\sin(2\theta + \Delta\theta_K) \end{bmatrix},$$

where the indices indicate the stage number as illustrated in Fig. 4.4. Assuming the power amplification factor is A and the attenuation factor due to the ND factor is B, the final re-balanced system with the same noise level requires the following relations (assuming $\Delta\theta_K$ is small compare to θ):

$$\sqrt{A}\sin 2\theta = \frac{\sqrt{2}}{2}, \tag{4.4}$$

$$\sqrt{AB}\cos 2\theta = \frac{\sqrt{2}}{2}. \tag{4.5}$$

Using Eq. 4.4 and 4.5, the MOKE signal from the unbalanced system can be simplified as

$$\text{Output}' = |\sqrt{A}\sin(2\theta + \Delta\theta_K)|^2 - |\sqrt{AB}\cos(2\theta + \Delta\theta_K)|^2 \simeq A(1+B)(\sin 4\theta)\Delta\theta_K. \tag{4.6}$$

Recalling the MOKE signal in the balanced system is $2\Delta\theta_K$, we get the signal enhancement from using the unbalanced optical bridge technique:

$$\frac{\text{Output}'}{\text{Output}} = A(1+B)(\sin 4\theta)/2 = \frac{\sqrt{2A}}{2}(1+B)\cos 2\theta. \tag{4.7}$$

In most cases, for a significant signal enhancement, we need A to be large. Therefore, we have $\cos 2\theta \to 1$ and $B \to 0$, which leads to a final expression of the signal enhancement of

$$\frac{\text{Output}'}{\text{Output}} \to \frac{\sqrt{2A}}{2}. \tag{4.8}$$

Since the system noise stays the same as in the balanced system, the S/N ratio improvement is also $\frac{\sqrt{2A}}{2}$, which is significant. I would like to point out that this enhancement factor from the unbalanced method is still smaller than $\sqrt{A}$, which is the enhancement from directly increasing the optical power in the balanced system. Thus, for the best S/N ratio performance, we should always first increase the power until the detector is nearly saturated, then implement the "unbalanced" technique.

4.3 Experimental Demonstration

To demonstrate the proposed S/N ratio enhancement, I conduct a power-dependent study on a Py(5nm)/Pt(6nm) sample using the unbalanced optical bridge technique. For this experiment, a Ti:Sapphire mode-locked laser with a center wavelength of 780 nm is used. The laser light is focused onto the 50 μm $\times$ 50 μm patterned sample. A 20 mA electrical current is applied to drive the spin-orbit torques (SOTs). The SOT-induced magnetization reorientation leads to the polarization change of the reflected light, which can be detected by the optical bridge system. First of all, as shown in Fig. 4.5(a), the system noise is independent of the power amplification. This result agrees well with the noise analysis conclusion that electron shot noise in the detector is the main noise source. Thus, when

the light power at the detector stays constant, the noise is also unchanged. This noise is equivalent to a polarization rotation of ~ 80 nrad$/\sqrt{\text{Hz}}$. This noise level can still be improved by averaging. The real sensitivity of the system is ultimately limited by the thermal noise from the detectors and lock-in amplifier, which cannot be reduced through sample averaging.

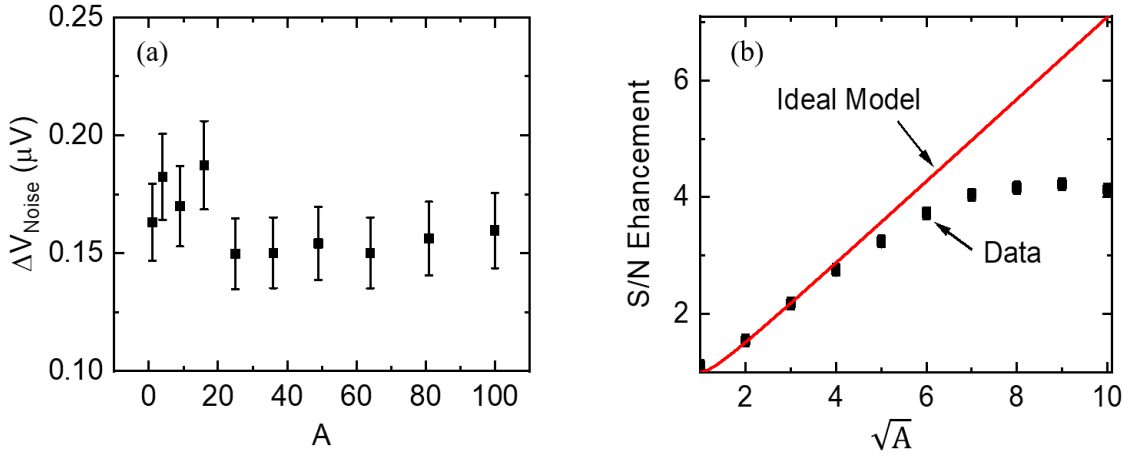

Figure 4.5: Results of the power-dependent study for the unbalanced optical bridge technique. (a) System noise as function of optical power amplification A. (b) Signal enhancement as a function of square root of the power amplification. The "Ideal Model" fitting line is set to have a slope of $\frac{\sqrt{2}}{2}$ and zero intercept.

On the other hand, the signal enhancement behavior is slightly different from what I expected. As shown in Fig. 4.5(b), albeit the first few points match the proposed $\frac{\sqrt{2A}}{2}$ fitting line, the experimental data starts to deviate from the ideal model after $A = 16$. The reason for this discrepancy turns out to be the imperfect linear polarization state. Recall at the first stage in Fig. 4.4, I assumed a perfectly linear polarization as the initial polarization state. However, after a simple characterization, I find that the extinction ratio of the polarization is only $400:1$ due to the birefringence of the optics. That is equivalent to a $20:1$ ratio of the s- and p-electric field components. Therefore, for a more realistic simulation, the initial polarization state needs to be changed as shown in Fig. 4.6. Then, the final polarization state before the detector can be numerically simulated with:

$$P_{\text{Final}} = \text{HWP} \times \text{Sample} \times \begin{bmatrix} bi \\ a \end{bmatrix}, \tag{4.9}$$

where

$$\text{Sample} = \begin{bmatrix} \cos\Delta\theta_k & \sin\Delta\theta_k \\ -\sin\Delta\theta_k & \cos\Delta\theta_k \end{bmatrix}$$

and

$$\text{HWP} = \begin{bmatrix} \cos 2\theta_k & \sin 2\theta_k \\ -\sin 2\theta_k & \cos 2\theta_k \end{bmatrix}$$

are the Jones matrices for the sample and a half-wave-plate with fast axis at θ degrees, respectively.

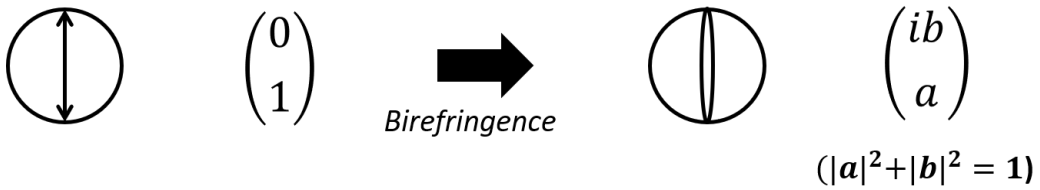

Figure 4.6: Modified initial polarization state due to the birefringence of optics. Here, $a : b = 20 : 1$.

The modified simulation of the signal enhancement as a function of power amplification can then be calculated as

$$\text{Signal Enhancement} = \frac{\text{Signal}(A)}{\text{Signal}(A=1)} = \frac{|P^s_{\text{Final}}|^2 - |P^p_{\text{Final}}|^2}{\text{Signal}(A=1)},$$

where $\text{Signal}(A = 1)$ represents the signal of the balanced system, P^s_{Final} and P^p_{Final} are the s- and p-components of the final polarization, respectively. As shown in Fig. 4.7, the modified model fits the experimental result much better. More than 3 times S/N ratio improvement is achieved by implementing the unbalanced optical bridge method.

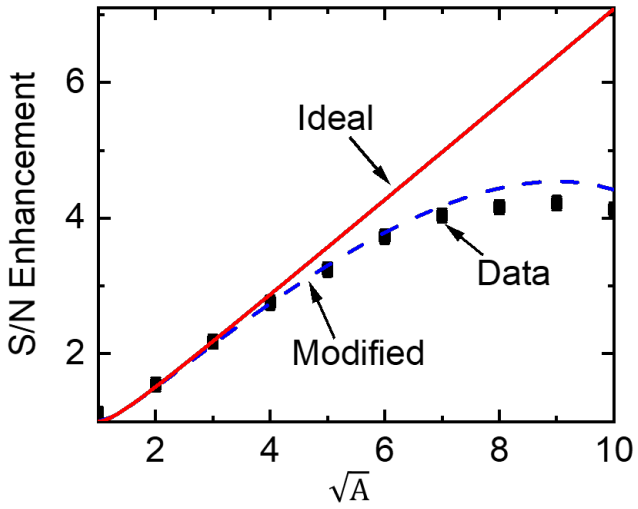

Figure 4.7: Modified simulation curve (blue dashed line) for signal enhancement as a function of square root of the power amplification.

4.4 Using the Unbalanced Method to Measure a Pattern-Free Sample

To further confirm the accuracy as well as the ultrahigh sensitivity of this method, we carry out the SOT measurement on an non-lithographically-processed (unpatterned) sample. The unpatterned sample has the same structure as the patterned one used in the previous power-dependent study. As shown in Fig. 4.8(a), the sample is cut into a rectangular piece with a width of 2 mm. Two copper wires are attached to the surface of the film by indium. An electric current of 100 mA is applied to provide a current density that is only $\frac{1}{8}$ of the one in the patterned sample. Thanks to the much larger sample area, no objective/lens is used, which drastically increases the optical power can be used before thermal effects becomes significant. A comparison between the MOKE signal before and after implementing the unbalanced optical bridge technique is shown in Fig. 4.8(b). An incident power of 4.4 mW is applied for the balanced optical bridge measurement. For the unbalanced measurement, 70.4 mW is used, which is 16 times the balanced setting. The laser beam without focusing

has a diameter of 2.5 mm. Compared to the 4 μm spot size after a 10× objective, the energy per unit area due to the 70.4 mW laser beam is equivalent to less than 1 μW in the focused situation. Thus, laser-induced sample heating is not an issue.

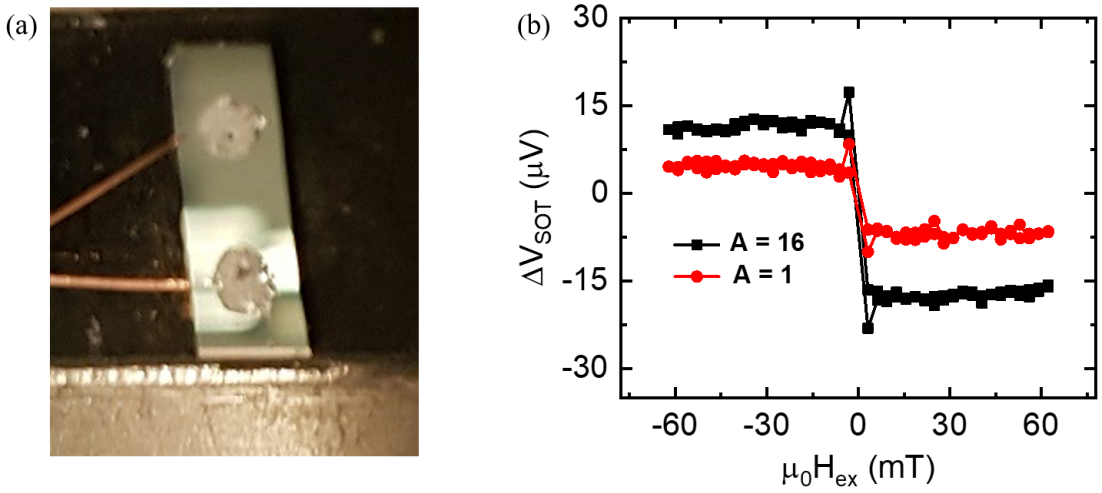

Figure 4.8: (a) Photo of the unpatterned sample with two wires attached to it. (b) SOT-induced MOKE signal of the unpatterned sample for the balanced optical bridge setting (red) and the unbalanced setting (black) with 16 times power amplification.

As a result, thanks to the ultrahigh sensitivity of our system, the MOKE signal is quite large even in the balanced optical bridge setting. The signal of the unbalanced measurement is about 3 times larger than the balanced result, which agrees well with the simulation. I then compare the extracted signal for the unpatterned and patterned sample. Under a current density of 1×10^6 A/m^2, the unpatterned sample has a signal of 0.34 ± 0.03 μrad, which is reasonably consistent with the patterned result of 0.32 ± 0.01 μrad. The error in the unpatterned result is mainly from the imperfect estimate of the sample width.

4.5 Conclusion

In conclusion, I demonstrate the main noise source of our MOKE-based SOT magnetometry system is the electron shot noise in the balanced detector. Based on that finding, I propose

an unbalanced optical bridge method to enhance the signal-to-noise ratio and experimentally achieve a S/N improvement of a factor of 3. Better performance is theoretically possible if the light polarization quality is improved. And, reliable SOT measurements are carried out on an unpatterned sample, which dramatically simplifies the sample preparation process and makes high speed and precise SOT characterization possible.

Chapter 5

Anomalous Spin-Orbit Torques in Magnetic Single-Layer Films

Part of this chapter will be published in "Anomalous Spin-Orbit Torques in Magnetic Single-Layer Films," by Wenrui Wang*, Tao Wang*, Vivek P. Amin, Yang Wang, Anil Radhakrishnan, Angie Davidson, Shane R. Allen, T. J. Silva, Hendrik Ohldag, Davor Balzar, Barry L. Zink, Paul M. Haney, John Q. Xiao, David G. Cahill, Virginia O. Lorenz, and Xin Fan, submitted for Publication (*Contributed equally).

5.1 Introduction

As discussed in Chap. 1, spin-orbit interaction (SOI) couples charge and spin transport [27, 92, 93], enabling electrical control of magnetization, the foundation of next-generation spintronic devices [30, 67–69, 94]. SOI can convert a charge current into a flow of spin angular momentum (spin current) with spin polarization orthogonal to both the charge and spin currents [95]. One of its manifestations in a magnetic conductor is the anomalous Hall effect (AHE) [96, 97], illustrated in Fig. 5.1(a). Due to the imbalance of electrons with spins parallel and antiparallel to the magnetization, the flow of spin current results in charge accumulation on the top and bottom surfaces [98]. In this chapter, we apply similar considerations to propose the existance of what we call the anomalous spin-orbit torque (ASOT). The geometry of ASOT is illustrated in Fig. 5.1(b), in which an electric current is parallel to the magnetization. Based on symmetry, which will be discussed in the next section, SOI should give rise to a spin current flowing between the top and bottom surfaces

of the magnetic conductor with electron spin polarization transverse to the magnetization. The transverse spins will precess rapidly about the magnetization direction and exert torques on the magnetization as they dephase, in analogy with spin transfer torque [99]; this results in net ASOTs in the y-direction on the top and bottom surfaces, but no bulk spin torque due to symmetry. Under the assumption that ASOT results in a small perturbation to the magnetization, the ASOTs are equivalent to effective magnetic fields in the z-direction [81] that tilt the magnetization out of plane, as illustrated in Fig. 5.1(b). Like the AHE, ASOT is a fundamental property of all magnetic conductors (those with broken bulk inversion symmetry have been shown to exhibit a non-zero bulk spin-orbit torque [100, 101]).

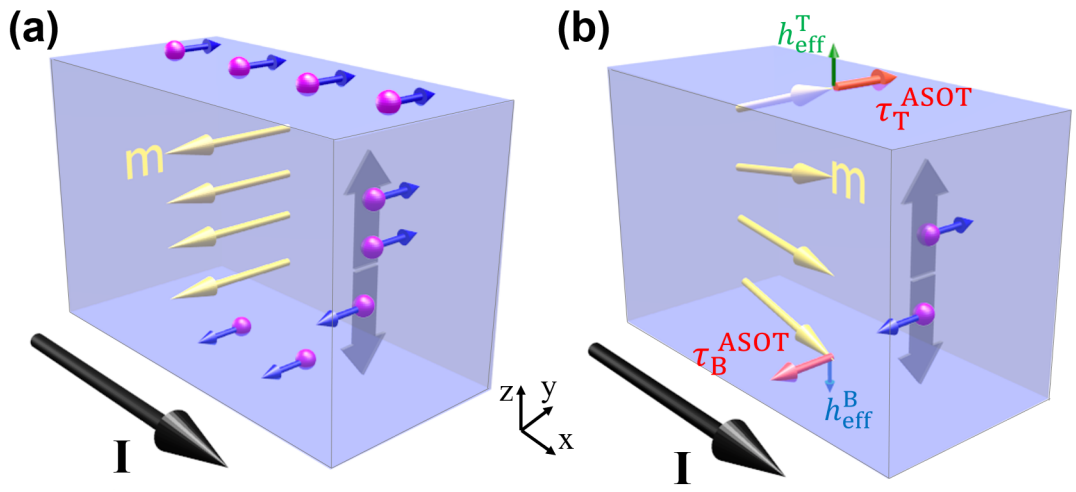

Figure 5.1: Illustrations of the anomalous Hall effect and anomalous spin-orbit torque. (a) In the anomalous Hall effect (AHE), a charge current **I** (black arrow) perpendicular to the magnetization **m** (yellow arrows) generates a flow of spin current (grey arrows) in the z-direction. Here blue arrows on purple spheres represent spin directions of electrons. Due to the imbalance of majority and minority electrons, the flow of spin current results in spin and charge accumulation on the top and bottom surfaces. (b) When a charge current is applied parallel with the magnetization, the AHE vanishes, but we predict and show that spin-orbit coupling generates anomalous spin-orbit torque (ASOT). The ASOTs (red arrows) are equivalent to out-of-plane fields (green arrows) that tilt the magnetization out of plane. $\tau_{\mathrm{T}}^{\mathrm{ASOT}}$ ($\tau_{\mathrm{B}}^{\mathrm{ASOT}}$) and $h_{\mathrm{eff}}^{\mathrm{T}}$ ($h_{\mathrm{eff}}^{\mathrm{B}}$) are the ASOTs and equivalent fields at the top (bottom) surfaces, respectively.

In this chapter, I first discuss the fundamental possibility of ASOT from a symmetry

perspective. In Section 5.3, an analytic derivation of the ASOT-induced magnetization tilt and its experimental demonstration on a single layer $Ni_{80}Fe_{20}$(Py) film are shown. In Section 5.4, I establish a numerical model to fit the experimental data as a function of the magnetic film thickness. Important parameters of the ASOT, such as the amplitude and direction, can be extracted from the fitting. In Section 5.5, measurements of a series of single-layer magnetic films with different interfaces are carried out to rule out interface contributions to the observed ASOT. Lastly, similar effects are also observed in other common ferromagnetic metals, including Co, Ni, and Fe and first principles calculations corroborate the order of magnitude of the measured values.

5.2 Symmetry Argument

Curie's principle [102] states that the symmetry of an effect must follow the symmetry of the cause. This heuristic argument provides guidance in searching for new physical phenomena. Here we show how symmetry leads to the types of surface spin and charge accumulation observed in the spin Hall effect, anomalous Hall effect and anomalous spin-orbit torque.

In polycrystalline, amorphous or crystalline thin films with high symmetry, the structure of the thin film is invariant under several symmetry operations, including (1) mirror symmetry operations: σ_{xy}, σ_{xz}, and σ_{yz}, where the subscript denotes the mirror plane, (2) two-fold rotational symmetry operations: C_2^x, C_2^y and C_2^z, where the superscript denotes the rotational axis, and (3) center inversion symmetry: i, where the inversion center is any point of the material.

When an electric current is applied through a nonmagnetic thin film along the x-direction, as shown in Fig. 5.2(a), mirror symmetry σ_{yz}, rotational symmetries C_2^y and C_2^z, and inversion symmetry i are broken. However, the system still retains the symmetries σ_{xy}, σ_{xz}, and C_2^x. Therefore, on the top and bottom surfaces in the xy plane, there cannot be any net charge accumulation, which would violate symmetries σ_{xy} and C_2^x. However, spin accumulation

with a certain spin polarization is allowed by symmetry. Spin polarizations in the x- and z-directions are forbidden, as both violate symmetry σ_{xz}. Spin polarization in the y-direction is allowed, given that the spins are polarized in opposite directions on the top and bottom surfaces to satisfy the symmetries σ_{xy} and C_2^x. These symmetry conditions characterize what is known as the spin Hall effect in nonmagnetic materials.

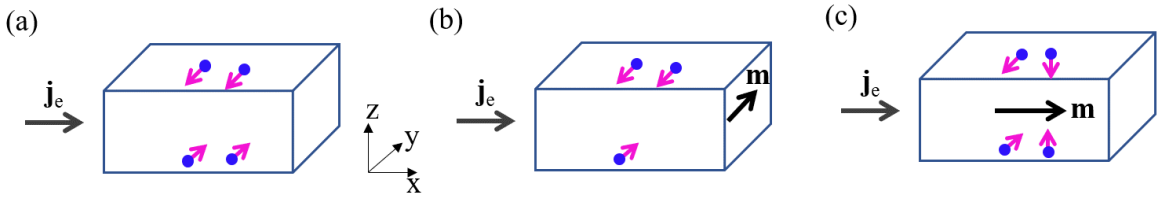

Figure 5.2: Symmetry-based analysis of the current-induced charge/spin accumulations at the top and bottom surfaces of (a) a nonmagnetic film, (b) a magnetic film with magnetization **m** along the y-direction and (c) a magnetic film with magnetization **m** along the x-direction.

In a magnetic film, where the existence of magnetization breaks more symmetries, more complicated surface phenomena are expected. As shown in Fig. 5.2(b), the magnetization along the y-direction breaks the mirror symmetry σ_{xy}, σ_{yz} and rotational symmetries C_2^x and C_2^z, leaving the magnetic film only carrying the mirror symmetry σ_{xz}. As a result, charge accumulation as well as spin accumulation with spins in the y-direction on the top and bottom surfaces are allowed by symmetry; these symmetry conditions characterize the anomalous Hall effect. On the other hand, in a magnetic film with magnetization along the x-direction, as shown in Fig. 5.2(c), the system only carries the C_2^x rotational symmetry and breaks all mirror symmetries. Under such symmetry, spin polarizations in both the y- and z- directions are allowed on the top and bottom surfaces. Due to spin dephasing, the spin accumulations give rise to spin torques in the y- and z- directions, which obey the same symmetry constraints. The symmetry conditions for the case of y-polarization characterizes damping-like anomalous spin-orbit torque, which is the focus of this work. The symmetry condition for z-polarization characterizes a field-like torque, the effect of which is very similar

to that of a current-induced Oersted field. It is challenging to distinguish the field-like torque and the Oersted field, the latter of which is likely to dominate the former. Therefore, the field-like torque is not studied in this paper.

It is worth pointing out that although spin polarization in the z-direction is allowed by symmetry, it would be independent of the current direction, as can be seen by applying the mirror symmetry operator σ_{yz}. This symmetry condition characterizes the situation in which the magnetic film is heated up by a current. When the film dissipates heat via the top and bottom surfaces, it induces spin accumulation with spin polarized along the **m** direction via the spin Seebeck effect. This second-order effect, however, is not relevant to what we aim to study here.

5.3 Simulation and Observation of ASOT-Induced Magnetization Distribution

5.3.1 Analytic Derivation of the ASOT-Induced Magnetization Distribution In a Single-Layer Magnetic Film

A phenomenological model of the ASOT is shown in Fig. 5.3. In a magnetic material with bulk inversion symmetry, the SOI gives rise to a separation of spins. The spins are transverse to the magnetization and thus will be quickly absorbed. The absorption of transverse spins should yield no net spin torque in the bulk due to the bulk inversion symmetry. However, at the top and bottom surfaces, where inversion symmetry is broken, we expect non-zero and opposite damping-like ASOTs that tilts the magnetization out of plane.

Assuming the ASOT is a purely interfacial spin torque and neglecting surface anisotropy, it is convenient to discretize the FM into a multilayer system (shown in Fig. 5.4), with the layers labeled 1 through n, where each layer has its own magnetization. The influence of ASOT can be written as an effective field h_z^i for the ith layer. Within such a system, the

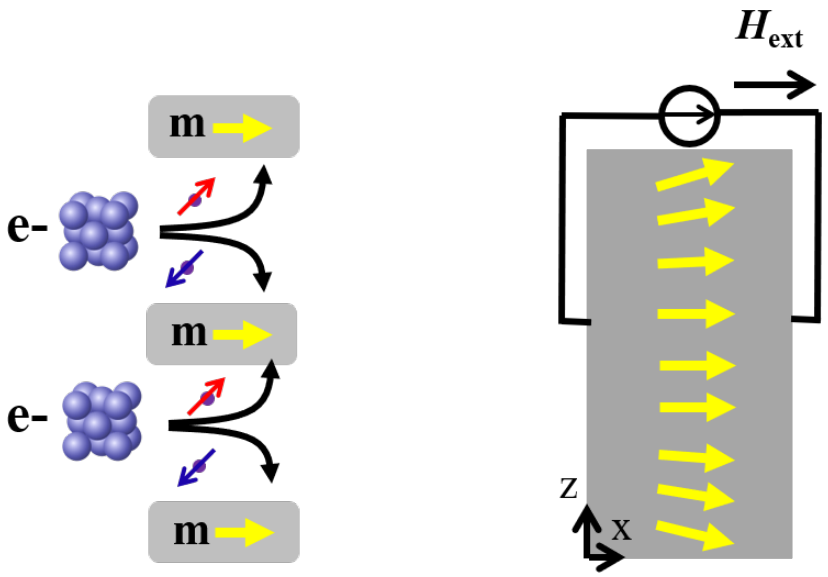

Figure 5.3: Phenomenological model of the ASOT. The spin-orbit interaction from the lattice separates electrons with opposite spins. The spin angular momentum is quickly absorbed by the magnetization. Due to bulk inversion symmetry, the only net angular momentum absorption occurs at the surface, leading to ASOT.

ASOTs only affect the two surface layers:

$$h_z^1 = \frac{\tau_{\mathrm{T}}^{\mathrm{ASOT}}}{\mu_0 M_s a} = -h_z^n = -\frac{\tau_{\mathrm{B}}^{\mathrm{ASOT}}}{\mu_0 M_s a}, \tag{5.1}$$

and

$$h_z^2 = h_z^3 = ... = h_z^{n-1} = 0, \tag{5.2}$$

where $\tau_{\mathrm{T}}^{\mathrm{ASOT}}$ ($\tau_{\mathrm{B}}^{\mathrm{ASOT}}$) is the ASOT at the top (bottom) surface, a is the lattice constant, and M_s is the saturation magnetization.

In addition to ASOT, interlayer exchange coupling significantly affects the behavior of the local magnetization. The interlayer exchange energy per unit area is described as [103]

$$E = -J\mathbf{m}_i \cdot \mathbf{m}_{i+1}, \tag{5.3}$$

where $\mathbf{m}_i$ and $\mathbf{m}_{(i+1)}$ are the unit magnetization vectors of nearest neighbor FM layers i

and $i+1$, and J is the interface exchange strength. For a uniform magnetic layer, J can be calculated as $J = \frac{2A_{\text{ex}}}{a}$, where A_{ex} is the exchange stiffness. Therefore, for magnetic layer i, the exchange coupling results in an effective field:

$$\mathbf{H}_i = H_z^i \mathbf{z} + H_y^i \mathbf{y} = \frac{J(m_z^{i-1} + m_z^{i+1})}{\mu_0 M_s a}\mathbf{z} + \frac{2J}{\mu_0 M_s a}\mathbf{y}, \tag{5.4}$$

where m_z^i is the z-component of $\mathbf{m}_i$.

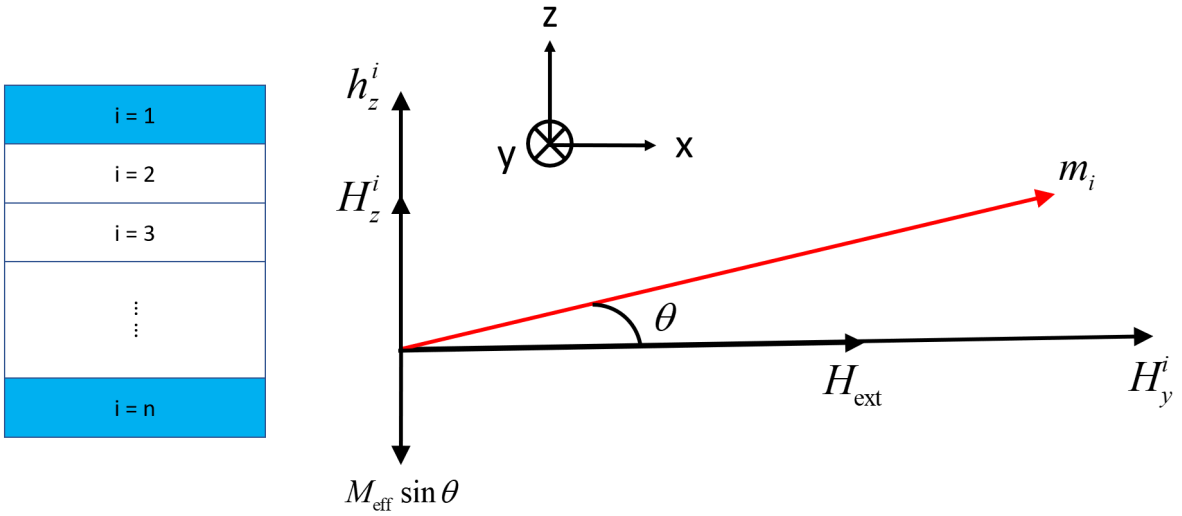

Figure 5.4: Illustration of the discrete-layer model (left) and effective magnetic fields (right) applied on the layer i. The ASOT is assumed to only exist in the top and bottom layers (blue layers). h_z^i is the effective field due to ASOT, H_z^i and H_y^i are the effective fields from nearest-neighbor exchange coupling, H_{ext} is the external magnetic field, and $M_{\text{eff}} = (M_s - 2K_a/(\mu_0 M_s))$ is the effective field caused by demagnetization, where $K_a = 0$ for $i = 2, 3, ...n-1$, is the surface anisotropy energy density.

All the magnetic fields on magnetic atomic layer i are depicted in Fig. 5.4. From the diagram, we can write

$$\frac{h_z^i + H_z^i - M_{\text{eff}} \sin\theta}{H_{\text{ext}} + H_y^i} = \sin\theta. \tag{5.5}$$

For the bulk layers, since $h_z^i = 0$ and $\sin\theta = m_z^i$, by plugging Eq. 5.4 into Eq. 5.5, we

have

$$m_z^i = \frac{\frac{J}{\mu_0 M_s a}(m_z^{i-1} + m_z^{i+1}) - M_{\text{eff}} m_z^i}{H_{\text{ext}} + \frac{2J}{\mu_0 M_s a}}. \tag{5.6}$$

Knowing a is small and

$$f''(x) = \lim_{h \to 0} \frac{f(x+h) - 2f(x) + f(x-h)}{h^2}.$$

Eq. 5.6 can be rewritten as

$$\frac{Ja}{\mu_0 M_s}(m_z^i)'' = (H_{\text{ext}} + M_{\text{eff}}) m_z^i. \tag{5.7}$$

The solution of Eq. 5.7 should have the form of

$$m_z^i = Ae^{-z/\lambda} + Be^{+z/\lambda}, \tag{5.8}$$

where $\lambda = \sqrt{\frac{Ja}{\mu_0 M_s (H_{\text{ext}} + M_{\text{eff}})}}$ is the exchange length.

On the other hand, for the top layer, we can rewrite Eq. 5.5 as

$$m_z^1 = \frac{\frac{\tau_{\text{T}}^{\text{ASOT}}}{\mu_0 M_s a} + \frac{J}{\mu_0 M_s a} m_z^2 - M_{\text{eff}} m_z^1}{H_{\text{ext}} + \frac{J}{\mu_0 M_s a}}. \tag{5.9}$$

Eq. 5.9 can again be rewritten to

$$(H_{\text{ext}} + M_{\text{eff}}) m_z^1 + \frac{J}{\mu_0 M_s a}(m_z^1 - m_z^2) = \frac{\tau_{\text{T}}^{\text{ASOT}}}{\mu_0 M_s a}. \tag{5.10}$$

Since a is small, the first term in Eq. 5.10 is negligible. Therefore, the equation can be simplified into

$$(m_z^1)' = -\frac{\tau_{\text{T}}^{\text{ASOT}}}{Ja}. \tag{5.11}$$

Similarly, the bottom layer magnetization yields

$$(m_z^n)' = -\frac{\tau_{\mathrm{B}}^{\mathrm{ASOT}}}{Ja}. \tag{5.12}$$

Using Eq. 5.11 and 5.12 as boundary conditions to solve Eq. 5.8, we get

$$A = \frac{\lambda}{Ja}\frac{\tau_{\mathrm{T}}^{\mathrm{ASOT}} - \tau_{\mathrm{B}}^{\mathrm{ASOT}} e^{-d/\lambda}}{1 - e^{-2d/\lambda}}, \tag{5.13}$$

and

$$B = \frac{\lambda}{Ja}\frac{\tau_{\mathrm{T}}^{\mathrm{ASOT}} - \tau_{\mathrm{B}}^{\mathrm{ASOT}} e^{d/\lambda}}{e^{2d/\lambda} - 1}, \tag{5.14}$$

where d is the thickness of the magnetic film.

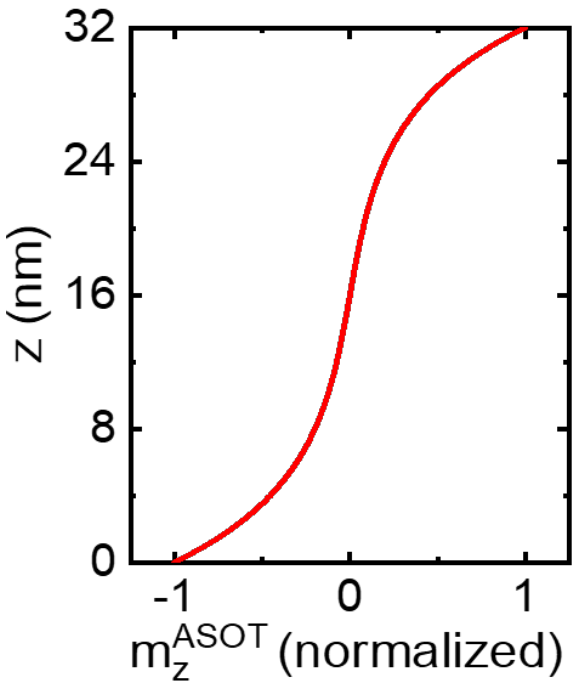

Figure 5.5: Simulated distribution of the out-of-plane magnetization $m_z^{\mathrm{ASOT}}(z)$ in a 32 nm Py film driven by equal and opposite ASOTs on the surfaces, scaled by the maximum value.

Plugging A and B back into Eq. 5.8, we get an analytic solution of the ASOT-induced magnetization tilt as

$$m_z^{\mathrm{ASOT}}(z) = \frac{\tau_{\mathrm{T}}^{\mathrm{ASOT}} \cosh\frac{d-z}{\lambda} + \tau_{\mathrm{B}}^{\mathrm{ASOT}} \cosh\frac{z}{\lambda}}{\lambda \sinh\frac{d}{\lambda}(|H_{\mathrm{ext}}| + M_{\mathrm{eff}})\mu_0 M_s} m_x. \tag{5.15}$$

Because of the strong exchange interaction, the effects from the two ASOTs will cancel out if the magnetic film is thin. However, when the magnetic film is much thicker than the exchange length, the magnetizations at the two surfaces will tilt out of plane in response to the respective ASOTs. A simulation curve based on Eq. 5.15 is shown in Fig. 5.5.

A more general model involving the surface anisotropy field acting on the two surface layers can be numerically calculated. By inserting Eqs. 5.1, 5.2 and 5.4 into 5.5, we get

$$\frac{\tau_{\mathrm{ASOT}}^i}{\mu_0 M_s a} = (H_{\mathrm{ext}} + M_{\mathrm{eff}} + \frac{2J}{\mu_0 M_s a}) m_z^i - \frac{J}{\mu_0 M_s a} m_z^{i-1} - \frac{J}{\mu_0 M_s a} m_z^{i+1}. \tag{5.16}$$

The ASOT-induced magnetization tilt can then be calculated by solving the following equation:

$$\begin{bmatrix} J+C' & -J & 0 & \dots & 0 \\ -J & 2J+C & -J & \dots & 0 \\ 0 & -J & 2J+C & \dots & 0 \\ \vdots & \vdots & \vdots & \ddots & \vdots \\ 0 & 0 & 0 & \dots & J+C' \end{bmatrix} \begin{bmatrix} m_z^1 \\ \vdots \\ m_z^i \\ \vdots \\ m_z^n \end{bmatrix} = \begin{bmatrix} \tau_{\mathrm{T}}^{\mathrm{ASOT}} \\ \vdots \\ 0 \\ \vdots \\ \tau_{\mathrm{B}}^{\mathrm{ASOT}} \end{bmatrix}, \tag{5.17}$$

where the surface term $C' = \mu_0 M_s a(H_{\mathrm{ext}} + M_{\mathrm{eff}})$ takes into account the surface anisotropy, and $C = \mu_0 M_s a(H_{\mathrm{ext}} + M_s)$ is for the bulk layers. As shown in Fig. 5.6(a), the numerical result maintains the signature of the analytic result with only a small amplitude difference.

We also verify the sensitivity of the magnetization tilt distribution to the number of layers exhibiting ASOTs. As shown in Fig. 5.6(b), spreading the ASOT into 5 surface layers does not affect the simulation result significantly. Therefore, our assumption that the ASOTs only exist at the top and bottom layers is reasonable.

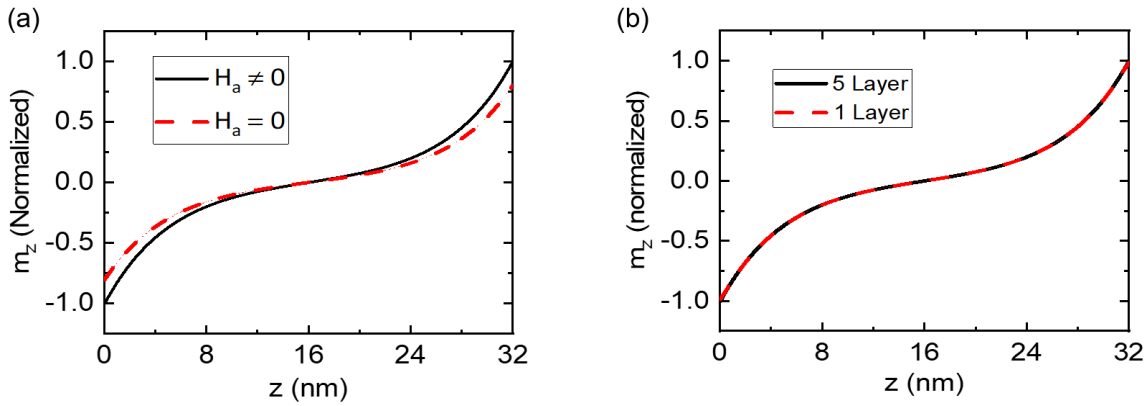

Figure 5.6: (a) Simulated distribution of the out-of-plane magnetization tilt $m_z^{\mathrm{ASOT}}(z)$ in a 32 nm Py film based on the numerical calculation (black solid line) and the analytic expression (red dashed line). (b) Simulation results driven by equal and opposite ASOTs on the first (red dash line) and first five (black solid line) surface layers, scaled by the maximum value.

5.3.2 Experimental Observation of the ASOT-Induced Magnetization Distribution

To observe the predicted ASOT-induced out-of-plane magnetization tilt, we fabricate a sample with structure: substrate/$\mathrm{AlO_x}$(2)/Py(32)/$\mathrm{AlO_x}$(2)/$\mathrm{SiO_2}$(3), where the numbers in parentheses are thicknesses in nanometers; the substrate is fused silica, which allows optical access to the bottom of the sample. Py is chosen because it is magnetically soft and widely used for the study of spin-orbit torques. The film is lithographically patterned into a 50 μm $\times$ 50 μm square and connected by gold contact pads, as shown in Fig. 5.7(a). When an electric current I of 40 mA is applied directly through the sample, ASOTs at the top ($\tau_{\mathrm{T}}^{\mathrm{ASOT}}$) and bottom ($\tau_{\mathrm{B}}^{\mathrm{ASOT}}$) surfaces lead to non-uniform magnetization tilting, as described by Eq. 5.15. When a calibration current I_{Cal} of 400 mA is passed around the sample, an out-of-plane Oersted field $\mu_0 h_{\mathrm{Cal}} \sim 0.85$ mT is generated that uniformly tilts the magnetization out of plane, which is used for calibrating the magnitude of the ASOTs:

$$m_z^{\mathrm{Cal}}(z) = \frac{h_{\mathrm{Cal}}}{|H_{\mathrm{ext}}| + M_{\mathrm{eff}}}. \tag{5.18}$$

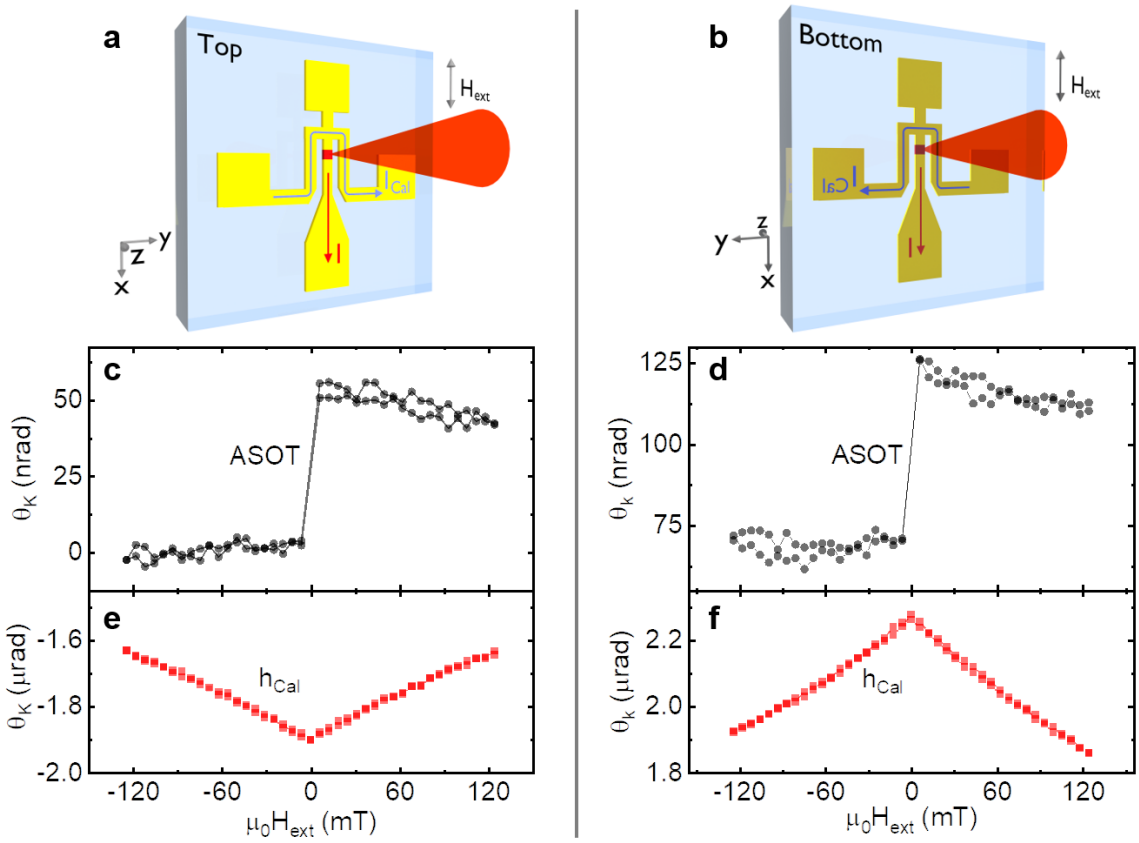

Figure 5.7: Diagrams of the measurement configurations with the laser incident on (a), the top and (b), the bottom of the sample. The plots below each diagram correspond to signals measured in that diagram's configuration. (c, d), The measured Kerr rotation signals for when current is applied through the sample, which arise from ASOTs. (e, f), The measured Kerr rotation signals for when the calibration field h_{Cal} is applied.

Considering the ASOT-induced magnetization tilt yields no net magnetization change, common electrical methods are not able to detect it. The penetration depth of a laser at 780 nm in Py is approximately 14 nm, which is less than half the thickness of the 32 nm Py. Therefore, the MOKE response is more sensitive to the ASOT-induced out-of-plane magnetization $m_z^{\mathrm{ASOT}}(z)$ on the surface on which the laser is directly incident. Therefore, we use the polar MOKE technique discussed in Chapter 3 to detect the magnetization changes. Both the Kerr rotation θ_k and ellipticity change ϵ_k of the polarization of a linearly polarized laser reflected from the sample are measured [104, 105].

The Kerr rotation due to ASOT as a function of the external field (shown in Figs. 5.7(c) and (d)) resembles a magnetization hysteresis, as can be understood from Eq. 5.15. The overall offsets of the Kerr rotation signals are due to the out-of-plane current-induced Oersted field, which does not depend on the in-plane magnetization orientation [81]. In contrast, when a uniform calibration field h_{Cal} is applied, the Kerr rotation is symmetric as a function of external field H_{ext} (see Fig. 5.7(e) and (f)), consistent with Eq. 5.18. The Kerr rotation due to ASOT on the top (Fig. 5.7(c)) and bottom (Fig. 5.7(d)) surfaces are the same sign, in agreement with our phenomenological model (Fig. 5.3), which predicts the bottom ASOT has similar magnitude but opposite sign as the top ASOT. In contrast, the Kerr rotation due to the calibration field (Figs. 5.7(e) and (f)) changes sign because h_{Cal} is reversed upon flipping the sample.

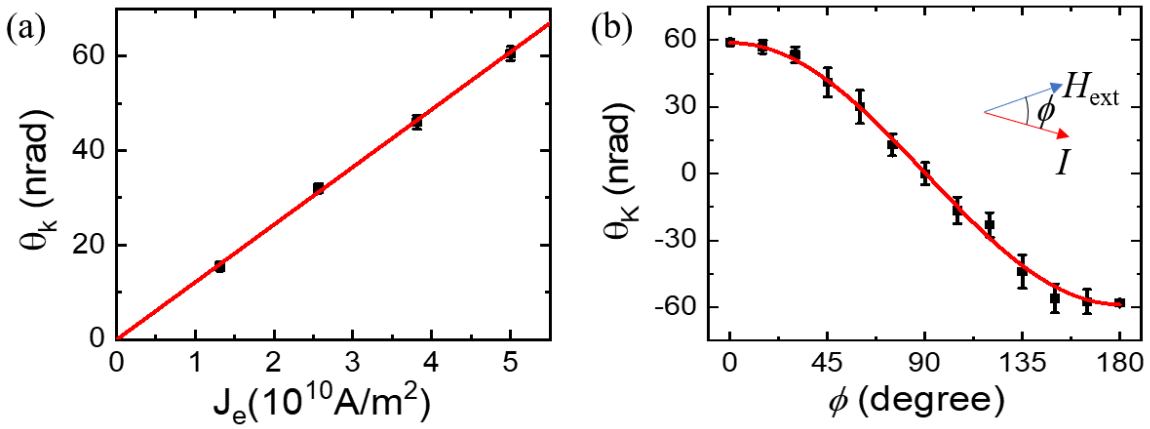

Figure 5.8: MOKE signal as a function of (a) current density and (b) the angle between the current direction and the magnetization direction. Both studies are performed with the same sample: Si(sub)/SiO_2(1000)/AlO_x(2)/Py(32)/AlO_x(2)/SiO_2(3), where the numbers in parentheses are the thicknesses in nanometers. The current density in the angle dependence study is 5×10^{10} A/m^2.

To further confirm the observed MOKE signal is indeed due to the current-induced ASOTs, we measure the ASOT-induced MOKE signal as a function of current density from the top surface of a 32 nm Py film on a silicon substrate. As shown in Fig. 5.8(a), up to

a current density of 5×10^{10} A/m^2, the detected signal increases linearly with the current density. This result rules out contributions from current-induced thermal effects, which should follow a quadratic dependence on the current. We also measure the MOKE signal as a function of the angle between the current and the magnetization. As demonstrated in Fig. 5.8(b), the sinusoidal dependence of the MOKE signal on the angle is consistent with Eq. 5.15. Both results suggest the observed MOKE signal is indeed a current-induced linear effect.

5.4 Thickness-Dependent Study: Model and Results

5.4.1 Model

To quantitatively determine the strength of the ASOT, we construct a numerical model based on the propagation matrix method [43, 104] to fit the measured MOKE results as a function of magnetic film thickness. In the structural model of Section 5.3, a single FM layer is treated as a series of ultrathin magnetic layers with different magnetization orientations. For magnetic layers with thicknesses less than the coherence length of the incident laser, multiple reflections should be taken into account. Here, we use medium boundary matrices and medium propagation matrices to treat the multiple reflections. Based on Ref. [43], in the polar MOKE geometry, medium boundary matrix A_j for the jth layer can be expressed as:

$$A_j = \begin{bmatrix} 1 & 0 & 1 & 0 \\ 0 & 1 & 0 & -1 \\ -\frac{in_jQ_jm_z^j}{2} & -n_j & \frac{in_jQ_jm_z^j}{2} & -n_j \\ n_j & \frac{in_jQ_jm_z^j}{2} & -n_j & \frac{in_jQ_jm_z^j}{2} \end{bmatrix}, \tag{5.19}$$

where n_j is the complex refractive index of the jth layer, Q_j is the Voigt coefficient of the

jth layer, and m_z^j is the out-of-plane magnetization magnitude of the jth layer, which is solved for in Sec. 5.3.

The propagation matrix D_j can be written as:

$$D_j = \begin{bmatrix} U\cos\delta^i & U\sin\delta^i & 0 & 0 \\ -U\sin\delta^i & U\cos\delta^i & 0 & 0 \\ 0 & 0 & U^{-1}\cos\delta^r & U^{-1}\sin\delta^r \\ 0 & 0 & -U^{-1}\sin\delta^r & U^{-1}\cos\delta^r \end{bmatrix}, \tag{5.20}$$

where

$$U = exp(-i\frac{2\pi}{\lambda}n_j d_j),$$

$$\delta_i = -\frac{\pi n_j Q d_j}{\lambda} m_z^j,$$

and

$$\delta_r = -\frac{\pi n_j Q d_j}{\lambda} m_z^j,$$

where d_j is the thickness of the jth layer and λ is the wavelength of the probe light.

To obtain the magneto-optical Fresnel reflection matrix $\begin{bmatrix} r_{ss} & r_{sp} \\ r_{ps} & r_{pp} \end{bmatrix}$, one computes the matrix M defined by

$$M = A_0^{-1} A_1 D_1 A_1^{-1} A_2 \ldots. \tag{5.21}$$

Then the 4×4 matrix M can be written in the form of a 2×2 block matrix as follows:

$$M = \begin{bmatrix} G & H \\ I & J \end{bmatrix}, \tag{5.22}$$

and the magneto-optical Fresnel reflection coefficients are further solved from

$$\begin{bmatrix} r_{ss} & r_{sp} \\ r_{ps} & r_{pp} \end{bmatrix} = IG^{-1}. \tag{5.23}$$

The complex Kerr angles for s- and p-polarized incident light are:

$$\begin{aligned} \Theta_k^p &= \frac{r_{sp}}{r_{pp}} \\ &\text{and} \\ \Theta_k^s &= \frac{r_{ps}}{r_{ss}}, \end{aligned} \tag{5.24}$$

respectively. Here the real part of the Kerr angle is defined as the Kerr rotation, and the imaginary part of the Kerr angle is the Kerr ellipticity. Since Kerr angle is independent of the incident polarization in polar MOKE, we use the s-polarization result in our simulation. Following the model described above, the MOKE response for different materials and structures can be simulated.

5.4.2 Experimental Results

To confirm the validity of our model and quantitatively determine the ASOT, we grow a series of $AlO_x(2)/Py(t)/AlO_x(2)/SiO_2(3)$ films on silicon substrates with 1 μm thermal oxide, where t varies from 4 nm to 48 nm. Unlike the current-induced Oersted field that depends on current amplitude, ASOT should depend on the current density. Therefore, for all samples, we apply the same current density of 5×10^{10} A/m^2, and measure the ASOT-induced MOKE signal change.

As presented in Fig. 5.9(a), the validity of the method is first verified by a thickness-dependent calibration measurement, where a uniform 0.85 mT out-of-plane calibration field is applied to all samples. The uniform out-of-plane calibration field causes a uniform magnetization tilt across the whole magnetic layer. Therefore it is reasonable to treat the entire

magnetic film as one layer in the simulation procedure described in the previous section. A structure of Air(∞)/Py(t)/SiO_2(1000)/Si(∞) is used for the simulation, where the numbers in parentheses are in nanometers. The thin SiO_2 and AlO_x layers are ignored because of their low absorption coefficients at 780 nm. A few nanometers of dielectric material do not affect the MOKE response significantly. With the refractive indices measured via ellipsometry, the resulting simulation curve is in good agreement with the experimental data.

To extract the ASOT amplitude, the top-surface Kerr rotation and the ellipticity change due to the ASOT is fitted in Fig. 5.9(b). The same model structure and fitting parameters are used as for the calibration smulation, except for including the ASOT strength $\tau_{\mathrm{T}}^{\mathrm{ASOT}} = -\tau_{\mathrm{B}}^{\mathrm{ASOT}}$ and the resulting non-uniform magnetization distribution. Here, we assume the surface torques are the same for all Py thicknesses under the same current density. By setting the value of $\tau_{\mathrm{T}}^{\mathrm{ASOT}}$ as the only free parameter in our model, we are able to fit the measured MOKE signals. The good agreement between experiment and simulation supports the assumption that ASOT depends on current density. The ASOTs are extrapolated to be $\tau_{\mathrm{T}}^{\mathrm{ASOT}} = -\tau_{\mathrm{B}}^{\mathrm{ASOT}} = -(0.86 \pm 0.04) \times 10^{-6}$ J/m^2 from the fitting. The extracted $\tau_{\mathrm{T}}^{\mathrm{ASOT}}$ is then used to calculate the spin-torque efficiency. Relating this torque to a spin current allows us to find the Spin-Hall-angle-like efficiency of the ASOT $\xi = \frac{2e\tau_{\mathrm{B}}^{\mathrm{ASOT}}}{j_e \hbar} = 0.053 \pm 0.003$, where e is the electron charge, j_e is the electric current density and $\hbar$ is the reduced Planck constant; this efficiency is comparable with the effective spin Hall angle of Pt (0.056 ± 0.005) measured in a Pt/Py bilayer [106]. The corresponding ASOT conductivity for 32 nm Py is calculated as $\sigma^{\mathrm{ASOT}} = \frac{2e}{\hbar}\frac{\tau_{\mathrm{B}}^{\mathrm{ASOT}}}{E} = 2300 \pm 115\ \Omega^{-1}\mathrm{cm}^{-1}$, where E is the applied electric field.

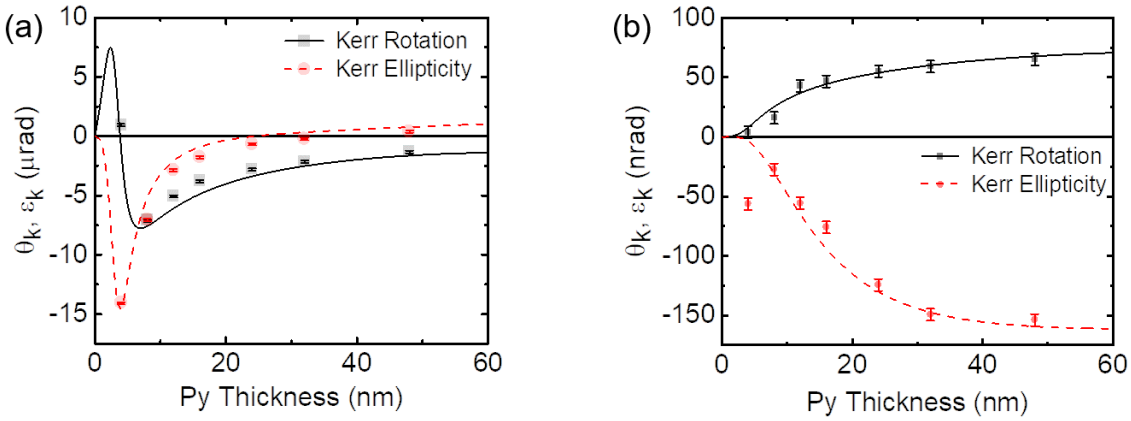

Figure 5.9: **Extracting the ASOT**. Kerr rotation (experimental, black squares; fit, black solid line) and ellipticity change (experimental, red circles; fit, red dashed line) (a), due to the calibration field, and (b), due to ASOT.

In Fig. 5.9(b), the deviation of the ASOT-induced change in Kerr ellipticity from the model for the 4 nm Py sample can be accounted for if a 1% variation between $\tau_{\mathrm{T}}^{\mathrm{ASOT}}$ and $\tau_{\mathrm{B}}^{\mathrm{ASOT}}$ is assumed, which may be due to a slight difference in spin relaxation at the two interfaces. In Fig. 5.10(a), we show a modified fitting curve that assumes a 1% difference between the top and bottom torques. The modified model only changes the fitting curves at small thicknesses (< 8 nm), and the modified Kerr ellipticity curve now fits well with the data point at 4 nm. The modified simulation curve can also be treated as a combination of the signal for balanced ASOT, $\tau_{\mathrm{T}}^{\mathrm{ASOT}} = \tau_{\mathrm{B}}^{\mathrm{ASOT}}$ (shown in Fig. 5.10(b)), and the signal for a 1% net torque originating from the bottom of Py film, $\tau_{\mathrm{T}}^{*} = 0$, $\tau_{\mathrm{B}}^{*} = -0.01\tau_{\mathrm{T}}$ (shown in Fig. 5.10(c)). The simulation for balanced ASOT is identical to the one shown in Fig. 5.9(b). However, as shown in Fig. 5.10(c), even a tiny (1%) total SOT can cause a rather large MOKE signal at small thicknesses that is comparable to the MOKE signal due to a much larger surface ASOT at large thicknesses. The large variation of the simulated MOKE signals when the Py is thin are due to the interference of the laser as it is reflected from the various interfaces; this effect also appears at small sample thicknesses in the MOKE signal from the calibration field (Fig. 5.9(a)).

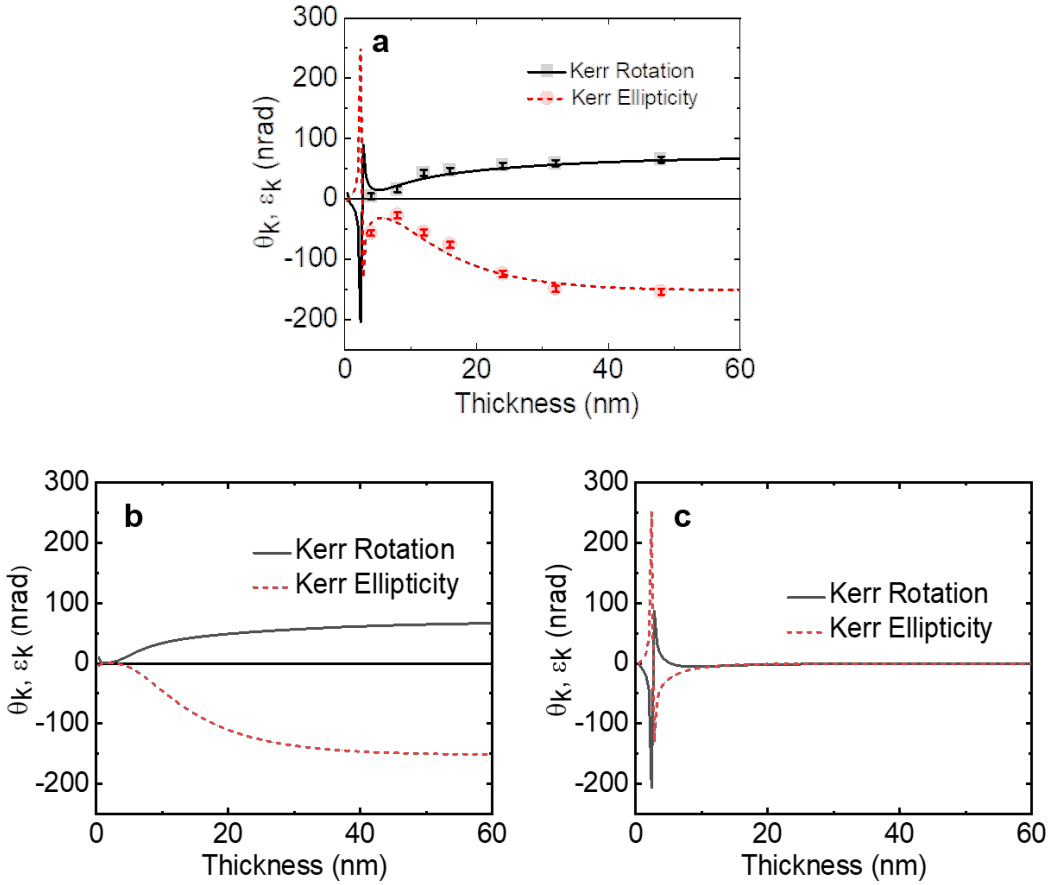

Figure 5.10: Experimental MOKE rotation and ellipticity signals (squares and circles) and simulated rotation and ellipticity signals (solid black lines and dashed red lines) for (a) unbalanced ($\tau_B = -1.01\tau_T$) ASOT, (b) balanced ($\tau_B = -\tau_T$) ASOT and (c) a tiny bottom (total) torque ($\tau_T^* = 0$, $\tau_B^* = -0.01\tau_T$) as a function of Py thickness. The fitting curves in (a) are equivalently combinations of the curves in (b) and (c), as described in this section.

5.4.3 Alternative Method to Determine τ_T^{ASOT} and τ_B^{ASOT}

The thickness-dependent numerical model introduced above is convenient to use in symmetric structures, such as AlO_x/Py(32)/AlO_x, where the assumption that top and bottom ASOT have very similar amplitudes is reasonable. However, for asymmetric structures, the ASOT at the top and bottom can be quite different. In this case, the thickness-dependent fitting method is less effective. Therefore, to compare the top and bottom ASOT strengths in such cases, it is important to be able to extract the surface torques individually.

As we have shown in Section 5.3, the overall ASOT-induced magnetization tilt distribu-

tion is a superposition of the magnetization distributions caused by the top surface torque and bottom surface torque. Similarly, the overall MOKE response can be treated as a combination of the top-surface ASOT-induced response and bottom-surface ASOT-induced response. Therefore, in the MOKE response calculation, by setting $\tau^{\mathrm{ASOT}}_{\mathrm{T(B)}} = 1$ and $\tau^{\mathrm{ASOT}}_{\mathrm{B(T)}} = 0$, we are able to simulate the MOKE responses due to only the top (bottom) ASOT with light incident from the front (F) and back (B) of the magnetic film. A detailed illustration is shown in Fig. 5.11.

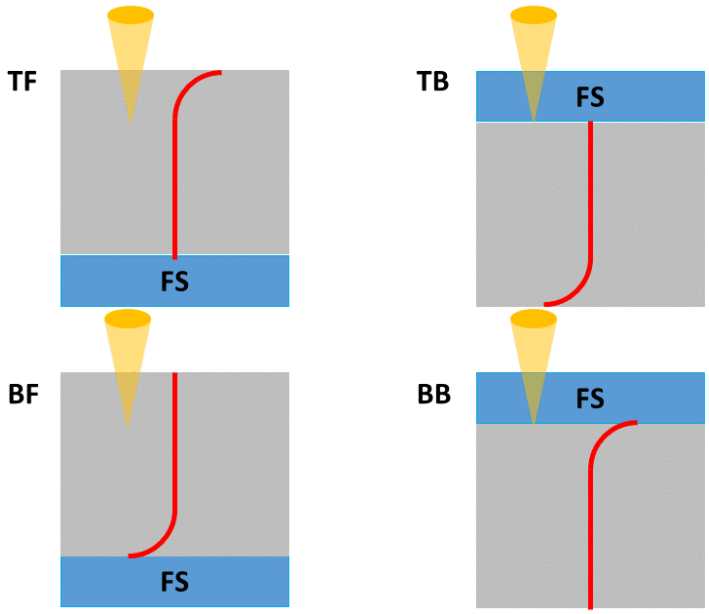

Figure 5.11: SSOT simulation configurations for extracting MOKE response due to top/bottom surface torques. Here, "TF" means top-surface torque, front incident light; "TB" means top-surface torque, back incident light; "BF" means bottom-surface torque, front incident light; "BB" means bottom-surface torque, back incident light.

By experimentally measuring the overall ASOT-induced MOKE response from the front and back of the magnetic film, we can correlate the experimental results with the calculated values:

$$\begin{bmatrix} \theta_{\mathrm{F}}^{\tau_{\mathrm{T}}} & \theta_{\mathrm{F}}^{\tau_{\mathrm{B}}} \\ \theta_{\mathrm{B}}^{\tau_{\mathrm{T}}} & \theta_{\mathrm{B}}^{\tau_{\mathrm{B}}} \end{bmatrix} \begin{bmatrix} \tau_{\mathrm{F}}^{\mathrm{ASOT}} \\ \tau_{\mathrm{B}}^{\mathrm{ASOT}} \end{bmatrix} = \begin{bmatrix} \theta_{\mathrm{F}} \\ \theta_{\mathrm{B}} \end{bmatrix}, \tag{5.25}$$

where the 2×2 matrix on the left side represents the calculated complex MOKE response for each configuration in Fig. 5.11, $\theta_{\mathrm{F(B)}}^{\mathrm{ASOT}}$ are the measured complex MOKE signals from front (back), and $\tau_{\mathrm{T(B)}}^{\mathrm{ASOT}}$ is the relative surface torque strength at top (bottom) surface.

Note that, there is finite reflection at the air/fused silica interface, which causes no polarization change, but also arrives at the detector. Thus, for the measurements from the back, we should take into account the attenuation of the MOKE signal caused by this part of the reflection light. According to the measured refractive indices, 3.1% of the laser power is reflected at the air/silica interface and 55.73% of the entire power is reflected at the silica/Py interface and goes back to the detector. Therefore, the measured MOKE response should be attenuated by a factor of 94.7%, and Eq. 5.25 should be rewritten as

$$\begin{bmatrix} \theta_{\mathrm{F}}^{\tau_{\mathrm{T}}} & \theta_{\mathrm{F}}^{\tau_{\mathrm{B}}} \\ \theta_{\mathrm{B}}^{\tau_{\mathrm{T}}} & \theta_{\mathrm{B}}^{\tau_{\mathrm{B}}} \end{bmatrix} \begin{bmatrix} \tau_{\mathrm{F}}^{\mathrm{ASOT}} \\ \tau_{\mathrm{B}}^{\mathrm{ASOT}} \end{bmatrix} = \begin{bmatrix} \theta_{\mathrm{F}} \\ \theta_{\mathrm{B}}/0.947 \end{bmatrix}. \tag{5.26}$$

Solving Eq. 5.26 gives the top- and bottom-surface ASOT amplitudes.

We apply this method to the 32 nm film used in Fig. 5.7. With a current density of 5×10^{10} A/m^2, we extract $\tau_{\mathrm{T}}^{\mathrm{ASOT}} = -(0.89 \pm 0.01) \times 10^{-6}$ J/m^2 and $\tau_{\mathrm{B}}^{\mathrm{ASOT}} = (0.87 \pm 0.01) \times 10^{-6}$ J/m^2. The error here is estimated based on the ratio of the imaginary and real parts of the extracted result. These results are in good agreement with those extrapolated from the thickness-dependent fitting. Samples with asymmetric structures, such as $\mathrm{AlO_x}$(2)/Py(32)/Cu(3)/$\mathrm{SiO_2}$(3) and $\mathrm{AlO_x}$(2)/Py(32)/Cu(1.5)/Pt(3)/$\mathrm{SiO_2}$(3), are also measured. However, due to the complexity introduced by the extra layers, the extracted results yield non-negligible imaginary components, which is a sign of inaccurate estimation. Therefore, more effort is needed to optimize this method for complex systems.

5.5 Interface Contribution

Since ASOT results in magnetization changes near the surface, the extracted ASOT values may be influenced by spin-orbit interaction at the interface with the capping layer, such as Rashba-Edelstein spin-orbit coupling [107–110]. To determine the relative contribution of such interface effects, we compare the ASOT at the top surface of the $AlO_x(3)/Py(32)/AlO_x(3)$ sample with the total spin-orbit torque (SOT) in a series of control samples, $AlO_x(3)/Py(4)/Cap$, where Cap is varied among $AlO_x(3)$, AlO_y(3, different oxidation time), $SiO_2(3)$, $Cu(3)/SiO_2(3)$ and $Al(3)/SiO_2(3)$. These capping layer materials are often considered to have weak spin-orbit interaction due to their being light elements, but they will change the electrostatic properties of the top interface, thereby changing the interfacial Rashba spin-orbit coupling. The bottom surface is the same as for the 32 nm sample and thus any interfacial contribution from the bottom surface should have similar ASOT conductivity. Since Py is only 4 nm in these control samples (thinner than the exchange length), the magnetization uniformly responds to the total SOT, which is a sum of the ASOTs at the top and bottom surfaces $\tau_{\mathrm{tot}}^{\mathrm{SOT}} = (\tau_{\mathrm{T}}^{\mathrm{ASOT}} + \tau_{\mathrm{B}}^{\mathrm{ASOT}})$. Should there be a significant interface-dependence of the ASOT, a large total SOT will be observed in some of these control samples with asymmetric interfaces. As shown in Fig. 5.12, all samples exhibit total SOT conductivities $\sigma_{\mathrm{tot}}^{\mathrm{SOT}} = \frac{2e}{\hbar}\frac{\tau_{\mathrm{tot}}^{\mathrm{SOT}}}{E}$ of at most 4% of the bottom-surface ASOT conductivity of the 32 nm Py sample. This result suggests that the top-surface ASOT, which varies less than 4% among Py with different capping layers, does not contain a substantial contribution from the interface of the Py with the capping layers.

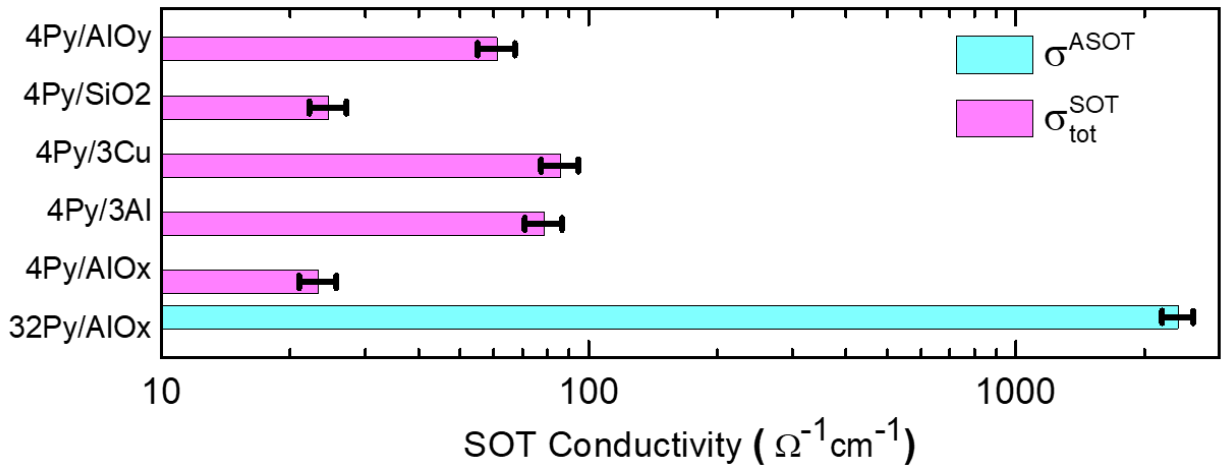

Figure 5.12: Comparison between total SOT conductivities ($\sigma_{\text{tot}}^{\text{SOT}}$) measured for 4 nm Py with different capping layers, and the bottom-surface ASOT conductivity (σ^{ASOT}) of 32 nm. Error bars indicate single standard deviation uncertainties. In all the 4 nm Py samples, the other side of the Py is in contact with AlO_x.

5.6 First-Principles Calculation

The insensitivity of ASOT to the interface implies that it arises from the bulk spin-orbit interaction within the magnetic material. ASOT can be phenomenologically understood as the result of a flow of transverse spin current, which generates ASOT by transferring spin angular momentum from one surface to the other. Together with theorist collaborators, we evaluate the transverse spin current conductivity using density functional theory. We compute the full spin-current conductivity tensor $\sigma_{\alpha\beta}^{\gamma}$ using the linear response Kubo formalism in the clean limit [111]:

$$\sigma_{\alpha\beta}^{\gamma} = 2\text{Im}\frac{e^2}{\hbar}\int \frac{dk}{(2\pi)^3}\sum_{n\neq m} f_{n,k}\frac{<\psi_n|Q_{\alpha\beta}|\psi_m><\psi_m|v_\gamma|\psi_n>}{(E_n - E_m)^2}, \tag{5.27}$$

where $f_{n,k}$ is the Fermi factor, v_γ is the velocity operator along the γ-direction: $v_\gamma = dH/dk_\gamma$, and $Q_{\alpha\beta}$ is the spin current corresponding to the α-component spin flowing in the β-direction. Its operator form is $Q_{\alpha\beta} = (v_\alpha s_\beta + s_\alpha v_\beta)/2$, where s_β is the β-component of the Pauli spin matrices. The above expression is evaluated within density functional theory. The ground state is computed with the Quantum Espresso package [112], where we use the experimental

lattice constants of (0.286, 0.352, 0.2507) nm for Fe (BCC), Ni (FCC), Co (HCP with c-axis perpendicular to the film plane), respectively. In each case, the plane-wave cutoff energy is set to 120 Ryd, and a 12 × 12 × 12 uniform k-point grid is used. We use ultrasoft, fully relativistic pseudopotentials with GGA functional. For Ni, we use the GGA+U method as described in Ref. [113], with $U = 1.9$ eV and $J = 1.2$ eV. To evaluate Eq. 5.15 on a fine k-point mesh, we perform Wannier interpolation using Wannier90 [114]. The integral is evaluated with 200^3 k-points, and we use an adaptive mesh technique in which k-points with integrand larger than 0.28 nm^2 are evaluated on a refined grid. The reported values are numerically converged to within 1 %. The magnetization is along the x-direction, consistent with Fig. 5.1(b). First-principles calculations for Ni, Fe and Co all show significant ASOT conductivities, summarized in Table 5.1.

		Ni	Fe	Co
Calculation	Structure	FCC	BCC	HCP
	AHE Conductivity	-1.3	0.72	0.45
	ASOT Conductivity	3.8	1.04	-0.24
Experiment	Structure	FCC	BCC	HCP
	Conductivity	56	32	46
	AHE Conductivity	-1.3	0.72	0.45
	ASOT Conductivity	3.8	1.04	-0.24

Table 5.1: **Measured and calculated electrical, AHE and ASOT conductivities.** All values have units of 10^3 Ω^{-1}cm^{-1}. All experimental data are extrapolated based on 40 nm sputtered polycrystalline films, sandwiched between two 3 nm AlO_x layers. The positive sign for the ASOT conductivity corresponds to the scenario that if the applied electric field is in the x-direction, the generated spin current flowing in the z-direction has spin moment in the -y-direction. Under this choice, the spin Hall conductivity of Pt is positive.

We also measure the ASOT conductivities of these materials experimentally, provided in Table 5.1. The conductivities are similar in magnitude as those calculated, indicating that the intrinsic mechanism may significantly contribute to the ASOT. However, the signs for Fe and Co are opposite between measured and calculated values; this may indicate that the

intrinsic mechanism is not the sole source for ASOT, and that other mechanisms should be taken into account. In analogy with the AHE, we expect that extrinsic mechanisms such as skew scattering [97, 115] could also contribute to generating transverse spin current and hence ASOT. An illustration of the skew-scattering mechanism is shown in Fig. 5.13.

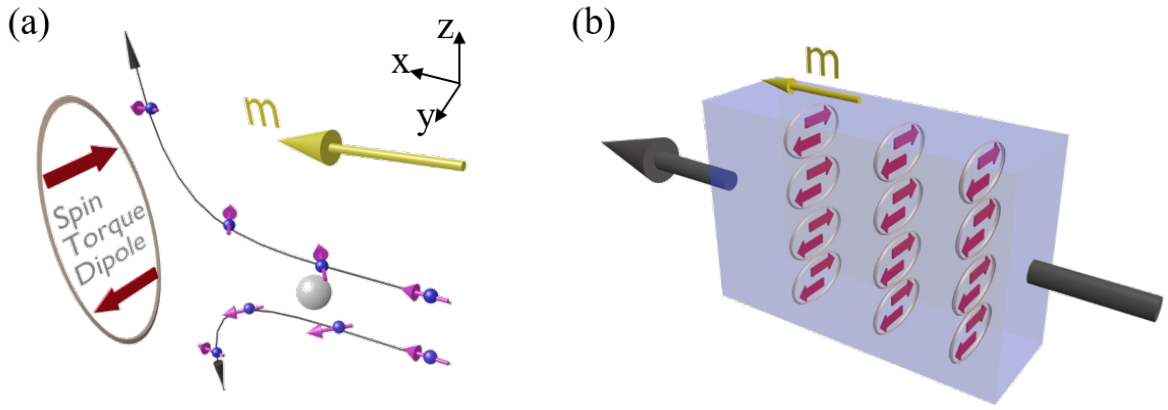

Figure 5.13: (a) Illustration of a Skew scattering-induced spin torque dipole. As x-polarized electrons are scattered by an impurity, the spin orbit interaction (SOI) generates an effective magnetic field $B_{\text{eff}} \propto E_{\text{scatter}} \times v$, where E_{scatter} is the electric field due to the impurity and v is the velocity of the electron. Depending on the scattering trajectory, B_{eff} has opposite directions above and below the scattering center, which rotates the electron spin toward the $+y$ and $-y$ directions. The electron spin is soon repolarized to the x-direction due to dephasing. The additional spin angular momentum gained via the SOI is transferred into the magnetization, which leads to an effective spin torque dipole separated by a distance on the order of the spin dephasing length. (b) A collection of spin torque dipoles in a uniform magnetic film gives rise to identical amplitude but opposite direction of ASOTs at the two surfaces, shown in Fig. 5.1(b).

5.7 Conclusion

In conclusion, our results unambiguously reveal a bulk spin-orbit effect of transverse spins in magnetic metals that is closely related to the well-known anomalous Hall effect. This work sheds light on recently reported nontrivial interconversion between charge and transverse spins in magnetic multilayers [110, 116–118], for which the origin remained unclear. More generally, this work challenges the fundamental understanding of SOT in magnetic multilayer experiments in which transverse spins arising in the magnetic materials have been overlooked. For example, current-induced SOT in magnetic/nonmagnetic bilayers has been widely attributed to the spin Hall effect in the nonmagnetic film and the Rashba effect at the interface. The existence of a large ASOT suggests that the spin-orbit coupling of the magnetic film can also have non-negligible contributions to the SOT in magnetic/nonmagnetic bilayers. Proper design of the magnetic film to enable strong charge-to-transverse-spin conversion can enhance SOT toward efficient electrical control of magnetism. The possibility of this application is explored in the next chapter.

Chapter 6

Self-Generated Spin-Orbit Torques in Magnetic Multilayers

Part of this chapter will be published in "Self-Spin-Orbit Torques in Magnetic Multilayers," by Tao Wang*, Wenrui Wang*, Angie Davidson, Yang Wang, Shane R. Allen, David G. Cahill, Virginia O. Lorenz, John Q. Xiao, and Xin Fan, manuscript in preparation (*Contribute equally).

6.1 Introduction

Current-induced SOTs in magnetic multilayers can enable efficient manipulation of magnetization and magnetic textures. Typical structures in SOT studies involve bilayers of ferromagnetic metal (FM) and spin-source metal (SSM) [30, 68, 73, 74, 119]. The SSMs are often materials exhibiting strong spin-orbit coupling, such as Pt, β-Ta, and topological insulators. Researchers have tended to believe the origin of SOTs in such bilayer systems is solely the spin-orbit effects in the SSM. As shown in Fig. 6.1(a), a spin current generated either in the bulk of the SSM or at the SSM/Cu interface propagates through the Cu spacer layer and reaches the FM, thanks to copper's long spin diffusion length. This leads to SOTs on the FM by spin momentum transfer from the transverse spins to the local magnetization. Because of the weak spin-orbit coupling in Cu, contributions from the FM side have been mostly neglected. However, according to our results in Chapter 5 and several other recent reports [110, 116–118], an electrical current may also generate a spin current in the FM or at the FM/Cu interface due to the spin-orbit coupling of the FM. As illustrated in Fig. 6.1(b),

if a spin current carrying transverse spin is generated from the FM and "absorbed" by the SSM, due to momentum conservation, it should exert SOTs back onto the FM. Since these torques arise from the FM itself, we name them self-spin-orbit torques (SSOT).

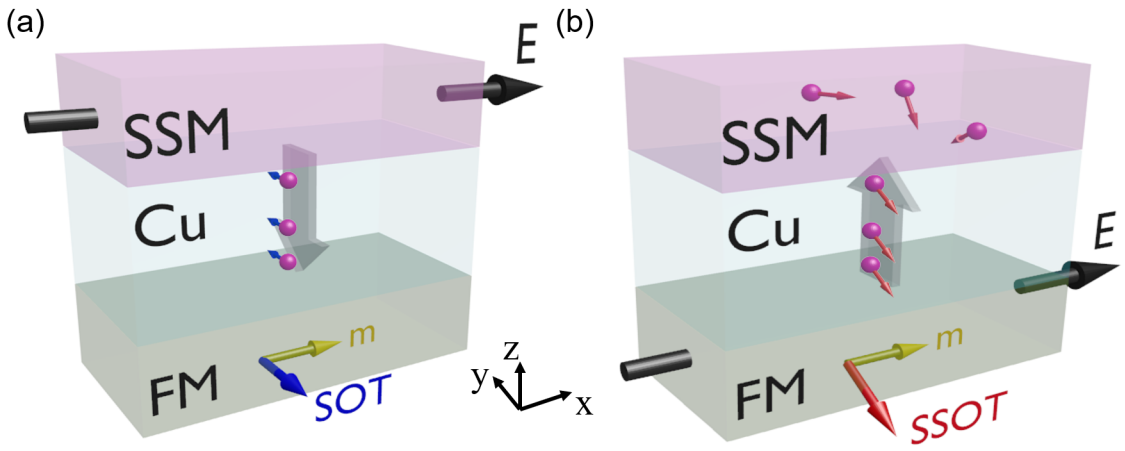

Figure 6.1: **Illustration of the conventional SOT and the SSOT.** (a) Illustration of the SOT that was conventionally thought to be caused by the spin current generated from the bulk SSM or the SSM/Cu interface. The spin current flowing through Cu is a pure spin current composed of equal and opposite spin species flowing in opposite directions. (b) Illustration of the SSOT due to spin current generated from the FM or the FM/Cu interface, which is then dissipated by spin scattering in the bulk of the SSM or by spin relaxation at the SSM/Cu interface.

In this chapter, we first demonstrate SSOT in a FM1/Cu/FM2 spin-valve structure with MOKE magnetometry. To quantitatively characterize the SSOT, we develop and apply a new calibration method to separately analyze the MOKE signals from the two FM layers. The effective SSOT conductivity of $Ni_{80}Fe_{20}$ (Py) is found to be 17% of the total SOT conductivity in a Py/Cu/Pt trilayer, which is too significant to be ignored. These results are consistent with our prediction that there is a spin current generated by the FM spin-orbit effect, which, in turn, leads to SSOT on the FM itself.

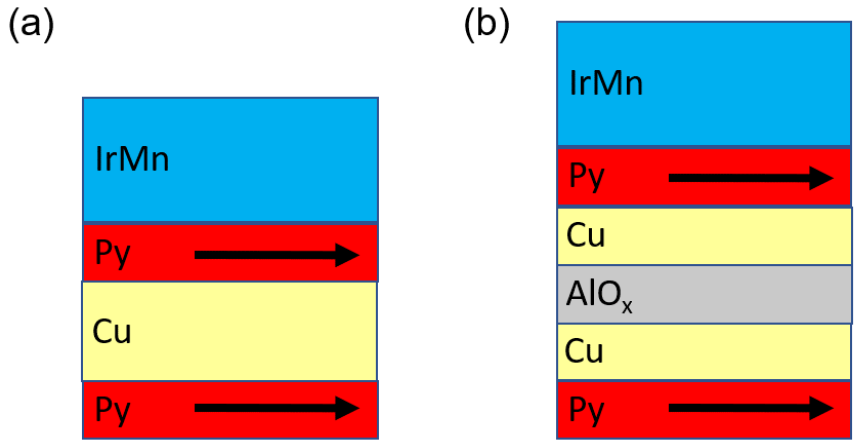

Figure 6.2: Illustration of (a) the test sample and (b) control sample structures.

6.2 Observation of the SSOT

To experimentally demonstrate the SSOT, we measure the SOT-induced magnetization tilting in a test sample with spin-valve structure:
substrate/Py(3)/Cu(6)/Py(3)/IrMn(15)/SiO_2(5) (see Fig. 6.2(a)), where the values in parentheses are in nanometers. In this experiment, the substrate is a silicon wafer with 1 μm thermal oxide; the first Py is a free magnetic layer; the magnetization of the second Py layer is pinned by the antiferromagnetic IrMn layer, giving rise to a shifted magnetization hysteresis; the Cu layer is a spacer layer that decouples the magnetization between the two Py layers, while still allowing the flow of spin current; the SiO_2 is a capping layer. The sample is patterned to a 50 μm $\times$ 50 μm square. For comparison, a control sample is also prepared with structure: substrate/Py(3)/Cu(3)/AlO_x(3)/Cu(3)/Py(3)/IrMn(15)/SiO_2(5) (see Fig. 6.2(b)), where the additional AlO_x is an insulating layer that blocks the spin currents flowing between the two Py layers. As shown in Fig. 6.4(a-b), this spin current "cut-off" is confirmed via giant magnetoresistance (GMR) measurements. The test sample exhibits $\approx 1.2\%$ GMR, while the GMR in the control sample is significantly suppressed by the AlO_x layer.

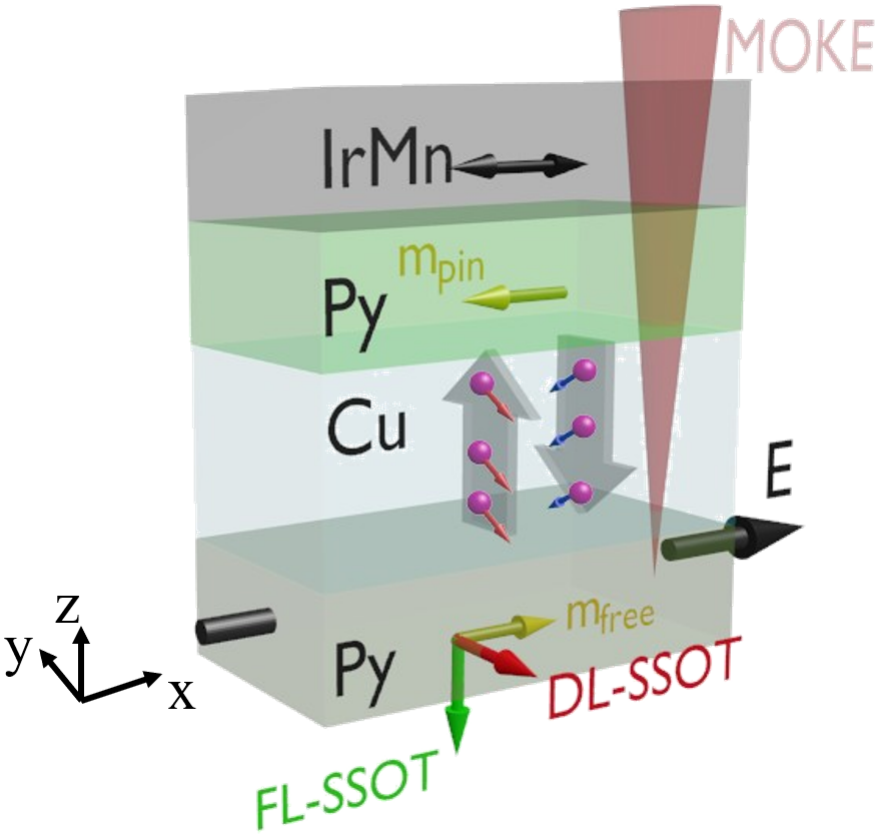

Figure 6.3: Diagram of current-induced spin currents and SSOT in a Py/Cu/Py/IrMn spin valve structure. The SSOT acting on the Py free-layer should only arise from the spin current generated by both Py layers. Moreover, the SSOT can be decomposed into DL-SSOT and FL-SSOT.

We then measure the SSOT using the MOKE-based SOT magnetometer introduced in Chapter 3. As we predicted in the last section, an electrical current parallel with the magnetization can generate a transverse spin current flowing out of the FM layers. Therefore, within such a spin-valve structure, there should be two transverse spin currents flowing between the two Py layers, as illustrated in Fig. 6.3. These spin currents lead to SOTs on both Py layers. Like normal SOTs, SSOT has damping-like (DL) and field-like (FL) terms. In this specific sample structure, DL-SSOT tilts the magnetization of both Py layers out of plane, which can be measured by the polar MOKE. A more detailed SSOT analysis is discussed in the next section; here we briefly present the main result. In the first experiment, we measure the SOT-induced polar MOKE signal in the control sample. The MOKE signal

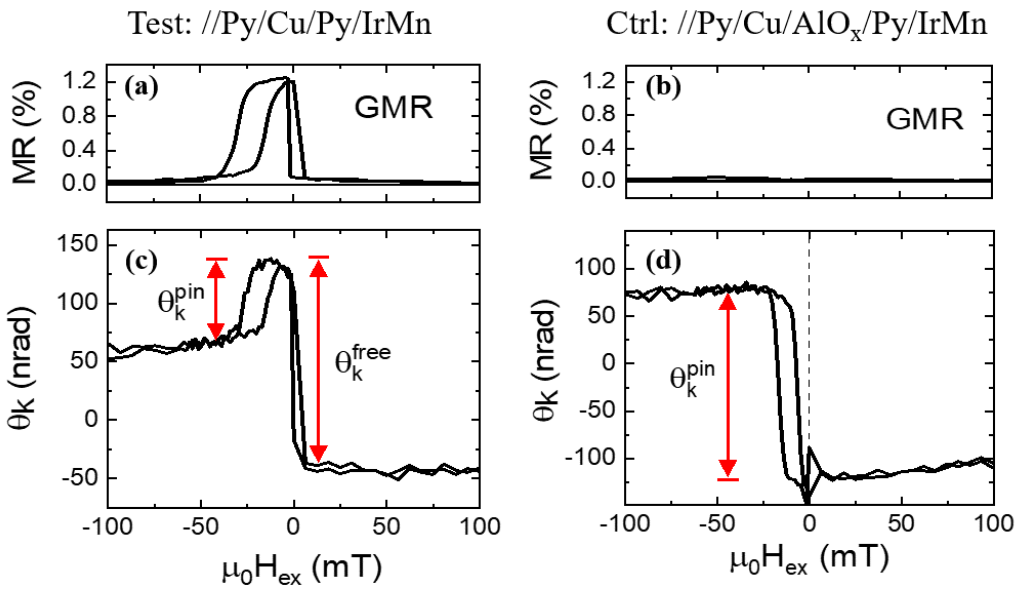

Figure 6.4: **GMR and MOKE results of the test and control samples.** (a, b) Magnetoresistance measured via the four-point-probe method. The test sample exhibits 1.2% GMR, while no noticeable GMR is measured in the control sample. (c, d) SOT-induced out-of-plane magnetization tilting measured by the MOKE-base SOT magnetometer. In the test sample, there is a strong SOT acting on the Py free-layer, while in the control sample, the SOT on the Py free-layer is negligible. The $y = 0$ dashed line indicates that there is no observable m_{free} hysteresis. In addition, the sign of the SOT acting on the Py pinned layer is reversed between the test and control samples.

due to a DL-SOT should resemble a magnetization hysteresis. As shown in Fig. 6.4(d), the pinned Py layer exhibits a clear hysteresis-like MOKE signal, suggesting a net SOT on the pinned Py layer originating in the AlO_x/Cu/Py/IrMn multilayer, consistent with previous reports [119]. However, there is nearly zero SOT on the free Py layer in the SiO_2/Py/Cu/AlO_x multilayer, because of the weak spin-orbit coupling in Cu. On the other hand, in the test sample signal shown in Fig. 6.4(c), there is a significant net SOT acting on the free Py layer. Moreover, the net SOT acting on the pinned Py layer is reversed from that in the control sample. These results unambiguously confirm our prediction that there is a spin current flowing between the two Py layers in the test sample. Such a transverse

spin current transfers spin angular momentum from one Py layer to the other, resulting in SSOT on both Py layers with equal magnitude and opposite directions. The reversal of the MOKE signal for the pinned layer indicates the SSOT from the Py layer is even greater than the SOT arising from the Py/IrMn interface.

6.3 Discussion of Spin-Orbit Torques in a Spin-Valve Structure

As discussed in the previous section, both FM layers in the spin-valve can generate spin currents that flow through the Cu spacer layer and lead to SOTs. Therefore, for both qualitative and quantitative analysis purposes, it is necessary to understand the effects of the possible SOTs on each FM layer. In this section, we summarize the possible SOTs in a FM1/Cu/FM2 trilayer and their symmetries.

Generally speaking, a spin current $\mathbf{Q_s}$ with spin polarization $\mathbf{s}$ can exert two types of SOTs on a magnetization $\mathbf{m}$: a damping-like torque in the direction of $\mathbf{m} \times (\mathbf{m} \times \mathbf{s})$ and a field-like torque in the direction of $\mathbf{m} \times \mathbf{s}$. The damping-like torque is equivalent to an effective field in the direction of $\mathbf{m} \times \mathbf{s}$, and the field-like torque is equivalent to an effective field in the direction of $\mathbf{s}$. Normally, when an electric current is applied parallel to the magnetization of a magnetic film, it generates a spin current with spin polarization $\mathbf{s}$ that is in the film plane and transverse to the current (magnetization). This spin current yields the same symmetry as that of the spin Hall effect and is thus referred to as the conventional spin-Hall-like current in this chapter. Moreover, according to two recent papers [110, 118], the current-induced spin current in a magnetic material also possesses spin polarization components in the $\mathbf{s'} = \mathbf{m} \times \mathbf{s}$ direction. Since $\mathbf{s'}$ is essentially a 90 degree rotation of $\mathbf{s}$ around the magnetization $\mathbf{m}$, we name this spin current component as the spin rotation current. As a result, the transversely flowing spin current in the magnetic film can be decomposed into two components: (1) conventional spin-Hall-like component $\mathbf{Q_s^C}$ with spin

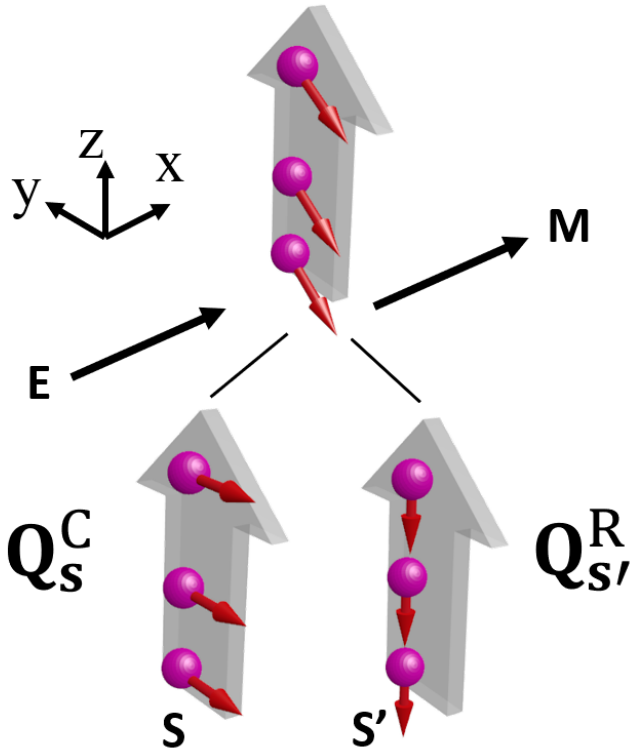

Figure 6.5: The spin current generated from the FM or the FM/Cu interface can be decomposed into a spin current with conventional spin Hall symmetry $\mathbf{Q_s^C}$, and a spin current with spin rotation symmetry $\mathbf{Q_{s'}^R}$. $\mathbf{s}$ and $\mathbf{s}'$ represent the spin polarization of the conventional and spin rotation currents, respectively. $\mathbf{E}$ is the applied electric field and $\mathbf{M}$ is the magnetization of the magnetic layer.

polarization $\mathbf{s}$ following $\mathbf{s}||\mathbf{j_e} \times \mathbf{Q_s^C}$, and spin rotation component $\mathbf{Q_{s'}^R}$ with spin polarization following $\mathbf{s'}||\mathbf{m} \times \mathbf{s}$. An illustration of the two spin current components is shown in Fig. 6.5.

In a spin-valve structure FM1/Cu/FM2, each of the two FM layers generates spin current carrying two spin polarizations. Therefore, for each FM layer, there are 8 possible SOTs acting on the magnetization. In Table 6.1, we summarize the symmetries of the effective magnetic fields due to the SOTs on FM1 magnetization $\mathbf{m_1}$. Similarly, the effective fields of SOTs acting on the magnetization of FM2 are summarized in Table 6.2.

In our sample structure, FM1 is the free Py layer and FM2 is the pinned Py layer. Since polar MOKE is only sensitive to the out-of-plane magnetization component, the detected

	Spin current from FM1		Spin current from FM2	
	$\mathbf{Q_s^C}$	$\mathbf{Q^R_{m1\times s}}$	$\mathbf{Q_s^C}$	$\mathbf{Q^R_{m2\times s}}$
Field-like	$\mathbf{s}$	$\mathbf{m_1 \times s}$	$\mathbf{s}$	$\mathbf{m_2 \times s}$
Damping-like	$\mathbf{m_1 \times s}$	$\mathbf{s}$	$\mathbf{m_1 \times s}$	$\mathbf{m_1 \times (m_2 \times s)}$

Table 6.1: Summary of the effective field directions caused by the SOTs on FM1 magnetization $\mathbf{m_1}$. Here, $\mathbf{s}$ is the spin polarization direction of the conventional spin current; $\mathbf{m_1}$ and $\mathbf{m_2}$ are the magnetization vectors of FM1 and FM2, respectively.

	Spin current from FM1		Spin current from FM2	
	$\mathbf{Q_s^C}$	$\mathbf{Q^R_{m1\times s}}$	$\mathbf{Q_s^C}$	$\mathbf{Q^R_{m2\times s}}$
Field-like	$\mathbf{s}$	$\mathbf{m_1 \times s}$	$\mathbf{s}$	$\mathbf{m_2 \times s}$
Damping-like	$\mathbf{m_2 \times s}$	$\mathbf{m_2 \times (m_1 \times s)}$	$\mathbf{m_2 \times s}$	$\mathbf{s})$

Table 6.2: Summary of the effective field directions caused by the SOTs on FM2 magnetization $\mathbf{m_2}$.

MOKE signal should be from the SOTs providing out-of-plane effective fields. Specifically, the SOTs yielding effective fields in the $\mathbf{m_1 \times s}$ direction should be responsible for the MOKE signal resembles a $\mathbf{m_1}$ hysteresis. All the SOTs that lead to effective fields with $\mathbf{m_1 \times s}$ direction are highlighted in Table 6.1 and 6.2, including damping-like torques on $\mathbf{m_1}$ due to conventional spin currents generated by both free and pinned layers, and field-like torques on $\mathbf{m_1}$ and $\mathbf{m_2}$ due to spin rotation current generated by the free-layer. Based on this result, the detected free-layer MOKE signal in Fig. 6.4(c) actually has contributions from both the free and pinned layers. Therefore, it is necessary to separate the MOKE signals of free and pinned layers for accurate quantitative SSOT analysis.

6.4 Separating MOKE Signals from Two FM Layers

To separate the MOKE signal from free and pinned Py layers in the test sample, we perform a comprehensive calibration process. In general, the MOKE signal is determined by the Kerr coefficients and magnetization. The Kerr coefficients depend on the light scattering

path. Therefore, even for two magnetic layers that are made of the same material, their Kerr coefficients can be drastically different. Mathematically, polar MOKE signals due to an out-of-plane magnetization component m_z can be expressed as

$$\Psi_k + i\Omega_k = (\theta_k + i\epsilon_k)m_z, \tag{6.1}$$

where Ψ_k and Ω_k are the Kerr rotation and ellipticity angle, respectively, and θ_k and ϵ_k are the corresponding Kerr rotation and ellipticity coefficients, respectively. Applying Eq. 6.1 to the spin valve systems shown in Fig. 6.2, the overall polar MOKE signal can be written as

$$\Psi_k + i\Omega_k = (\theta_k^{\text{free}} + i\epsilon_k^{\text{free}})m_z^{\text{free}} + (\theta_k^{\text{pin}} + i\epsilon_k^{\text{pin}})m_z^{\text{pin}}, \tag{6.2}$$

where superscripts "free" and "pin" denote the magnetizations and coefficients of the corresponding Py layers. To determine the Kerr coefficients of the free and pinned layers, we applied an external calibration magnetic field h_{Cal}. Under this calibration field, the out-of-plane magnetization tilting of free and pinned layers can be calculated as

$$m_z^{\text{free}} = \frac{h_{\text{Cal}}}{M_{\text{eff}}^{\text{free}} + |H_{\text{ext}}|}, \tag{6.3}$$

and

$$m_z^{\text{pin}} = \frac{h_{\text{Cal}}}{M_{\text{eff}}^{\text{pin}} + |H_{\text{ext}} + H_{\text{bias}}|}, \tag{6.4}$$

where $M_{\text{eff}}^{\text{free}}$ and $M_{\text{eff}}^{\text{pin}}$ are the effective demagnetizing field for free and pinned layers, respectively, H_{ext} is the external magnetic field, and H_{bias} is the exchange bias field applied on the pinned layer due to the antiferromagnetic IrMn. The Kerr rotation and ellipticity signal due to these magnetization tilts can then be described by

$$\Psi_k = \theta_k^{\text{free}} \frac{h_{\text{Cal}}}{M_{\text{eff}}^{\text{free}} + |H_{\text{ext}}|} + \theta_k^{\text{pin}} \frac{h_{\text{Cal}}}{M_{\text{eff}}^{\text{pin}} + |H_{\text{ext}} + H_{\text{bias}}|}, \tag{6.5}$$

and

$$\Omega_k = \epsilon_k^{\text{free}} \frac{h_{\text{Cal}}}{M_{\text{eff}}^{\text{free}} + |H_{\text{ext}}|} + \epsilon_k^{\text{pin}} \frac{h_{\text{Cal}}}{M_{\text{eff}}^{\text{pin}} + |H_{\text{ext}} + H_{\text{bias}}|}. \tag{6.6}$$

We measure the Kerr rotation and ellipticity signal due to the calibration field as a function of external magnetic field H_{ext}. We also characterize the effective demagnetizing fields $M_{\text{eff}}^{\text{free}}$ and $M_{\text{eff}}^{\text{pin}}$ through ferromagnetic resonance (FMR) measurements and H_{bias} with magnetometry measurements. Therefore, the Kerr coefficients of both free and pinned layers can be extracted by fitting the Kerr rotation and ellipticity data with Eq. 6.5 and Eq. 6.6, respectively.

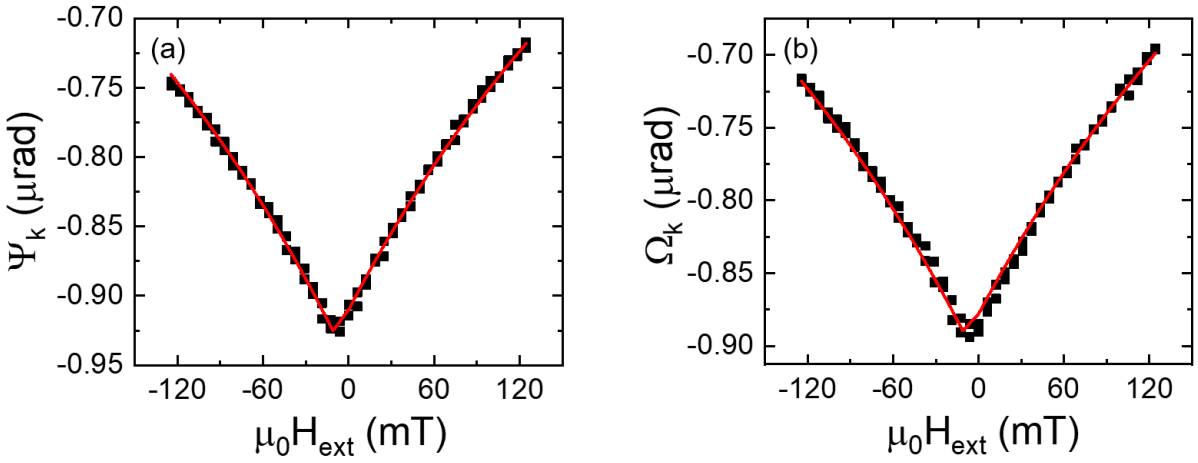

Figure 6.6: Illustration of the Kerr coefficient calibration fitting of (a) Kerr rotation and (b) Kerr ellipticity. Black squares are the experimental data. Red curves are the fitting curves based on Eq. 6.5 and Eq. 6.6. Constant parameters used in this fitting are: $M_{\text{eff}}^{\text{free}} = 7136$ Oe, $M_{\text{eff}}^{\text{pin}} = 4012$ Oe, $H_{\text{bias}} = -250$ Oe, and $h_{\text{Cal}} = -9.70$ Oe.

As long as we know all the Kerr coefficients, we can then measure the SOT-induced Kerr rotation Ψ_k^{SOT} and ellipticity Ω_k^{SOT} and extract the corresponding magnetization tilting in the two Py layers with

$$m_z^{\text{free}} = \frac{\epsilon_k^{\text{pin}} \Psi_k^{\text{SOT}} - \theta_k^{\text{pin}} \Omega_k^{\text{SOT}}}{\epsilon_k^{\text{pin}} \theta_k^{\text{free}} - \epsilon_k^{\text{free}} \theta_k^{\text{pin}}}, \tag{6.7}$$

and

$$m_z^{\text{pin}} = \frac{\epsilon_k^{\text{free}}\Psi_k^{\text{SOT}} - \theta_k^{\text{free}}\Omega_k^{\text{SOT}}}{\epsilon_k^{\text{free}}\theta_k^{\text{pin}} - \epsilon_k^{\text{pin}}\theta_k^{\text{free}}}. \tag{6.8}$$

We demonstrate this fitting method with the control sample. As shown in Fig. 6.6, the calibration fitting curves match the experimental data very well. The extracted Kerr coefficients are: $\theta_k^{\text{free}} = (1.69 \pm 0.02) \times 10^{-4}$, $\theta_k^{\text{pin}} = (2.90 \pm 0.02) \times 10^{-4}$, $\epsilon_k^{\text{free}} = (2.15 \pm 0.01) \times 10^{-4}$, $\theta_k^{\text{free}} = (2.49 \pm 0.01) \times 10^{-4}$ (uncertainties are the fitting errors).

Using the extracted Kerr coefficients, we disentangle the SOT-induced MOKE signal from the two Py layers using Eq. 6.7 and Eq. 6.8. The extracted out-of-plane magnetization tilting of the free and pinned layers are shown in Fig. 6.7. In Fig. 6.7(a), the free layer yields no significant magnetization tilting, because the AlO_x blocks all the spin currents. On the other hand, as shown in Fig. 6.7(b), the pinned-layer magnetization tilting resembles a m_{pin} hysteresis, a signature of the SOTs generated at the Py/IrMn interface.

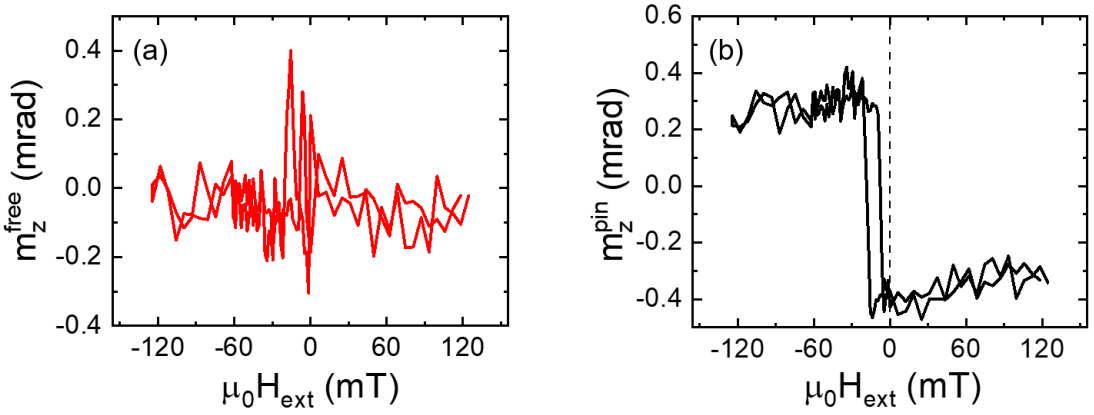

Figure 6.7: Extracted SOT-induced magnetization tilting of (a) the free Py layer, (b) the pinned Py layer in the control sample. The $y = 0$ dashed line indicates that there is no observable m_{free} hysteresis.

As a result, the separated magnetization tilting successfully reflects the predicted SOTs in the control sample. This result verifies our MOKE calibration method is reliable in separating MOKE response from two magnetic layers. The separated results make individual

analysis of the free layer possible, which significantly benefits the SSOT-analysis process.

6.5 Quantitative Analysis of the SSOT

In this section, we quantitatively analyze the strength of the SSOT in Py. Applying the calibration method discussed in the last section to the test sample, we extract the SOT-induced magnetization tilting in the free and pinned layers, as shown in Fig. 6.8.

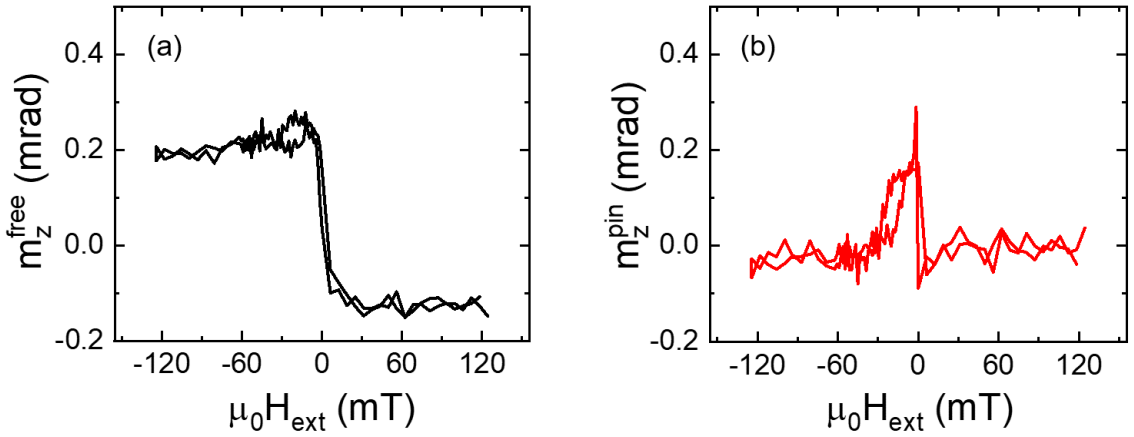

Figure 6.8: Extracted SOT-induced magnetization tilting of (a) the free Py layer, (b) the pinned Py layer in the test sample.

As summarized in Tables 6.1 and 6.2, there are three SOT-induced $\mathbf{m_{free}} \times \mathbf{s}$-symmetry effective fields on the free layer and one on the pinned layer. These fields are responsible for the $\mathbf{m_{free}}$-hysteresis-like out-of-plane magnetization tilting observed in Fig. 6.8. The polar MOKE signal can be expressed as

$$\begin{aligned}(\Psi_k + i\Omega_k)|_{\mathbf{m_{free}}} =& (\theta_k^{\text{free}} + i\epsilon_k^{\text{free}}) \frac{h_{\text{C-DL}}^{\text{free}} + h_{\text{C-DL}}^{\text{pin}} + h_{\text{SR-FL}}^{\text{free}}}{M_{\text{eff}}^{\text{free}} + |H_{\text{ext}}|} \\ &+ (\theta_k^{\text{pin}} + i\epsilon_k^{\text{pin}}) \frac{-h_{\text{SR-FL}}^{\text{free}}}{M_{\text{eff}}^{\text{pin}} + |H_{\text{ext}} + H_{\text{bias}}|},\end{aligned} \tag{6.9}$$

where the first and second terms correspond to the polar MOKE response from the free

layer (Fig. 6.8(a)) and pinned layer (Fig. 6.8(b)), respectively, $h^{\text{origin}}_{\text{SOT}-\text{type}}$ is the effective field exhibiting $\mathbf{m_{free}} \times \mathbf{s}$-symmetry, and $\text{C}-\text{DL}$ and $\text{SR}-\text{FL}$ stand for "conventional-damping-like" and "spin-rotation-field-like", respectively. From Fig. 6.8(b), we can extract $h^{\text{free}}_{\text{C}-\text{DL}}$ by analyzing the magnetization tilting change at zero field. Based on the second term in Eq. 6.9, we get $h^{\text{free}}_{\text{SR}-\text{fL}} = (0.45 \pm 0.06)$ Oe. Since the $h^{\text{free}}_{\text{SR}-\text{FL}}$ acting on the two layers are counter to each other and $h^{\text{free}}_{\text{C}-\text{DL}} = h^{\text{pin}}_{\text{C}-\text{DL}}$, we can then solve $h^{\text{free}}_{\text{C}-\text{DL}} = h^{\text{free}}_{\text{C}-\text{DL}} = -(0.97 \pm 0.12)$ Oe by analyzing the zero-field tilting change in the free-layer. Here, $h^{\text{free}}_{\text{C}-\text{DL}}$ is the caused by SSOT. Therefore, using these results, we derive the SSOTs arising from the Py to be $\tau^{\text{DL}-\text{SSOT}}_{\text{Py}} = h^{\text{free}}_{\text{C}-\text{DL}}\mu_0 M_{\text{s}} d = (0.23 \pm 0.03) \times 10^{-6}$ J/m^2 and $\tau^{\text{FL}-\text{SSOT}}_{\text{Py}} = h^{\text{free}}_{\text{SR}-\text{FL}}\mu_0 M_{\text{s}} d = -(0.11 \pm 0.02) \times 10^{-6}$ J/m^2, where $\mu_0 M_{\text{s}} = 1$ T is the saturation magnetization, and $d = 3$ nm is the thickness of the free Py layer (signs here follow the convention that Pt has a positive spin-torque conductivity). Since the test sample is a multilayer structure, it is difficult to accurately characterize the current density in the Py layers. Thus, we calculate the corresponding spin-Hall-like SSOT conductivities for Py as $\sigma^{\text{DL}-\text{SSOT}}_{\text{Py}} = \frac{2e}{\hbar}\frac{\tau^{\text{DL}-\text{SSOT}}_{\text{Py}}}{E} = (554 \pm 60)\ \Omega^{-1}\text{cm}^{-1}$ and $\sigma^{\text{FL}-\text{SSOT}}_{\text{Py}} = \frac{2e}{\hbar}\frac{\tau^{\text{FL}-\text{SSOT}}_{\text{Py}}}{E} = -(253 \pm 50)\ \Omega^{-1}\text{cm}^{-1}$, where E is the applied electric field. These values are close to the total spin-torque conductivity in Py/IrMn, $(592 \pm 30)\ \Omega^{-1}\text{cm}^{-1}$, which is extracted from Fig. 6.7(b). The extracted $\sigma^{\text{DL}-\text{SSOT}}_{\text{Py}}$ is only about 24% of that from the single-layer Py study in Chap. 5. This result indicates that the spin transparency of the interfaces through which spin current is injected may play an important role in the spin-torque efficiency.

For a quantitative comparison, we also measure the SOTs in a second control sample (Pt-Control): substrate/Py(3)/Cu(3)/Pt(3)/AlO_{x}(3)/Cu(3)/Py(3)/IrMn(15)/SiO_2(5), in which the free Py layer experiences a net SOT due to the additional Pt. This net SOT is measured by Kerr rotation and ellipticity measurements, shown in Fig. 6.9(a, b). In addition to the pinned-layer signal, which we observed in the control sample, there is a large free-layer signal resembling $\mathbf{m_{free}}$-symmetry. The extracted magnetization tilting in the free and pinned layers are shown in Fig. 6.9(c, d). As expected, the pinned-layer tilting is very similar to

that observed in Fig. 6.7(b). From Fig. 6.9(c), we extract the total spin-torque conductivity in the Py/Cu/Pt to be $\sigma^{\mathrm{SOT}} = (1778 \pm 50)\ \Omega^{-1}\mathrm{cm}^{-1}$.

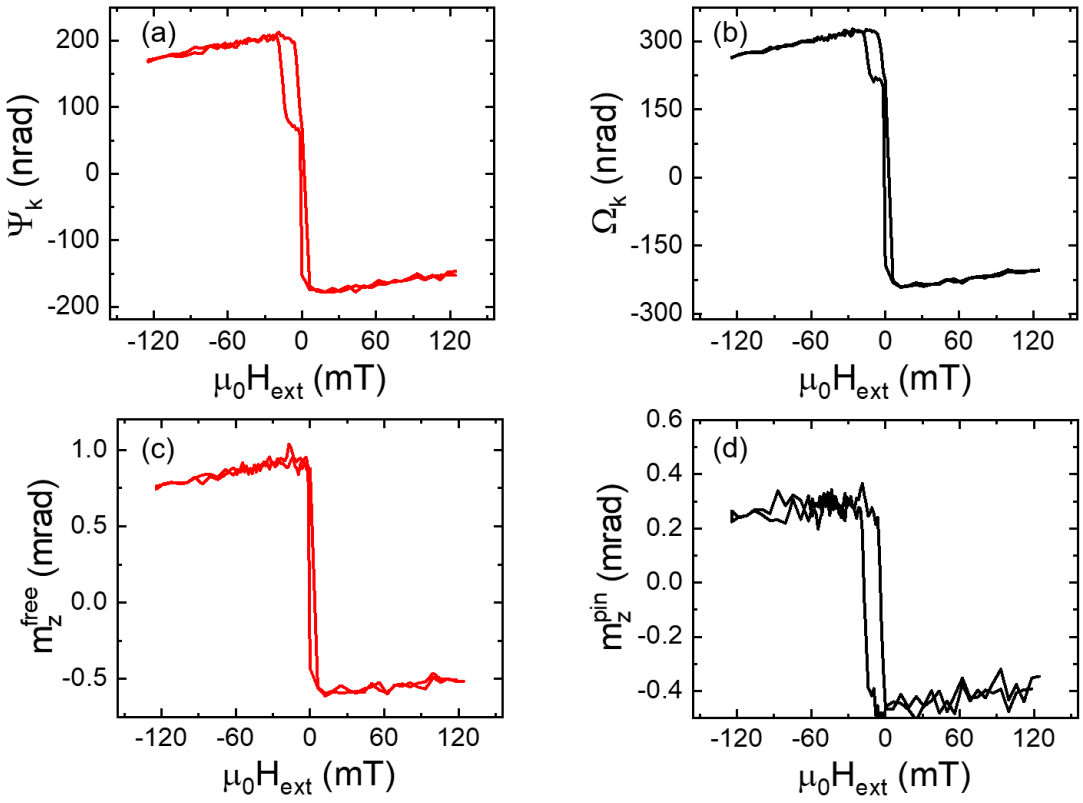

Figure 6.9: (a) Kerr rotation and (b) Kerr ellipticity data, and the extracted SOT-induced magnetization tilting of (c) the free Py layer, (d) the pinned Py layer in the Pt-Control sample.

Since the total SOTs in the Py/Cu/Pt include the SSOT from Py and SOTs from Pt, we can express the total spin torque conductivity as $\sigma^{\mathrm{SOT}}_{\mathrm{Py/Cu/Pt}} = \sigma^{\mathrm{SOT}}_{\mathrm{Pt}} + \sigma^{\mathrm{DL-SSOT}}_{\mathrm{Py}} + \sigma^{\mathrm{DL-SSOT}}_{\mathrm{Py}}$. Assuming the effective spin torque conductivity of Py is the same in Py/Cu/Py and Py/Cu/Pt, we can estimate the SSOT conductivity as $\sigma^{\mathrm{DL-SSOT}}_{\mathrm{Py}} + \sigma^{\mathrm{FL-SSOT}}_{\mathrm{Py}} = (301 \pm 78)$ $\Omega^{-1}\mathrm{cm}^{-1}$, providing 17% of the total spin torque conductivity in the Py/Cu/Pt trilayer. Considering its universality and large amplitude, the SSOT contribution is too significant to be neglected.

6.6 Conclusion

In recent years, a great amount of effort has been devoted to searching for new SSMs that can generate an efficient total SOT to manipulate magnetizations, with the assumption that the total SOT solely arises from the SSM. Our results show that the FM itself can contribute a considerable amount of SSOT in a FM/SSM system. The SSOT should be take into consideration for extracting the spin torque conductivity of the SSM. Beyond this, the SSOT due to the spin-orbit coupling in the FM is universal in these devices and can itself be harnessed as an additional source for efficient manipulation of the magnetization.

Chapter 7

Conclusions

In this dissertation, I explored current-induced spin-orbit effects and spin-orbit torques specifically originating in magnetic materials. I showed that magneto-optic Kerr effect, a well-known characterization tool in magnetism studies, can also be implemented in spin-orbit effect research. Thanks to the high sensitivity and resolution of the MOKE-based system, I discovered some significant yet long-overlooked spin-orbit phenomena in magnetic systems.

First, I developed and optimized an optical system based on the magneto-optic Kerr effect to realize high-precision spin-orbit torque measurements. Damping-like and field-like spin-orbit torques can both be measured in one normally-incident configuration via polar and quadratic MOKE. Without any averaging, our system yields a ~ 70 nrad polarization rotation sensitivity, which is mainly limited by the electron shot noise in the balanced detector. Based on this fact, I further improved the performance of our system by implementing an "unbalanced-optical-bridge" technique, which can provide a factor of 3 enhancement of the signal-to-noise ratio. As a result, our MOKE-based spin-orbit torque magentometer is a powerful tool for fast and accurate spin-orbit torque characterization. Its high sensitivity enabled us to accomplish the following discoveries in magnetic thin film structures.

With the help of our MOKE system, I observed an anomalous spin-orbit torque at the surfaces of single-layer magnetic thin films when an electrical current is applied parallel with the magnetization. This anomalous spin-orbit torque is very difficult to measure with electrical methods because it leads to a net zero magnetization distribution across the entire magnetic film. The extracted spin-Hall-like efficiency of $Ni_{80}Fe20$ is comparable to the effi-

ciency of Pt, which suggests its great potential in spin-orbitronics applications. After a series of interface-dependent experiments, I speculated the observed torque is caused fundamentally by a spin current generated in the magnetic material with spin polarization transverse to the magnetization direction. Our similar observations and first-principles calculations in other common magnetic materials also suggest this phenomenon is due to an intrinsic and universal spin-orbit effect that exists in all magnetic materials. Therefore, by revealing this long-overlooked spin-orbit effect, we point out a new configuration for spin-orbit effect research in magnetic materials, in which current is parallel to the magnetization (as opposed to perpendicular as in the anomalous Hall effect), opening up more possibilities in spin-orbitronics studies.

As a follow-up study of the new spin-orbit effect, I also studied its related phenomenon, namely, the self-spin-orbit torques, in more complex magnetic multilayer structures. In a spin-valve system, I demonstrated that an electrical current parallel with the magnetization can indeed generate a transverse spin current flowing out of the magnetic material. Moreover, if this spin current is "absorbed" by another material, it will exert spin-orbit torques back on the magnetization. The amplitudes of the spin-orbit torques induced by a spin current from $Ni_{80}Fe20$ are very close to those caused by a $Ni_{80}Fe20$/IrMn interface. This result challenges the current understanding of spin-orbit torques in ferromagnet/non-magnetic spin source metal bilayers, because contributions from the ferromagnet are often ignored. It also opens a new route to realizing efficient electrical control of magnetic moment by wisely engineering magnetic materials so that self-spin-orbit torques work constructively with non-magnetic spin source materials.

The dissertation work was partially supported by the DOE center under Award Number DE-FG02-07ER46374 and the NSF MRSEC under Award Number DMR-1505192.

Chapter 8

References

[1] M. N. Baibich, J. M. Broto, A. Fert, F. Nguyen Van Dau, F. Petroff, P. Etienne, G. Creuzet, A. Friederich, and J. Chazelas. Giant magnetoresistance of (001)fe/(001)cr magnetic superlattices. *Physical Review Letters*, 61(21):2472–2475, 1988. doi: 10.1103/PhysRevLett.61.2472. URL https://link.aps.org/doi/10.1103/PhysRevLett.61.2472.

[2] G. Binasch, P. Grünberg, F. Saurenbach, and W. Zinn. Enhanced magnetoresistance in layered magnetic structures with antiferromagnetic interlayer exchange. *Physical Review B*, 39(7):4828–4830, 1989. doi: 10.1103/PhysRevB.39.4828. URL https://link.aps.org/doi/10.1103/PhysRevB.39.4828.

[3] B. Dieny, V. S. Speriosu, S. S. P. Parkin, B. A. Gurney, D. R. Wilhoit, and D. Mauri. Giant magnetoresistive in soft ferromagnetic multilayers. *Physical Review B*, 43(1):1297–1300, 1991. doi: 10.1103/PhysRevB.43.1297. URL https://link.aps.org/doi/10.1103/PhysRevB.43.1297.

[4] A. Fert and I. A. Campbell. Two-current conduction in nickel. *Physical Review Letters*, 21(16):1190–1192, 1968. doi: 10.1103/PhysRevLett.21.1190. URL https://link.aps.org/doi/10.1103/PhysRevLett.21.1190.

[5] N. F. Mott. The electrical conductivity of transition metals. *Proceedings of the Royal Society of London. Series A - Mathematical and Physical Sciences*, 153(880):699, 1936. URL http://rspa.royalsocietypublishing.org/content/153/880/699.abstract.

[6] Claude Chappert, Albert Fert, and Frédéric Nguyen Van Dau. The emergence of spin electronics in data storage. *Nature Materials*, 6:813, 2007. doi: 10.1038/nmat2024. URL http://dx.doi.org/10.1038/nmat2024.

[7] R. Coehoorn, J. C. S. Kools, Th G. S. M. Rijks, and K. M. H. Lenssen. Giant magnetoresistance materials for read heads. *Philips Journal of Research*, 51(1):93–124, 1998. ISSN 0165-5817. doi: https://doi.org/10.1016/S0165-5817(97)00004-1. URL http://www.sciencedirect.com/science/article/pii/S0165581797000041.

[8] J. S. Moodera, Lisa R. Kinder, Terrilyn M. Wong, and R. Meservey. Large magnetoresistance at room temperature in ferromagnetic thin film tunnel junctions. *Physical Review Letters*, 74(16):3273–3276, 1995. doi: 10.1103/PhysRevLett.74.3273. URL https://link.aps.org/doi/10.1103/PhysRevLett.74.3273.

[9] T. Miyazaki and N. Tezuka. Giant magnetic tunneling effect in fe/al2o3/fe junction. *Journal of Magnetism and Magnetic Materials*, 139(3):L231–L234, 1995. ISSN 0304-8853. doi: https://doi.org/10.1016/0304-8853(95)90001-2. URL http://www.sciencedirect.com/science/article/pii/0304885395900012.

[10] Stuart S. P. Parkin, Christian Kaiser, Alex Panchula, Philip M. Rice, Brian Hughes, Mahesh Samant, and See-Hun Yang. Giant tunnelling magnetoresistance at room temperature with mgo (100) tunnel barriers. *Nature Materials*, 3:862, 2004. doi: 10.1038/nmat1256.

[11] Shinji Yuasa, Taro Nagahama, Akio Fukushima, Yoshishige Suzuki, and Koji Ando. Giant room-temperature magnetoresistance in single-crystal fe/mgo/fe magnetic tunnel junctions. *Nature Materials*, 3:868, 2004. doi: 10.1038/nmat1257. URL http://dx.doi.org/10.1038/nmat1257.

[12] M. Julliere. Tunneling between ferromagnetic films. *Physics Letters A*, 54(3):225–226, 1975. ISSN 0375-9601. doi: https://doi.org/10.1016/0375-9601(75)90174-7. URL http://www.sciencedirect.com/science/article/pii/0375960175901747.

[13] S. Ikeda, J. Hayakawa, Y. Ashizawa, Y. M. Lee, K. Miura, H. Hasegawa, M. Tsunoda, F. Matsukura, and H. Ohno. Tunnel magnetoresistance of 604% at 300k by suppression of ta diffusion in cofeb/mgo/cofeb pseudo-spin-valves annealed at high temperature. 93(8):082508, 2008. doi: 10.1063/1.2976435. URL https://aip.scitation.org/doi/abs/10.1063/1.2976435.

[14] Sabpreet Bhatti, Rachid Sbiaa, Atsufumi Hirohata, Hideo Ohno, Shunsuke Fukami, and S. N. Piramanayagam. Spintronics based random access memory: a review. *Materials Today*, 20(9):530–548, 2017. ISSN 1369-7021. doi: https://doi.org/10.1016/j.mattod.2017.07.007. URL http://www.sciencedirect.com/science/article/pii/S1369702117304285.

[15] S. Lee and K. Lee. Emerging three-terminal magnetic memory devices. *Proceedings of the IEEE*, 104(10):1831–1843, 2016. ISSN 0018-9219. doi: 10.1109/JPROC.2016.2543782.

[16] W.H. Butler, X.-G. Zhang, D.M.C. Nicholson, and J.M. MacLaren. Spin-dependent scattering and giant magnetoresistance. *Journal of Magnetism and Magnetic Materials*, 151(3):354 – 362, 1995. ISSN 0304-8853. doi: https://doi.org/10.1016/0304-8853(95)00507-2. Spin Polarized Electron Transport.

[17] Online Source. Spin transfer torque. URL http://science.sciencemag.org/content/285/5429/867.

[18] J. C. Slonczewski. Current-driven excitation of magnetic multilayers. *Journal of Magnetism and Magnetic Materials*, 159(1):L1–L7, 1996. ISSN 0304-8853. doi: https://doi.org/10.1016/0304-8853(96)00062-5.

[19] L. Berger. Emission of spin waves by a magnetic multilayer traversed by a current. *Physical Review B*, 54(13):9353–9358, 1996. doi: 10.1103/PhysRevB.54.9353. URL https://link.aps.org/doi/10.1103/PhysRevB.54.9353.

[20] E. B. Myers, D. C. Ralph, J. A. Katine, R. N. Louie, and R. A. Buhrman. Current-induced switching of domains in magnetic multilayer devices. *Science*, 285 (5429):867–870, 1999. ISSN 0036-8075. doi: 10.1126/science.285.5429.867. URL http://science.sciencemag.org/content/285/5429/867.

[21] J. A. Katine, F. J. Albert, R. A. Buhrman, E. B. Myers, and D. C. Ralph. Current-driven magnetization reversal and spin-wave excitations in co/cu/co pillars. *Phys. Rev. Lett.*, 84:3149–3152, Apr 2000. doi: 10.1103/PhysRevLett.84.3149.

[22] Yiming Huai, Frank Albert, Paul Nguyen, Mahendra Pakala, and Thierry Valet. Observation of spin-transfer switching in deep submicron-sized and low-resistance magnetic tunnel junctions. *Applied Physics Letters*, 84(16):3118–3120, 2004. doi: 10.1063/1.1707228.

[23] G. D. Fuchs, N. C. Emley, I. N. Krivorotov, P. M. Braganca, E. M. Ryan, S. I. Kiselev, J. C. Sankey, D. C. Ralph, R. A. Buhrman, and J. A. Katine. Spin-transfer effects in nanoscale magnetic tunnel junctions. *Applied Physics Letters*, 85(7):1205–1207, 2004. doi: 10.1063/1.1781769.

[24] Scott. Strong. Everspin announces sampling of industry's first 256mb perpendicular spin torque mram to customers. *The SSD Review*, 2016.

[25] K. Narayanapillai, X. Qiu, Y. Wang, J. Kwon, J. Yu, L. M. Loong, W. Legrand, J. Yoon, K. Banerjee, and H. Yang. Spin-transfer versus spin-orbit torque mram. In *2016 IEEE International Nanoelectronics Conference (INEC)*, pages 1–2. ISBN 2159-3531. doi: 10.1109/INEC.2016.7589383.

[26] M.I. Dyakonov and V.I. Perel. Current-induced spin orientation of electrons in semiconductors. *Physics Letters A*, 35(6):459 – 460, 1971. ISSN 0375-9601. doi: https://doi.org/10.1016/0375-9601(71)90196-4. URL http://www.sciencedirect.com/science/article/pii/0375960171901964.

[27] J. E. Hirsch. Spin hall effect. *Physical Review Letters*, 83(9):1834–1837, 1999. ISSN 0031-9007. doi: 10.1103/PhysRevLett.83.1834. URL <Go to ISI>://WOS:000082242600034.

[28] Jairo Sinova, Dimitrie Culcer, Q. Niu, N. A. Sinitsyn, T. Jungwirth, and A. H. MacDonald. Universal intrinsic spin hall effect. *Phys. Rev. Lett.*, 92:126603, Mar 2004. doi: 10.1103/PhysRevLett.92.126603. URL https://link.aps.org/doi/10.1103/PhysRevLett.92.126603.

[29] Luqiao Liu, Takahiro Moriyama, D. C. Ralph, and R. A. Buhrman. Spin-torque ferromagnetic resonance induced by the spin hall effect. *Physical Review Letters*, 106

(3), 2011. ISSN 0031-9007. doi: 10.1103/PhysRevLett.106.036601. URL <Go to ISI>://WOS:000286739100010.

[30] Luqiao Liu, Chi-Feng Pai, Y. Li, H. W. Tseng, D. C. Ralph, and R. A. Buhrman. Spin-torque switching with the giant spin hall effect of tantalum. *Science*, 336 (6081):555–558, 2012. ISSN 0036-8075. doi: 10.1126/science.1218197. URL <Go to ISI>://WOS:000303498800037.

[31] Chi-Feng Pai, Luqiao Liu, Y. Li, H. W. Tseng, D. C. Ralph, and R. A. Buhrman. Spin transfer torque devices utilizing the giant spin hall effect of tungsten. *Applied Physics Letters*, 101(12):122404, 2012. doi: 10.1063/1.4753947.

[32] Yu A Bychkov and E I Rashba. Properties of a 2d electron gas with lifted spectral degeneracy. *JETP lett*, 39(2):78, 1984.

[33] Gustav Bihlmayer, O Rader, and R Winkler. Focus on the rashba effect. *New journal of physics*, 17(5):050202, 2015.

[34] Jorge Puebla, Florent Auvray, Mingran Xu, Bivas Rana, Antoine Albouy, Hanshen Tsai, Kouta Kondou, Gen Tatara, and Yoshichika Otani. Direct optical observation of spin accumulation at nonmagnetic metal/oxide interface. 111(9):092402, 2017. doi: 10.1063/1.4990113.

[35] S. Zhang, P. M. Levy, and A. Fert. Mechanisms of spin-polarized current-driven magnetization switching. *Phys. Rev. Lett.*, 88: 236601, May 2002. doi: 10.1103/PhysRevLett.88.236601. URL https://link.aps.org/doi/10.1103/PhysRevLett.88.236601.

[36] Tianxiang Nan, Satoru Emori, Carl T. Boone, Xinjun Wang, Trevor M. Oxholm, John G. Jones, Brandon M. Howe, Gail J. Brown, and Nian X. Sun. Comparison of spin-orbit torques and spin pumping across nife/pt and nife/cu/pt interfaces. *Phys. Rev. B*, 91:214416, Jun 2015. doi: 10.1103/PhysRevB.91.214416. URL https://link.aps.org/doi/10.1103/PhysRevB.91.214416.

[37] Yongxi Ou, Shengjie Shi, DC Ralph, and RA Buhrman. Strong spin hall effect in the antiferromagnet ptmn. *Physical Review B*, 93(22):220405, 2016.

[38] Arne Brataas, Andrew D Kent, and Hideo Ohno. Current-induced torques in magnetic materials. *Nature materials*, 11(5):372, 2012.

[39] Kotb Jabeur, Gregory Di Pendina, Fabrice Bernard-Granger, and Guillaume Prenat. Spin orbit torque non-volatile flip-flop for high speed and low energy applications. *IEEE electron device letters*, 35(3):408–410, 2014.

[40] John Kerr LL.D. Xliii. on rotation of the plane of polarization by reflection from the pole of a magnet. *The London, Edinburgh, and Dublin Philosophical Magazine and Journal of Science*, 3(19):321–343, 1877. doi: 10.1080/14786447708639245.

[41] Laura M. Roth. Theory of the faraday effect in solids. *Phys. Rev.*, 133:A542–A553, Jan 1964. doi: 10.1103/PhysRev.133.A542.

[42] Jana Hamrlová, Jaroslav Hamrle, Kamil Postava, and Jaromír Pištora. Quadratic-in-magnetization permittivity and conductivity tensor in cubic crystals. *physica status solidi (b)*, 250(10):2194–2205, 2013. ISSN 0370-1972. doi: 10.1002/pssb.201349031. URL `https://doi.org/10.1002/pssb.201349031`.

[43] Chun-Yeol You and Sung-Chul Shin. Generalized analytic formulae for magneto-optical kerr effects. *Journal of Applied Physics*, 84(1):541–546, 1998. doi: 10.1063/1.368058. URL `https://doi.org/10.1063/1.368058`.

[44] Tomoya Higo, Huiyuan Man, Daniel B Gopman, Liang Wu, Takashi Koretsune, Olaf MJ van't Erve, Yury P Kabanov, Dylan Rees, Yufan Li, Michi-To Suzuki, et al. Large magneto-optical kerr effect and imaging of magnetic octupole domains in an antiferromagnetic metal. *Nature photonics*, 12(2):73, 2018.

[45] J Hamrle, S Blomeier, O Gaier, B Hillebrands, H Schneider, G Jakob, K Postava, and C Felser. Huge quadratic magneto-optical kerr effect and magnetization reversal in the co2 fesi heusler compound. *Journal of Physics D: Applied Physics*, 40(6):1563, 2007.

[46] P K Muduli, W C Rice, L He, B A Collins, Y S Chu, and F Tsui. Study of magnetic anisotropy and magnetization reversal using the quadratic magnetooptical effect in epitaxial cox mny gez (111) films. *Journal of Physics: Condensed Matter*, 21(29): 296005, 2009.

[47] R. Clark Jones. A new calculus for the treatment of optical systems: Description and discussion of the calculus. *J. Opt. Soc. Am.*, 31(7):488–493, Jul 1941. doi: 10.1364/JOSA.31.000488.

[48] Peter J Kelly and R Derek Arnell. Magnetron sputtering: a review of recent developments and applications. *Vacuum*, 56(3):159–172, 2000.

[49] Denton Vaccum. Magnetron sputtering solutions. URL `https://www.dentonvacuum.com/products-technologies/magnetron-sputtering`.

[50] Tadatsugu Minami, Hidehito Nanto, and Shinzo Takata. Highly conductive and transparent aluminum doped zinc oxide thin films prepared by rf magnetron sputtering. *Japanese Journal of Applied Physics*, 23(5A):L280, 1984.

[51] Tadatsugu Minami, Hirotoshi Sato, Hidehito Nanto, and Shinzo Takata. Group iii impurity doped zinc oxide thin films prepared by rf magnetron sputtering. *Japanese journal of applied physics*, 24(10A):L781, 1985.

[52] DAH Hanaor, G Triani, and CC Sorrell. Morphology and photocatalytic activity of highly oriented mixed phase titanium dioxide thin films. *Surface and Coatings Technology*, 205(12):3658–3664, 2011.

[53] Wikipedia. Photolithography. .

[54] Product Data Sheet. Az 5214 e image reversal photoresist. *AZ Electronic Materials*, 70.

[55] Rabih Zaouk, Benjamin Y Park, and Marc J Madou. Introduction to microfabrication techniques. In *Microfluidic Techniques*, pages 5–15. Springer, 2006.

[56] INC. Ion Beam Milling. Ion milling process. URL http://www.ionbeammilling.com/about-the-ion-milling-process.

[57] FM Smits. Measurement of sheet resistivities with the four-point probe. *Bell System Technical Journal*, 37(3):711–718, 1958.

[58] NM Bashara. *Ellipsometry and polarized light*. North Holland, 1987.

[59] Hiroyuki Fujiwara. *Spectroscopic ellipsometry: principles and applications*. John Wiley Sons, 2007.

[60] Wikipedia. Ellipsometry. .

[61] Bertram Eugene Warren. *X-ray Diffraction*. Courier Corporation, 1990.

[62] John Brian Pendry. *Low energy electron diffraction*. Academic Press London, 1974.

[63] Wikipedia. X-ray diffraction. .

[64] Martin Weisheit, Sebastian Fähler, Alain Marty, Yves Souche, Christiane Poinsignon, and Dominique Givord. Electric field-induced modification of magnetism in thin-film ferromagnets. *Science*, 315(5810): 349–351, 2007. ISSN 0036-8075. doi: 10.1126/science.1136629. URL http://science.sciencemag.org/content/315/5810/349.

[65] Ying-Hao Chu, Lane W. Martin, Mikel B. Holcomb, Martin Gajek, Shu-Jen Han, Qing He, Nina Balke, Chan-Ho Yang, Donkoun Lee, Wei Hu, Qian Zhan, Pei-Ling Yang, Arantxa Fraile-Rodríguez, Andreas Scholl, Shan X. Wang, and R. Ramesh. Electric-field control of local ferromagnetism using a magnetoelectric multiferroic. *Nature Materials*, 7:478, 2008. doi: 10.1038/nmat2184. URL http://dx.doi.org/10.1038/nmat2184.

[66] T. Maruyama, Y. Shiota, T. Nozaki, K. Ohta, N. Toda, M. Mizuguchi, A. A. Tulapurkar, T. Shinjo, M. Shiraishi, S. Mizukami, Y. Ando, and Y. Suzuki. Large voltage-induced magnetic anisotropy change in a few atomic layers of iron. *Nature Nanotechnology*, 4:158, 2009. doi: 10.1038/nnano.2008.406. URL http://dx.doi.org/10.1038/nnano.2008.406.

[67] Satoru Emori, Uwe Bauer, Sung-Min Ahn, Eduardo Martinez, and Geoffrey S. D. Beach. Current-driven dynamics of chiral ferromagnetic domain walls. *Nature Materials*, 12(7):611–616, 2013. ISSN 1476-1122. doi: 10.1038/nmat3675. URL <Go to ISI>://WOS:000320720000015.

[68] Ioan Mihai Miron, Kevin Garello, Gilles Gaudin, Pierre-Jean Zermatten, Marius V. Costache, Stephane Auffret, Sebastien Bandiera, Bernard Rodmacq, Alain Schuhl, and Pietro Gambardella. Perpendicular switching of a single ferromagnetic layer induced by in-plane current injection. *Nature*, 476(7359):189–U88, 2011. ISSN 0028-0836. doi: 10.1038/nature10309. URL <Go to ISI>://WOS:000293731900032.

[69] Kwang-Su Ryu, Luc Thomas, See-Hun Yang, and Stuart Parkin. Chiral spin torque at magnetic domain walls. *Nature Nanotechnology*, 8(7):527–533, 2013. ISSN 1748-3387. doi: 10.1038/nnano.2013.102. URL <Go to ISI>://WOS:000321248700018.

[70] J. A. Katine and Eric E. Fullerton. Device implications of spin-transfer torques. *Journal of Magnetism and Magnetic Materials*, 320(7):1217–1226, 2008. ISSN 0304-8853. doi: https://doi.org/10.1016/j.jmmm.2007.12.013. URL http://www.sciencedirect.com/science/article/pii/S0304885307010189.

[71] Xin Fan, Jun Wu, Yunpeng Chen, Matthew J. Jerry, Huaiwu Zhang, and John Q. Xiao. Observation of the nonlocal spin-orbital effective field. *Nature Communications*, 4:1799, 2013. doi: 10.1038/ncomms2709. URL http://dx.doi.org/10.1038/ncomms2709.

[72] Junyeon Kim, Jaivardhan Sinha, Masamitsu Hayashi, Michihiko Yamanouchi, Shunsuke Fukami, Tetsuhiro Suzuki, Seiji Mitani, and Hideo Ohno. Layer thickness dependence of the current-induced effective field vector in ta—cofeb—mgo. *Nature Materials*, 12:240, 2012. doi: 10.1038/nmat3522. URL http://dx.doi.org/10.1038/nmat3522.

[73] Yabin Fan, Pramey Upadhyaya, Xufeng Kou, Murong Lang, So Takei, Zhenxing Wang, Jianshi Tang, Liang He, Li-Te Chang, Mohammad Montazeri, Guoqiang Yu, Wanjun Jiang, Tianxiao Nie, Robert N. Schwartz, Yaroslav Tserkovnyak, and Kang L. Wang. Magnetization switching through giant spin–orbit torque in a magnetically doped topological insulator heterostructure. *Nature Materials*, 13:699, 2014. doi: 10.1038/nmat3973. URL http://dx.doi.org/10.1038/nmat3973.

[74] A. R. Mellnik, J. S. Lee, A. Richardella, J. L. Grab, P. J. Mintun, M. H. Fischer, A. Vaezi, A. Manchon, E. A. Kim, N. Samarth, and D. C. Ralph. Spin-transfer torque generated by a topological insulator. *Nature*, 511:449, 2014. doi: 10.1038/nature13534. URL http://dx.doi.org/10.1038/nature13534.

[75] Kevin Garello, Ioan Mihai Miron, Can Onur Avci, Frank Freimuth, Yuriy Mokrousov, Stefan Blügel, Stéphane Auffret, Olivier Boulle, Gilles Gaudin, and Pietro Gambardella. Symmetry and magnitude of spin–orbit torques in ferromagnetic heterostructures. *Nature Nanotechnology*, 8:587, 2013. doi: 10.1038/nnano.2013.145. URL http://dx.doi.org/10.1038/nnano.2013.145.

[76] Can Onur Avci, Kevin Garello, Mihai Gabureac, Abhijit Ghosh, Andreas Fuhrer, Santos F. Alvarado, and Pietro Gambardella. Interplay of spin-orbit torque and thermoelectric effects in ferromagnet/normal-metal bilayers. *Physical Review B*, 90(22):224427, 2014. doi: 10.1103/PhysRevB.90.224427. URL https://link.aps.org/doi/10.1103/PhysRevB.90.224427.

[77] E. Saitoh, M. Ueda, H. Miyajima, and G. Tatara. Conversion of spin current into charge current at room temperature: Inverse spin-hall effect. *Applied Physics Letters*, 88(18):182509, 2006. ISSN 0003-6951. doi: 10.1063/1.2199473. URL https://doi.org/10.1063/1.2199473.

[78] Carlos Dehesa-Martínez, L. Blanco-Gutierrez, M. Vélez, J. Díaz, L. M. Alvarez-Prado, and J. M. Alameda. Magneto-optical transverse kerr effect in multilayers. *Physical Review B*, 64(2):024417, 2001. doi: 10.1103/PhysRevB.64.024417. URL https://link.aps.org/doi/10.1103/PhysRevB.64.024417.

[79] M. Buchmeier, R. Schreiber, D. E. Bürgler, and C. M. Schneider. Thickness dependence of linear and quadratic magneto-optical kerr effects in ultrathin fe(001) films. *Physical Review B*, 79(6):064402, 2009. doi: 10.1103/PhysRevB.79.064402. URL https://link.aps.org/doi/10.1103/PhysRevB.79.064402.

[80] R. M. Osgood Iii, S. D. Bader, B. M. Clemens, R. L. White, and H. Matsuyama. Second-order magneto-optic effects in anisotropic thin films. *Journal of Magnetism and Magnetic Materials*, 182(3):297–323, 1998. ISSN 0304-8853. doi: https://doi.org/10.1016/S0304-8853(97)01045-7. URL http://www.sciencedirect.com/science/article/pii/S0304885397010457.

[81] X. Fan, H. Celik, J. Wu, C. Y. Ni, K. J. Lee, V. O. Lorenz, and J. Q. Xiao. Quantifying interface and bulk contributions to spin-orbit torque in magnetic bilayers. *Nature Communications*, 5, 2014. ISSN 2041-1723. doi: 10.1038/ncomms4042. URL <Go to ISI>://WOS:000331083800025.

[82] Masamitsu Hayashi, Junyeon Kim, Michihiko Yamanouchi, and Hideo Ohno. Quantitative characterization of the spin-orbit torque using harmonic hall voltage measurements. *Physical Review B*, 89(14):144425, 2014. doi: 10.1103/PhysRevB.89.144425. URL https://link.aps.org/doi/10.1103/PhysRevB.89.144425.

[83] Christian Stamm, Christoph Murer, Marco Berritta, Junxiao Feng, Mihai Gabureac, Peter M Oppeneer, and Pietro Gambardella. Magneto-optical detection of the spin hall effect in pt and w thin films. *Physical review letters*, 119(8):087203, 2017.

[84] OMJ van 't Erve, AT Hanbicki, KM McCreary, CH Li, and BT Jonker. Optical detection of spin hall effect in metals. *Applied Physics Letters*, 104(17):172402, 2014.

[85] Patricia Riego, Saül Vélez, Juan M Gomez-Perez, Jon Ander Arregi, Luis E Hueso, Fèlix Casanova, and Andreas Berger. Absence of detectable current-induced magneto-optical kerr effects in pt, ta, and w. *Applied Physics Letters*, 109(17):172402, 2016.

[86] Yudan Su, Hua Wang, Jie Li, Chuanshan Tian, Ruqian Wu, Xiaofeng Jin, and YR Shen. Absence of detectable moke signals from spin hall effect in metals. *Applied Physics Letters*, 110(4):042401, 2017.

[87] Yang Liu, Jean Besbas, Yi Wang, Pan He, Mengji Chen, Dapeng Zhu, Yang Wu, Jong Min Lee, Lan Wang, Jisoo Moon, et al. Direct visualization of current induced spin accumulation in topological insulators. *arXiv preprint arXiv:1805.11382*, 2018.

[88] Paul Seifert, Kristina Vaklinova, Sergey Ganichev, Klaus Kern, Marko Burghard, and Alexander W Holleitner. Spin hall photoconductance in a three-dimensional topological insulator at room temperature. *Nature communications*, 9(1):331, 2018.

[89] Model SR830 Lock-in Amplifier and Product Manual. Stanford research systems. *Inc, Sunnyvale, USA*, 1993.

[90] Ya M Blanter and Markus Büttiker. Shot noise in mesoscopic conductors. *Physics reports*, 336(1-2):1–166, 2000.

[91] Newport Co. Nirvana model 2007. URL `https://www.newport.com/p/2007`.

[92] Y. K. Kato, R. C. Myers, A. C. Gossard, and D. D. Awschalom. Observation of the spin hall effect in semiconductors. *Science*, 306(5703):1910–1913, 2004. ISSN 0036-8075. doi: 10.1126/science.1105514. URL `<Go to ISI>://WOS:000225695600036`.

[93] T. Kimura, Y. Otani, T. Sato, S. Takahashi, and S. Maekawa. Room-temperature reversible spin hall effect. *Physical Review Letters*, 98(15), 2007. ISSN 0031-9007. doi: 10.1103/PhysRevLett.98.156601. URL `<Go to ISI>://WOS:000245691400047`.

[94] W. J. Jiang, P. Upadhyaya, W. Zhang, G. Q. Yu, M. B. Jungfleisch, F. Y. Fradin, J. E. Pearson, Y. Tserkovnyak, K. L. Wang, O. Heinonen, S. G. E. te Velthuis, and A. Hoffmann. Blowing magnetic skyrmion bubbles. *Science*, 349(6245): 283–286, 2015. ISSN 0036-8075. doi: 10.1126/science.aaa1442. URL `<Go to ISI>://WOS:000358218600045`.

[95] S. F. Zhang. Spin hall effect in the presence of spin diffusion. *Physical Review Letters*, 85(2):393–396, 2000. ISSN 0031-9007. doi: 10.1103/PhysRevLett.85.393. URL `<Go to ISI>://WOS:000088048700042`.

[96] E. H. Hall. On the "rotational coefficient" in nickel and cobalt. *Proc. Phys. Soc. London*, 4:325, 1880.

[97] N. Nagaosa, J. Sinova, S. Onoda, A. H. MacDonald, and N. P. Ong. Anomalous hall effect. *Reviews of Modern Physics*, 82(2):1539–1592, 2010. ISSN 0034-6861. doi: 10.1103/RevModPhys.82.1539. URL `<Go to ISI>://WOS:000278228900001`.

[98] B. F. Miao, S. Y. Huang, D. Qu, and C. L. Chien. Inverse spin hall effect in a ferromagnetic metal. *Phys. Rev. Lett.*, 111:066602, Aug 2013. doi: 10.1103/PhysRevLett.111.066602.

[99] D. C. Ralph and M. D. Stiles. Spin transfer torques. *Journal of Magnetism and Magnetic Materials*, 320(7):1190–1216, 2008. ISSN 0304-8853. doi: 10.1016/j.jmmm.2007.12.019. URL `<Go to ISI>://WOS:000254418600001`.

[100] A. Chernyshov, M. Overby, X. Y. Liu, J. K. Furdyna, Y. Lyanda-Geller, and L. P. Rokhinson. Evidence for reversible control of magnetization in a ferromagnetic material by means of spin-orbit magnetic field. *Nature Physics*, 5(9):656–659, 2009. ISSN 1745-2473. doi: 10.1038/nphys1362. URL <Go to ISI>://WOS:000270095600017.

[101] C. Ciccarelli, L. Anderson, V. Tshitoyan, A. J. Ferguson, F. Gerhard, C. Gould, L. W. Molenkamp, J. Gayles, J. Zelezny, L. Smejkal, Z. Yuan, J. Sinova, F. Freimuth, and T. Jungwirth. Room-temperature spin-orbit torque in nimnsb. *Nature Physics*, 12(9):855–860, 2016. ISSN 1745-2473. doi: 10.1038/nphys3772. URL <Go to ISI>://WOS:000383219800013.

[102] A. F. Chalmers. Curie's principle. *British Journal for the Philosophy of Science*, 21 (2):133–148, 1970.

[103] P. A. M. Dirac. On the theory of quantum mechanics. *Proceedings of the Royal Society of London. Series A, Containing Papers of a Mathematical and Physical Character*, 112 (762):661–677, 1926. ISSN 09501207. URL http://www.jstor.org/stable/94692.

[104] Z. Q. Qiu and S. D. Bader. Surface magneto-optic kerr effect. *Review of Scientific Instruments*, 71(3):1243–1255, 2000. ISSN 0034-6748. doi: 10.1063/1.1150496. URL <Go to ISI>://WOS:000085688600001.

[105] Xin Fan, Alex R. Mellnik, Wenrui Wang, Neal Reynolds, Tao Wang, Halise Celik, Virginia Lorenz, Daniel C. Ralph, and John Q. Xiao. All-optical vector measurement of spin-orbit-induced torques using both polar and quadratic magneto-optic kerr effects. *Applied Physics Letters*, 109, 2016.

[106] L. Q. Liu, T. Moriyama, D. C. Ralph, and R. A. Buhrman. Spin-torque ferromagnetic resonance induced by the spin hall effect. *Physical Review Letters*, 106 (3), 2011. ISSN 0031-9007. doi: 10.1103/PhysRevLett.106.036601. URL <Go to ISI>://WOS:000286739100010.

[107] D. A. Pesin and A. H. MacDonald. Quantum kinetic theory of current-induced torques in rashba ferromagnets. *Physical Review B*, 86(1), 2012. ISSN 1098-0121. doi: 10.1103/PhysRevB.86.014416. URL <Go to ISI>://WOS:000306468000001.

[108] X. H. Wang and A. Manchon. Diffusive spin dynamics in ferromagnetic thin films with a rashba interaction. *Physical Review Letters*, 108(11), 2012. ISSN 0031-9007. doi: 10.1103/PhysRevLett.108.117201. URL <Go to ISI>://WOS:000301411300014.

[109] H. Kurebayashi, J. Sinova, D. Fang, A. C. Irvine, T. D. Skinner, J. Wunderlich, V. Novak, R. P. Campion, B. L. Gallagher, E. K. Vehstedt, L. P. Zarbo, K. Vyborny, A. J. Ferguson, and T. Jungwirth. An antidamping spin-orbit torque originating from the berry curvature. *Nature Nanotechnology*, 9(3):211–217, 2014. ISSN 1748-3387. doi: 10.1038/nnano.2014.15. URL <Go to ISI>://WOS:000332637200015.

[110] S. H. C. Baek, V. P. Amin, Y. W. Oh, G. Go, S. J. Lee, G. H. Lee, K. J. Kim, M. D. Stiles, B. G. Park, and K. J. Lee. Spin currents and spin-orbit torques in ferromagnetic trilayers. *Nature Materials*, 17(6):509–+, 2018. ISSN 1476-1122. doi: 10.1038/s41563-018-0041-5. URL <Go to ISI>://WOS:000432928300014.

[111] X. J. Wang, J. R. Yates, I. Souza, and D. Vanderbilt. Ab initio calculation of the anomalous hall conductivity by wannier interpolation. *Physical Review B*, 74 (19), 2006. ISSN 1098-0121. doi: 10.1103/PhysRevB.74.195118. URL <Go to ISI>://WOS:000242409200055.

[112] al Paolo Giannozzi, et. Quantum espresso: a modular and open-source software project for quantum simulations of materials. *Journal of Physics: Condensed Matter*, 21(39): 395502, 2009. URL http://stacks.iop.org/0953-8984/21/i=39/a=395502.

[113] Huei-Ru Fuh and Guang-Yu Guo. Intrinsic anomalous hall effect in nickel: A gga + u study. *Phys. Rev. B*, 84:144427, Oct 2011. doi: 10.1103/PhysRevB.84.144427. URL https://link.aps.org/doi/10.1103/PhysRevB.84.144427.

[114] Arash A. Mostofi, Jonathan R. Yates, Young-Su Lee, Ivo Souza, David Vanderbilt, and Nicola Marzari. wannier90: A tool for obtaining maximally-localised wannier functions. *Computer Physics Communications*, 178(9):685 – 699, 2008. ISSN 0010-4655. doi: https://doi.org/10.1016/j.cpc.2007.11.016. URL http://www.sciencedirect.com/science/article/pii/S0010465507004936.

[115] Axel Hoffmann. Spin hall effects in metals. *Ieee Transactions on Magnetics*, 49(10): 5172–5193, 2013. ISSN 0018-9464. doi: 10.1109/tmag.2013.2262947. URL <Go to ISI>://WOS:000324930200001.

[116] D. Tian, Y. F. Li, D. Qu, S. Y. Huang, X. F. Jin, and C. L. Chien. Manipulation of pure spin current in ferromagnetic metals independent of magnetization. *Physical Review B*, 94(2), 2016. ISSN 2469-9950. doi: 10.1103/PhysRevB.94.020403. URL <Go to ISI>://WOS:000379701700002.

[117] K. S. Das, W. Y. Schoemaker, B. J. van Wees, and I. J. Vera-Marun. Spin injection and detection via the anomalous spin hall effect of a ferromagnetic metal. *Physical Review B*, 96(22), 2017. ISSN 2469-9950. doi: 10.1103/PhysRevB.96.220408. URL <Go to ISI>://WOS:000418572700004.

[118] A. M. Humphries, T. Wang, E. R. J. Edwards, S. R. Allen, J. M. Shaw, H. T. Nembach, J. Q. Xiao, T. J. Silva, and X. Fan. Observation of spin-orbit effects with spin rotation symmetry. *Nature Communications*, 8, 2017. ISSN 2041-1723. doi: 10.1038/s41467-017-00967-w. URL <Go to ISI>://WOS:000412871300007.

[119] Wei Zhang, Matthias B. Jungfleisch, Wanjun Jiang, John E. Pearson, Axel Hoffmann, Frank Freimuth, and Yuriy Mokrousov. Spin hall effects in metallic antiferromagnets. *Phys. Rev. Lett.*, 113:196602, Nov 2014. doi: 10.1103/PhysRevLett.113.196602.

[120] Anthony Gerrard and James M Burch. *Introduction to matrix methods in optics*. Courier Corporation, 1994.

Appendix A

Jones Calculus Derivations

A.1 Overview of Jones Calculus

The polarization of light, which is fundamentally a transverse electromagnetic wave, is defined based on the electric field components of the light. Therefore, in Jones calculus, polarization states are expressed by electric field vectors:

$$\boldsymbol{E} = \begin{pmatrix} E_{0x}\exp(i\phi_x) \\ E_{0y}\exp(i\phi_y) \end{pmatrix} = \begin{pmatrix} E_{0x} \\ E_{0y}\exp(-i\phi) \end{pmatrix} \exp(i\phi_x), \tag{A.1}$$

where E is the complex electric field vector, E_{0x} and E_{0y} are the amplitudes of the electric field in x- and y-directions, and ϕ_x and ϕ_y contain the phase information. The light described by Eq. A.1 is propagating in the z-direction. The phase difference between the two components, $\phi = \phi_x - \phi_y$, determines the nature of the polarization state. For instance, if there is no phase difference between the two components, $\phi = 0$, the polarization state is linear. However, if the phase difference is 180 degrees ($\phi = \frac{\pi}{2}$), the resultant polarization state is circular. All the other phase differences result in elliptical polarization states.

Some typical polarization states are listed below:

$$\text{Linear Horizontal Polarization (LHP)} : \begin{pmatrix} 1 \\ 0 \end{pmatrix},$$

$$\text{Linear Vertical Polarization (LVP)} : \begin{pmatrix} 0 \\ 1 \end{pmatrix},$$

$$\text{Linear Polarization at 45 degrees (L45P)} : \frac{\sqrt{2}}{2}\begin{pmatrix} 1 \\ 1 \end{pmatrix},$$

$$\text{Left Circular Polarization (LCP)} : \frac{\sqrt{2}}{2}\begin{pmatrix} 1 \\ -i \end{pmatrix},$$

$$\text{Right Circular Polarization (RCP)} : \frac{\sqrt{2}}{2}\begin{pmatrix} 1 \\ i \end{pmatrix}.$$

For simplification, the intensity of the light $|\boldsymbol{E}|^2$ is normalized to 1. The superposition of two beams can be calculated by directly adding the Jones vectors together. For example, we know linear polarization can be decomposed into a combination of LCP and RCP. This relation can be demonstrated with Jones vectors:

$$\frac{\sqrt{2}}{2}\begin{pmatrix} 1 \\ i \end{pmatrix} + \frac{\sqrt{2}}{2}\begin{pmatrix} 1 \\ -i \end{pmatrix} = \sqrt{2}\begin{pmatrix} 1 \\ 0 \end{pmatrix}. \tag{A.2}$$

The effect of linear optical elements on a given polarization state is addressed by applying 2×2 Jones matrix operators to the Jones vectors, $P' = M_n \cdots M_1 \cdot P$. Common optics, such as mirrors, polarizers, wave-plates, beam-splitters, electro-optic modulators and even magnetic thin films, can all be expressed in the form of matrices. For the MOKE calculations in this dissertation, polarizer and half/quarter-wave-plate are most frequently used. A linear polarier can be generalized as [120]

$$M_{\text{Pol}} = \begin{pmatrix} p_x & 0 \\ 0 & P_y \end{pmatrix}, 0 \geq p_x, p_y \leq 1, \tag{A.3}$$

where the relative amplitudes of p_x and p_y depend on the angle between the polarizer axis

and the x-direction. For example, the Jones matrix for a linear polarizer with axis parallel to x- and y-direction can be written as [120]

$$M_x = \begin{pmatrix} 1 & 0 \\ 0 & 0 \end{pmatrix}, M_y = \begin{pmatrix} 0 & 0 \\ 0 & 1 \end{pmatrix}. \tag{A.4}$$

Wave-plates, on the other hand, are phase retarders. In the simplest situation, in which the fast- and slow-axis of the wave plate is aligned with x- and y-direction, respectively, the Jones matrix for such a wave plate (WP) can be expressed as [120]

$$M_{\mathrm{WP}} = \begin{pmatrix} 1 & 0 \\ 0 & e^{i\phi} \end{pmatrix}, \tag{A.5}$$

where ϕ is the phase delay between the fast- and slow-axis of the wave plate. As an example, half-wave-plates (HWP) have $\phi = \pi$ and quarter-wave-plates (QWP) have $\phi = \frac{\pi}{2}$, leading to the Jones matrices for half- and quarter-wave-plate as [120]

$$M_{\mathrm{HWP}} = \begin{pmatrix} 1 & 0 \\ 0 & -1 \end{pmatrix}, M_{\mathrm{QWP}} = \begin{pmatrix} 1 & 0 \\ 0 & -i \end{pmatrix}. \tag{A.6}$$

In addition, for more general situations, where the principle axis of an optical element is at an angle θ with respect to the x-direction, the corresponding Jones matrix is calculated by applying the rotation operator matrix, $R(\theta) = \begin{pmatrix} \cos\theta & \sin\theta \\ -\sin\theta & \cos\theta \end{pmatrix}$, to the special matrices shown in Eq. A.4 and A.6. For instance, the Jones matrix for a half-wave-plate with its fast axis at θ degree is calculated as

$$M_{\mathrm{HWP}}(\theta) = R(-\theta) M_{\mathrm{HWP}} R(\theta) = \begin{pmatrix} \cos 2\theta & \sin 2\theta \\ \sin 2\theta & -\cos 2\theta \end{pmatrix}. \tag{A.7}$$

Lastly, Jones matrix containing polar and quadratic MOKE information for a magnetic

sample can be written as

$$\textbf{Magnetic Sample}: M_{\text{Sample}} = \xi \begin{bmatrix} 1 + \frac{\beta_{\text{Quadratic}}}{2} & -\alpha_{\text{Polar}} m_z \\ \alpha_{\text{Polar}} m_z & 1 + \frac{\beta_{\text{Quadratic}}}{2} \end{bmatrix}.$$

Factor ξ captures the reflection loss, which does not affect the polarization change. M_{Sample} is derived based on the fact that polar MOKE is only sensitive to the out-of-plane magnetization component and Quadratic MOKE yields no polarization change when the polarization direction is in parallel or perpendicular to the in-plane magnetization directions.

By applying the vectors/matrices discussed above, the polarization states at each point of a linear optical system can be calculated.

A.2 Derivation of MOKE Signal for Circular Polarization

In this section, I use Jones calculus to derive Eq. 3.6 in Chap. 3. Following the Jones matrix formalism presented in Appendix.A1, for incident light with circular polarization, the polarization states at each stage in Fig. 3.4 can be calculated as (see Fig. A.1 for an illustration of the polarization at each stage)

$$(1): P_1 = \begin{bmatrix} 1 \\ 0 \end{bmatrix},$$

$$(2): P_2 = R[\phi_{\pi/4}] M_{\text{QW}} R[-\phi_{\pi/4}] P_1 = \frac{1-i}{2} \begin{bmatrix} 1 \\ i \end{bmatrix},$$

$$(3): P_3 = R[\phi_M] M_{\text{Sample}} R[-\phi_M] P_2 =$$

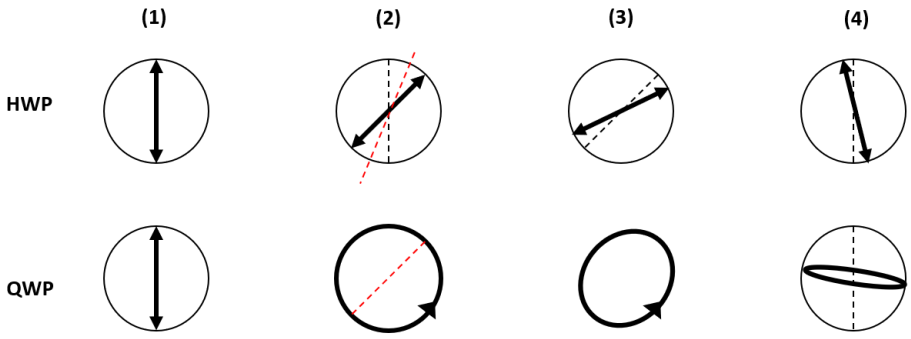

Figure A.1: Illustration of the light polarization state at each stage in Fig. 3.4. Red dashed line indicates the fast axis direction of the wave plates.

$$\frac{1-i}{2}\xi\left\{(1-i\alpha_{\text{Polar}}m_z)\begin{bmatrix}1\\ i\end{bmatrix}+\frac{\beta_{\text{Quadratic}}(\cos\phi_M+i\sin\phi_M)^2}{2}\begin{bmatrix}1\\ -i\end{bmatrix}\right\},$$

$$(4): P_4 = R[\phi_{\pi/4}]M_{\text{QW}}R[-\phi_{\pi/4}]P_3 = \xi\left\{\begin{bmatrix}0\\ 1\end{bmatrix}+\begin{bmatrix}\beta_{\text{Quadratic}}\frac{\sin 2\phi_M - i\cos 2\phi_M}{2}\\ i\alpha_{\text{Polar}}m_z\end{bmatrix}\right\}.$$

Thus, the total polarization change is $\frac{\pi}{2}-\beta_{\text{Quadratic}}\frac{\sin 2\phi_M - i\cos 2\phi_M}{2}$. Differentiating this expression near $\phi_M = 0$ gives Eq. 3.6.

A.3 Derivation of MOKE Signal for Linear Polarization

In this section, I use Jones calculus to derive Eq. 3.7 in Chap. 3. Using the same procedures as in the previous section, for light with linear polarization, the polarization at each stage in Fig. 3.4 cane be calculated as (see Fig. A.1 for an illustration of the polarization at each stage)

$$(1) : P_1 = \begin{bmatrix} 1 \\ 0 \end{bmatrix},$$

$$(2) : P_2 = R[\phi_{\mathrm{HW}}] M_{\mathrm{HW}} R[-\phi_{\mathrm{HW}}] P_1 = \begin{bmatrix} \cos 2\phi_{\mathrm{HW}} \\ \sin 2\phi_{\mathrm{HW}} \end{bmatrix},$$

$$(3) : P_3 = R[\phi_{\mathrm{M}}] M_{\mathrm{Sample}} R[-\phi_{\mathrm{M}}] P_2 =$$

$$\xi \left\{ \begin{bmatrix} \cos 2\phi_{\mathrm{HW}} \\ \sin 2\phi_{\mathrm{HW}} \end{bmatrix} + \alpha_{\mathrm{Polar}} m_z \begin{bmatrix} -\sin(2\phi_{\mathrm{HW}}) \\ \cos 2\phi_{\mathrm{HW}} \end{bmatrix} + \frac{\beta_{\mathrm{Quadratic}}}{2} \begin{bmatrix} \cos(2\phi_M - 2\phi_{\mathrm{HW}}) \\ \sin(2\phi_M - 2\phi_{\mathrm{HW}}) \end{bmatrix} \right\},$$

$$(4) : P_4 = R[\phi_{\mathrm{HW}}] M_{\mathrm{HW}} R[-\phi_{\mathrm{HW}}] P_3 =$$

$$\xi \left\{ \begin{bmatrix} 1 \\ 0 \end{bmatrix} + \begin{bmatrix} \frac{\beta_{\mathrm{Quadratic}}}{2} \cos(4\phi_{\mathrm{HW}} - 2\phi_M) \\ -\alpha_{\mathrm{Polar}} m_z + \frac{\beta_{\mathrm{Quadratic}}}{2} \sin(4\phi_{\mathrm{HW}} - 2\phi_M) \end{bmatrix} \right\},$$

where $\phi_{\mathrm{HW}} = \frac{1}{2}\phi_{\mathrm{pol}}$ is the angle between x-direction and the principle axis of the half-wave-plate. Therefore, the total polarization rotation is $-\alpha_{\mathrm{Polar}} m_z + \frac{\beta_{\mathrm{Quadratic}}}{2} \sin(4\phi_{\mathrm{HW}} - 2\phi_M)$. By differentiating this angle rotation near $\phi_M = 0$, we get Eq. 3.7.

A.4 Derivation of MOKE Signal for the Magnetometer Setup

As discussed in Chap.3, the light polarization change due to polar and/or quadratic MOKE can be measured with the lock-in balanced detection technique shown in Fig. 3.4. For the real part of the polarization change, Kerr rotation, a half-wave-plate is used before the Wollaston prism. The half-wave-plate is set to 22.5° so that the s- and p-components of the polarization are initially balanced. Assume the Kerr rotation from polar and/or quadratic

MOKE is θ_K, the balanced detector output can be derived as (indices in this derivation indicate the steps as shown in Fig. A.2):

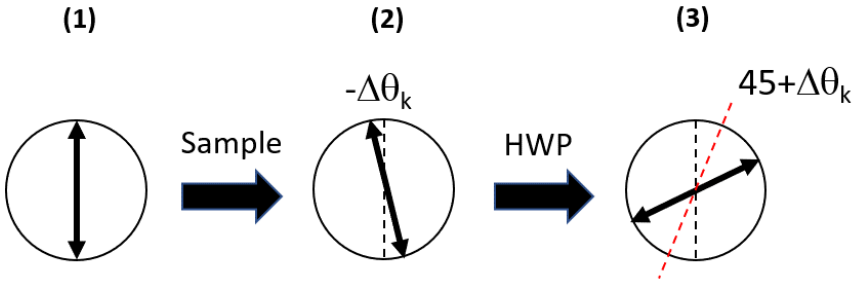

Figure A.2: Illustration of the light polarization state at each stage through the optical bridge system. Red dashed line indicates the fast axis of the wave-plates, which is at 22.5 degrees.

$$(1) : P_1 = \begin{bmatrix} 1 \\ 0 \end{bmatrix},$$

$$(2) : P_2 = \begin{bmatrix} \cos\Delta\theta_K \\ \sin\Delta\theta_K \end{bmatrix},$$

$$(3) : P_3 = \begin{bmatrix} \cos(45^\circ + \Delta\theta_K) \\ -\sin(45^\circ + \Delta\theta_K) \end{bmatrix}.$$

Since the balanced detector measures the optical power difference between the two components. Under first-order approximation, we have

$$V_{\text{lockin}} \propto |\cos(45^\circ + \Delta\theta_K)|^2 - |-\sin(45^\circ + \Delta\theta_K)|^2 = \cos(2\Delta\theta^K + 90^\circ) = \sin 2\Delta\theta_K \simeq 2\Delta\theta_K.$$

Therefore, if the DC output from one of the ports on the balanced detector is V_{DC} and the ratio of the AC and DC gain factors of the balanced detector is G, the Kerr rotation change $\Delta\theta_K$ can be calculated with

$$\Delta\theta_K = \frac{V_{\text{lockin}}}{4GV_{\text{DC}}}. \tag{A.8}$$

On the other hand, the imaginary part of the MOKE signal, Kerr ellipticity, can be measured with an additional quarter-wave-plate in front of the half-wave-plate and the Wollaston prism. The principle is easy to understand. When the fast axis of the quarter wave plate is parallel to the incoming nearly-linear polarization direction, it transfers the imaginary part of the polarization change into a real part. Therefore, it can then be measured by the above-discussed system.

Appendix B

MATLAB Code for Simulations

B.1 Signal-to-Noise Enhancement for Imperfect Linear Polarization

In this section, I attach the MATLAB code used to generate the modified S/N enhancement simulation curve in Fig. 4.7:

```
clear all

theta_K = 1e-6; %Kerr rotation due to sample
PtoS = 18; %Extinction ratio (field ratio)

%determine the strength of S and P components
b = sqrt( 1 / (1 + PtoS^2) );
a = sqrt(1 - b^2);

Ini = [1i*b;a]; %initial state of polarzation
SAM = [cos(theta_K) sin(theta_K); -sin(theta_K) cos(theta_K)]; %
    Jone matrix of the sample
i = 1;

for A = 1:0.1:100
```

```
15
16      sin2theta(i) = sqrt( (1/(2*A)-b^2) / (a^2-b^2) );
17      cos2theta(i) = sqrt(1 - sin2theta(i)^2);
18      B(i) = 1 / (2*A*(a^2*cos2theta(i)^2 + b^2*sin2theta(i)^2)); %
            attenuation factor due to the ND filter
19
20      WP = [cos2theta(i) sin2theta(i); sin2theta(i) -cos2theta(i)];
            % half-wave-plate
21
22      %calculate the resulting Jones vector
23      Output_Pol = WP*SAM*Ini;
24
25      %calculate the balanced detector output
26      output(i) = abs(sqrt(A) * Output_Pol(1))^2 - abs(sqrt(A) *
            sqrt(B(i)) * Output_Pol(2))^2;
27
28      i = i + 1;
29  end
30
31  %% Ploting Section
32  AA=1:0.1:100;
33
34  Experimental_A = [1, 4, 9, 16, 25, 36, 49, 64, 81, 100]; %
        experiemental thickness points
35  Amplification = [1, 1.39, 1.96, 2.48, 2.92, 3.35, 3.64, 3.75,
        3.80, 3.72];
36
```

```
data = [AA; output/output(1)];
fileID = fopen('Polarization Imperfection Simulation.txt','w');
fprintf(fileID, '%f %e\n',data);
fclose(fileID);

%data2 = [TT/1e-9; imag(Phi_S')*1e6];
%fileID2 = fopen('thickness calibration ellipticity.txt','w');
%fprintf(fileID2, '%f %e\n',data2);
%fclose(fileID2);

figure(1)
plot(sqrt(AA),output/(output(1)),'-r','linewidth',4);
hold on
scatter(sqrt(Experimental_A), Amplification, 'b', 'linewidth', 4);
xlabel('Incident power amplification');
ylabel('Enhancement');
title('Power enhancement A vs. signal enhancement');
%axis([1 10 0 45])
```

B.2 ASOT- and Calibration-Field-Induced Magnetization Distribution and MOKE Response

In this section, I summarize the MATLAB code that I used for the simulations in Chap. 5. First of all, "GetMagDist$_2$" function is used to generate the ASOT-induced magnetization distribution shown in Fig. 5.5. The "MOKE$_\mathrm{M}$Lmodel$_\mathrm{S}$UB3" function can take in a random magnetization distribution and calculate the corresponding MOKE response. There-

fore, I got the ASOT-induced MOKE response by applying the "$\text{MOKE}_{\text{M}}\text{Lmodel}_{\text{S}}\text{UB3}$" function to the previous calculated ASOT-induced magnetization distribution. Similarly, the MOKE response due to a uniform calibration field was calculated by applying the "$\text{MOKE}_{\text{M}}\text{Lmodel}_{\text{S}}\text{UB3}$" function to an uniformly-tilted magnetization distribution.

B.2.1 ASOT-Induced Magnetization Distribution

Fig. 5.5 is produced by "GetMagDist_2" function:

```
%Input the ASOT at the top and bottom surfaces; output the ASOT-induced magnetization distribution in a singal-layer FM
function m1 = GetMagDist_2(H_ex, M_s, H_a, n, a, J_ex, tau_T, tau_B, mu)

M_eff = M_s - H_a; %Calculate the effective field from demagnetizaztion and surface anisotropy

% construct the matrix
A_ii = (H_ex + M_s)*mu*a*M_s + 2*J_ex; %create the diagonal element (Inside layers are not affected by the surface anisotropy)
Diag = linspace(A_ii, A_ii, n); %create the vector for matrix diagonal
subDiag_1 = linspace(-J_ex, -J_ex, n-1);%create the subdiagonal vectors
subDiag_2 = linspace(-J_ex, -J_ex, n-1);

%Calculate the effective field caused by spin current
```

```
for i = 1:1:n
    tau(i) = 0; %Calculate the spin current loss in each layers (
        total n layers, compared to n+1 interfaces)
    %dJs_z(i) = Js_z(i)-Js_z(i+1);
end
tau(1) = tau_T;
tau(n) = tau_B;

M = diag(Diag) + diag(subDiag_1, 1) + diag(subDiag_2, -1); %
    construct the Matrix in euqation 5
M(1,1) = (H_ex + M_eff)*mu*a*M_s + J_ex;
M(n,n) = (H_ex + M_eff)*mu*a*M_s + J_ex;
% calculate magnetization distribution
m1 = M\tau.';
```

B.2.2 MOKE Response of a certain Magnetization Distribution

"MOKE$_{\mathrm{M}}$Lmodel$_{\mathrm{S}}$UB3" function:

```
% Input a magnetization distribution and calculates polar complex
    Kerr angle (incident angle is 0 degree)
% Uses formalism in 1998_You_JAP

function [Reflectance, Phi_S, Phi_P] = MOKE_MLmodel_SUB3(lambda,h,
    n,Q,mz)


```

```
Af = [1                                    0                                    1
                                                                    0;...
     0                                     1                                    0
                                                                    -1;...
     -1i*n(end)*Q(end)*mz(end)/2    -n(end)                    1i*n(end)
        *Q(end)*mz(end)/2           -n(end);...
     n(end)                         1i*n(end)*Q(end)*mz(end)/2  -n(end
        )                           1i*n(end)*Q(end)*mz(end)/2]; %The
        substrate's boundary matrix

Told = Af;%Put the substrate's the matrix as the last term

for j = length(mz)-1:-1:2 %calculate the boundary matices for
   magnetic layers (total is n-2 layers)
    A = [1                                 0                                1
                                                                0;...
         0                                 1                                0
                                                                -1;...
         -1i*n(j)*Q(j)*mz(j)/2             -n(j)                    1i*n(j)*
            Q(j)*mz(j)/2                   -n(j);...
         n(j)                              1i*n(j)*Q(j)*mz(j)/2     -n(j)
                                           1i*n(j)*Q(j)*mz(j)/2];

    U = exp(-1i*2*pi/lambda*n(j)*h(j));
    deltai = -pi*n(j)*Q(j)*h(j)*mz(j)/lambda;
    deltar = deltai;  %identical

```

```
24      D = [U*cos(deltai)    U*sin(deltai)   0                  0;...
25           -U*sin(deltai)   U*cos(deltai)   0                  0;...
26           0                0               cos(deltar)/U      sin(deltar)
                 /U;...
27           0                0               -sin(deltar)/U     cos(deltar
                 )/U];
28
29      Tnew = A*D*A^(-1)*Told; %multiply one layer per iteration
30      Told = Tnew;
31  end
32
33  j = 1;
34  Ai = [1                                  0                          1
                                          0;...
35        0                                  1                          0
                                                -1;...
36       -1i*n(j)*Q(j)*mz(j)/2               -n(j)                      1i*n(j)*Q
            (j)*mz(j)/2                          -n(j);...
37        n(j)                          1i*n(j)*Q(j)*mz(j)/2          -n(j)
                                  1i*n(j)*Q(j)*mz(j)/2];%Calculate the
             boundary matrix of air
38
39  T = Ai^(-1)*Told;
40
41  G = [T(1,1) T(1,2); T(2,1) T(2,2)];
42  I = [T(3,1) T(3,2); T(4,1) T(4,2)];
43
```

```
R = I/G;

Reflectance = abs(R(1,1))^2 + abs(R(2,1))^2;
Phi_S = R(2,1)/R(1,1);
Phi_P = R(1,2)/R(2,2);
```

B.2.3 ASOT-Induced MOKE Response

Code used to generate the fitting curves in Fig. 5.9(b):

```
% Calculate ASOT-induced MOKE response of a singal layer FM

clear all

% Define all the parameters and constant
%Parameters for step one
tau_T = -1.8e-6; %ASOT at the top surface (J/(m^2))
tau_B = -tau_T; %ASOT at the bottom surface (J/(m^2))
J_e = 1e+11; %charge current density  (A/m^2)
%sigma = 9.43e+6; %electrical conductivity (S/m) Pt
l_ex = 4e-9; %exchange length, due to exchange coupling, approx 4
    nm; (m)
a = 4e-10; %lattice constant--thickness of each sublayer (m)

mu = 4*pi*1e-7; %permeability (N/A^2)
h_bar = 1.0546e-34; %planck constant (J*s)
e = 1.6e-19; % electron charge (C)
```

```
17 M_s = 1.09/mu; %saturation magnetization (A/m) (from mu*Ms = 1.09T
       )
18 H_a = 79.77*27074/2/(a/1e-9); %surface anisotropy effective field
       (A/m)
19 J_ex = 0.64*2*19.1e-12/a; %interlayer exchange strength (J/m^2)
       %0.64 is from the scaling of thickness factor 0.8
20
21 %Parameters for MOKE response calculation
22 lambda = 780e-9;  % wavelength (m)
23 refrac_layer = 2.38+1i*4.36; %refractive index of the FM layer(for
        Py,2.2+1i*4.2) (14.78nm penetration depth)
24 refrac_Si = 3.7+1i*0.008; %refractive index of the substrate (Si)
       3.7+1i*0.007
25 refrac_SiO2 = 1.47+1i*0.0; %refractive index of the oxidation (
       SiO2) 1.47+1i*0
26 refrac_Pt = 2.73+1i*6.04; %refractive index of the (Pt)
27 refrac_Cu = 0.153 + 1i*4.84; %refractive index of copper 0.153 + 1
       i*4.84
28 Q_FM = 0.0036-1i*0.011; % magneto-optic coefficient of Co (0.043+1
       i*0.007)
29 T_max = 60e-9; %The maximum thickness of the simulation (m)
30
31
32 i = 1;
33 Reflectance = zeros(round(T_max/a),1);
34 Phi_S = zeros(round(T_max/a),1);
35 Phi_P = zeros(round(T_max/a),1);
```

```
36 for T = a: a: T_max %FM layer total thickness in (m)
37
38 n = round(T/a); %iteration number (number of sublayers, not the
       number of interfaces)
39
40 % Calculate ASOT-induced magnetization distribution
41
42 m1 = GetMagDist_2(H_ex, M_s, H_a, n, a, J_ex, tau_T, tau_B, mu); %
       m1 is the magnetization tilt caused by the ASOT
43
44 % sample layer (first is air, last is substrate, thickness of both
        do not matter)
45 refrac_temp = linspace(refrac_layer, refrac_layer, n); % Make a
       refractive index vector for all the sublayers
46 refrac = [1  refrac_temp  refrac_SiO2  refrac_Si]; % Construct
       the total refractive index vector
47 Q_temp = linspace(Q_FM, Q_FM, n); % Make a Q vector for all the
       sublayers
48 Q = [0  Q_temp  0  0]; % Construct the total magneto-optical
       constants vector
49 h_temp = linspace(a, a, n); % Make a thickness vector for all the
       sublayers
50 h = [inf  h_temp  1.0e-6  inf]; % Construct the overall thickness
        vector
51 mz = [0  m1'  0  0]; % Construct the overall magnetization vector
       in z-direction
52
```

```
53
54 [Reflectance(i), Phi_S(i), Phi_P(i)] = MOKE_MLmodel_SUB3(lambda, h
       , refrac, Q, mz); %Calculate the MOKE response for one
       thickness
55
56
57 i = i + 1;
58
59 end
60
61 SHA = 2*e*tau_T/(h_bar*J_e); %Calculate spin Hall angle
```

B.2.4 MOKE Response for the Calibration Field

Code used to generate the fitting curves in Fig. 5.9(a):

```
1 %% MOKE response under a calibration field as a fucntion of FM
      thickness
2 clear all
3
4 %Parameters for Calibration Fitting
5 a = 0.4e-10; %lattice constant (m)
6 lambda = 780e-9;  % wavelength (m)
7 refrac_layer = 2.38+1i*4.36; % refractive index of the FM layer
8 %refrac_Cu = 0.2+1i*4.9; % refractive index of the Cu layer
9 refrac_Si = 3.7+1i*0.008; %refractive index of the substrate (Si)
10 refrac_SiO2 = 1.43+1i*0.0; %refractive index of the oxidation (
      SiO2) %%%%%%%%%%%%%%%%%%%%%%%%%%%%%%%VERY SENSITIVE
```

```
    %%%%%%%%%%%%%%%
%refrac_Al2O3 = 1.6716+1i*0; %refractive index of the oxidation (
    Al2O3)
%refrac_Pt = 2.73+1i*6.04; %refractive index of the (Pt)
%refrac_Cu = 0.153 + 1i*4.84; %refractive index of copper
Q_FM = 0.0036-1i*0.011; % magneto-optic coefficient of Py
T_max = 80e-9; %The maximum thickness of the simulation (m)
m_z = 0.85e-3; %normalized magnetization tilt in z-direction, is
    actually m_z/M_s.(rad) (assume mu_0M_eff = 1T)

i = 1;
Reflectance = zeros(round(T_max/a),1);
Phi_S = zeros(round(T_max/a),1);
Phi_P = zeros(round(T_max/a),1);
for T = a: a: T_max %FM layer total thickness in (m)

% sample layer (first is air, last is substrate, thickness of both
    do not matter)
refrac = [1  refrac_layer  refrac_SiO2  refrac_Si]; % Construct
    the total refractive index vector
Q = [0  Q_FM  0  0]; % Construct the total magneto-optical
    constants vector (air/Sio2/Al2O3/Py/Al2O3/SiO2/Si)
h = [inf  T  1.0e-6  inf]; % Construct the overall thickness
    vector (air/Sio2/Al2O3/Py/Al2O3/SiO2/Si)
mz = [0  m_z  0  0]; % Construct the overall magnetization vector
    in z-direction (air/Sio2/Al2O3/Py/Al2O3/SiO2/Si)

```

```
30
31 [Reflectance(i), Phi_S(i), Phi_P(i)] = MOKE_MLmodel_SUB3(lambda, h
       , refrac, Q, mz); %Calculate the MOKE response for one
       thickness
32
33
34 i = i + 1;
35
36 end
37
38 %%
39 TT = a:a:T_max;
40 Thickness = 0.8*[5, 10, 15, 20, 30, 40, 60, 80]; %experiemental
       thickness points
41
42 Calib = [2.85*1.62, -28.72*1.24, -22.88*1.11, -18.70*1.05,
       -14.07*1.00, -10.88*0.99, -7.01*0.96, -6.11*0.94]/5; %
       calibration Kerr rotation (urad)
43 Calib2 = [-8.7*1.62, -5.72*1.24, -2.59*1.11, -1.77*1.05,
       -0.68*1.00, -0.24*0.99, 0.40*0.96, 1.09*0.94]; %calibration
       Kerr ellipticity (urad)
44
45 %data = [TT/1e-9; real(Phi_S')*1e6];
46 %fileID = fopen('thickness calibration rotation.txt','w');
47 %fprintf(fileID, '%f %e\n',data);
48 %fclose(fileID);
49
```

```
%data2 = [TT/1e-9; imag(Phi_S')*1e6];
%fileID2 = fopen('thickness calibration ellipticity.txt','w');
%fprintf(fileID2, '%f %e\n',data2);
%fclose(fileID2);

figure(3)
clf
plot(TT/1e-9,real(Phi_S)*1e9,'r','LineWidth', 4);
hold on
plot(TT/1e-9,imag(Phi_S)*1e9,'b','LineWidth', 4);
hold on
scatter(Thickness, Calib*1000, 'k', 'linewidth', 4);
hold on
scatter(Thickness, Calib2*1000, 'b', 'linewidth', 4);
%hold on
%errorbar(Thickness, Calib*1000, err*1000, 'LineStyle','none');
hold off
ylabel('Kerr rotation (nrad)')
xlabel('FM thickness (nm)')
title('Singal FM layer calibration MOKE signal at 780 nm
    wavelength (Ha = 10k)')
```